Vectorial beam coupling in fast photorefractive crystals with AC-enhanced response

Dissertation
zur Erlangung des Grades
eines Doktors der Naturwissenschaften

von

Oleg Filippov
Moskau / Russland

genehmigt vom Fachbereich Physik der

UNIVERSITÄT OSNABRÜCK

Osnabrück 2004

Contents

The work on this thesis was accompained by the following publications:

1. O. Filippov, K. H. Ringhofer, M. Shamonin, E. Shamonina, B. I. Sturman, A. A. Kamshilin, E. Nippolainen, *Polarization properties of light-induced scattering in $Bi_{12}TiO_{20}$ crystals: Theory and experiment for the diagonal geometry*, J. Opt. Soc. Am. **B 20**, 677-684, 2003.

2. O. Fillipov, K. H. Ringhofer, and B. I. Sturman, *Photorefractive ac-enhanced nonlinear response of sillenites: Low- and high-contrast effects*, *Eur. Phys. J.* **D**, 23, 285-290 (2003).

3. B. I. Sturman, O. Fillipov, *Exact solutions for vectorial beam coupling under AC-field in cubic photorefractive crystals*, *Phys. Rev.* **E 68**, 36613, (2003).

4. O. Fillipov, K. H. Ringhofer, B. I. Sturman, *Vectorial coupling in the sillenites under AC-enhancement: low- and high-contrast regimes*, *OSA TOPS* **87**, 345-350, (2003).

5. O. Fillipov, B. I. Sturman, *Linear signal detection with cubic photorefractive crystals under ac-field: influence of coupling effects.* (in preparation)

and presentations at:

- Ninth International Conference on Photorefractive Effects, Materials, and Devices. June 2003, Nice, France,

- Seminars of Graduate College 695.

Chapter 1

General introduction

Photorefractive (PR) beam coupling effects have been extensively studied during the last decades because of their strength and diversity and also because of a large application potential [1]. These effects are present in many materials, including ferroelectric/semiconductive crystals and polymers [2]. In crystals, the strongest coupling occurs in ferroelectrics whose nonlinear response is not sufficiently fast for many applications. Many efforts have been spent to find and optimize faster PR materials. Nowadays, cubic crystals of the sillenite family ($Bi_{12}SiO_{20}$, $Bi_{12}TiO_{20}$, $Bi_{12}GeO_{20}$) and also cubic semiconductors (CdTe, GaAs, and InP) meet the speed requirements most fully [3].

A common feature of the above fast materials is their relatively weak PR response. Two techniques, dc and ac, have been developed to enhance it [4, 5]. Both of them exploit applied electric fields. In the dc-case, the field is constant while the interacting waves are slightly detuned in frequency. In the ac-case, which is proven to be most useful for practical purposes, an applied electric field oscillates in time and no detuning is introduced between the light waves. The efficiency of the ac-technique depends on the temporal profile of the field [6]. The best enhancement occurs for a square-wave profile when the field changes periodically its sign.

The strong spatial amplification which can be achieved in sillenites, is accompanied by pronounced light-induced (nonlinear) scattering [7, 8]. The underlying mechanism of this phenomenon is not much different from that known for photorefractive ferroelectrics [3]. Weak seed waves arising because of the surface and bulk crystal imperfections, experience a strong spatial amplification at the expense of the pump.

Considerable progress in improving the photorefractive characteristics of sillen-

ites was made during the last decade [9, 10]. The fabrication of thin and long BSO and BTO crystals has allowed to increase the ac-field amplitude up to 50 kV/cm, to decrease the response time in cw-experiments to milliseconds, and to demonstrate a variety of strong nonlinear effects relevant to applications. Among them are fast phase conjugation [11], generation of surface light waves [12, 13], time separated recording and readout processes [14], and linear detection of weak signals [15].

A distinctive feature of the PR phenomena in fast cubic crystals is the vectorial character of wave coupling. The energy and polarization changes cannot generally be separated here from each other. Sensitivity of the nonlinear-optical effects to the polarization degrees of freedom (and also to the crystal cut) can be regarded as a property useful for applications.

An important step in describing the vectorial coupling was made recently in [16, 17]. The authors have summarized different aspects of vectorial beam coupling in cubic PR crystals and proposed a theoretical scheme capable of combining the general analytical methods with incorporation of the factual data on the PR response. This approach has allowed to describe in a uniform manner a number of important vectorial effects including the vectorial Bragg diffraction [18] and the angular distribution of the light-induced scattering in BTO and BSO crystals [16, 17].

The abovementioned theory describes well the vectorial coupling for a narrow region of the small light contrast m or under assumption of constant grating amplitude. It is known that the fundamental component of the space-charge wave E_K is linearly proportional to the light contrast only for small values of m. With increasing m, the function $E_K(m)$ becomes strongly nonlinear and the vectorial coupling theory needs to be corrected to work in the region of large contrast. The large-contrast effects in sillenites under ac-enhancement were investigated in [19, 20] by numerical methods, but the interpretation of the obtained results was insufficiently clear. The region of large contrast is especially important in connection with the soliton propagation problem [21] or for such application as the linear detection of weak signals [22, 23].

The linear detection technique was developed first in its scalar variant. However, as was recently shown, the vectorial beam coupling under ac-field can be effectively used for the linear detection too [24, 25]. The basic idea is not much different from that known for the scalar linear detection – to transform fast phase modulation of one of the input beams into output intensity modulation (so-called grating translation technique). The main obstacle on the way of implementation of this idea is that the index grating recorded in the ac-case is $\pi/2$ shifted with respect to the pump

light pattern. This feature would make the linear detection impossible in the scalar case [22]. In the vectorial case, this problem can be solved by using of polarization filtering of the output signals, as proposed in [15].

In this thesis we investigate such important aspects of the vectorial two-beam coupling in sillinites under ac-enhancement, as recording of the space-charge field grating in the large contrast regime, effect of the input beams polarizations on coupling characteristics and polarization properties of scattered light.

We begin, in Chapter 2, with the analysis of the space-charge field formation in the whole region of light contrast. We perform a theoretical description of this phenomena and consider the first three Fourier harmonics of the space-charge field. In Chapter 3 we incorporate the results from Chapter 2 to the vectorial two-beam coupling theory and extend it over the whole region of light contrast. Chapter 4 deals with the grating translation technique and related to it with the linear signal detection. We take into account the influence of the coupling effects on the output intensity modulation and optimize the linear detection parameters for different important experimental cases. Chapter 5 gives the information about the polarization properties of small-angle light-induced scattering in BTO crystals. To the best of our knowledge, polarization states of scattered waves in cubic crystals were never analyzed theoretically. A concluding Chapter 6 summarizes and accentuates the main aspects of the thesis and also discusses an outlook on open challenges and future tasks.

Chapter 2

Photorefractive ac-enhanced nonlinear response: low- and high-contrast effects

2.1 Introduction

The idea of ac-enhancement of the insufficiently high nonlinear response of fast photorefractive sillenites crystals goes back to the 80ies [1, 3]. It was found first in 1985 [5] that employment of a quickly oscillating electric ac-field increases the light-induced space-charge field within the low-contrast limit and makes the photorefractive response nonlocal, i.e., gradient-like. Such a nonlocal response is convenient for many practical purposes.

In the subsequent years the ac-enhancement technique had become the subject of numerous experimental and theoretical studies. It was found, in particular, that a square-wave shape of the ac-field provides the best enhancement [6], that the low-contrast range, where the fundamental component of the space-charge field grows linearly with m, is very narrow, and that the enhancement property is closely related to the presence of weakly damped, low-frequency eigenmodes – space-charge waves [26] – and to the generation of spatial subharmonics [3].

The large-contrast ac-effects in sillenites were partially investigated in [19, 20]. These works were restricted only to the fundamental component of the space-charge field and involve many phenomenological parameters, which have insufficiently clear significance [19, 20]. Recently, it was found under rather general conditions that the space-charge field induced in a fast ac-enhancemented crystal by a finite light beam

possesses a discontinuity [27, 28]. The width of this discontinuity lies in the sub-μm range, it is much smaller than the typical scale of light-intensity variations.

In this chapter we investigate the space-charge field grating formation in sillinites crystals under ac-enhancement. In particular, we account for the discontinuity of the field profile and analyze the dependences of the space-charge field harmonics amplitudes on the light contrast ranging from 0 to 1. We work in the terms providing generality of the obtained results and simplicity in using them for the vectorial beam coupling theory.

2.2 Basic relations

We assume that two light waves propagate symmetrically to the z-axis in a fast photorefractive crystal and a square-wave ac-field is applied parallel to the x-axis, see Fig.2.1. The vectorial complex amplitudes of the light waves we denote $\mathbf{a}_{1,2}$. They can change with z because of linear (field-induced birefringence and optical activity) and nonlinear (energy exchange) effects. The sum $|\mathbf{a}_1|^2 + |\mathbf{a}_1|^2$, which is proportional to the total intensity, does not depend on z. From now on we normalize the vectorial amplitudes in such a way that this sum equals to unity.

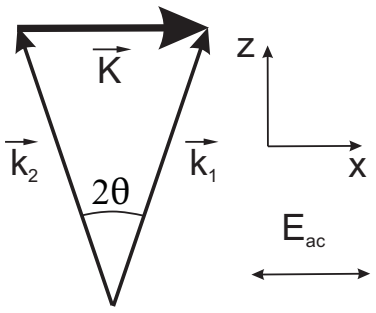

Fig.2.1. Geometrical diagram of an AC experiment.

The spatially modulated part of the intensity distribution, $\tilde{I}$, produced by these two waves and normalized to the sum of their intensities is

$$\tilde{I} = (\mathbf{a}_2^* \cdot \mathbf{a}_1) \exp(iKx) + \text{c.c.} \tag{2.1}$$

where $K = |\mathbf{k}_1 - \mathbf{k}_2|$ is the absolute value of the light wave vector difference (often called the grating vector), x is the fringe coordinate measured in the direction of the vector $\mathbf{k}_1 - \mathbf{k}_2$, and c.c. stands for complex conjugation. The contrast of the interference light pattern, m, is given by $m = 2|\mathbf{a}_2^* \cdot \mathbf{a}_1|$. The presence of the

scalar product in Eq. (2.1) and in the definition of m is important for optically isotropic cubic crystals. The polarization states of light waves change here because of nonlinear coupling and this change cannot be generally separated from the intensity changes [16, 29]. The contrast m reaches its maximum value (unity) only for equal intensities, $|\mathbf{a}_1|^2 = |\mathbf{a}_2|^2 = 1/2$, and identical polarization states, $\mathbf{a}_1 \parallel \mathbf{a}_2$. As clear from Eq. (2.1), the modulated part $\tilde{I}$ of the intensity distribution can be rewritten in the real form, $\tilde{I} = m\cos(Kx + \varphi)$ with $\varphi = \arg(\mathbf{a}_2^* \cdot \mathbf{a}_1)$. Generally, the phase φ depends on the propagation coordinate z because of coupling effects and this dependence is important for the description of the vectorial 2W-coupling.

The light-induced space-charge field E_{sc} is directed along the x-axis and can be presented in the form

$$E_{sc}(x) = E_K\, e^{i(Kx+\varphi)} + E_{2K}\, e^{2i(Kx+\varphi)} + \ldots + \text{c. c.} \tag{2.2}$$

The amplitudes E_K, E_{2K}, ... are complex functions of m; the form of these functions depends on the charge transport mechanism. The fundamental amplitude E_K is of prime importance for photorefractive effects because it characterizes the rate of mutual Bragg diffraction of the recording beams and, therefore, the coupling strength during 2W-coupling.

In the case under study the charge separation occurs under an alternating external field. This field is assumed to be parallel to the x-axis, to change periodically its sign, $E_{ex}(t) = \pm E_0$, and have an oscillation period much smaller than the photorefractive response time. These conditions provide an optimum ac-enhancement [6]. In the experiments, the amplitude E_0 is often larger than (or comparable with) 10 kV/cm. Diffusion charge separation is negligible in this case.

The high speed of the ac-oscillations allows to employ an averaging procedure to find the static profile $E_{sc}(x)$. This procedure was used first within the low contrast approximation (and within the conventional one-species model of charge transfer) to find the first spatial harmonic E_K [5]. The main result of this paper we present in a form which is convenient for what follows,

$$E_K/E_0 \simeq -i\, m\, Q/2 \tag{2.3}$$

where the real quantity $Q = Q(K, E_0)$ is the quality factor for the space-charge wave with wavevector K [26],

$$Q = \left(\frac{E_0}{E_q} + \frac{E_m}{E_0} + \frac{E_d}{E_0}\right)^{-1} \tag{2.4}$$

E_q, E_m, and E_d are the conventional characteristic fields [3, 1],

$$E_q = \frac{qN_t}{\epsilon\epsilon_0 K} \qquad E_m = \frac{1}{K\mu\tau} \qquad E_d = \frac{Kk_bT}{q} \tag{2.5}$$

q is the elementary charge, N_t the effective trap concentration, $\epsilon\epsilon_0$ the static dielectric constant, $\mu\tau$ the mobility-lifetime product for photo-excited electrons, k_b the Boltzman constant, and T the absolute temperature.

The maximum value of the function $Q(K, E_0)$ is $(qN_t\mu\tau/4\epsilon\epsilon_0)^{1/2}$ [26]. The fast photorefractive crystals are distinguished by large values of the $\mu\tau$-product , here $Q_{max} \gg 1$. With the values $N_t = 2 \cdot 10^{16}$ cm^{-3}, $\mu\tau = 3 \cdot 10^{-7}$ cm^2/V, and $\epsilon\epsilon_0 = 50$, representative for the sillenites, we have $Q_{max} \simeq 8$.

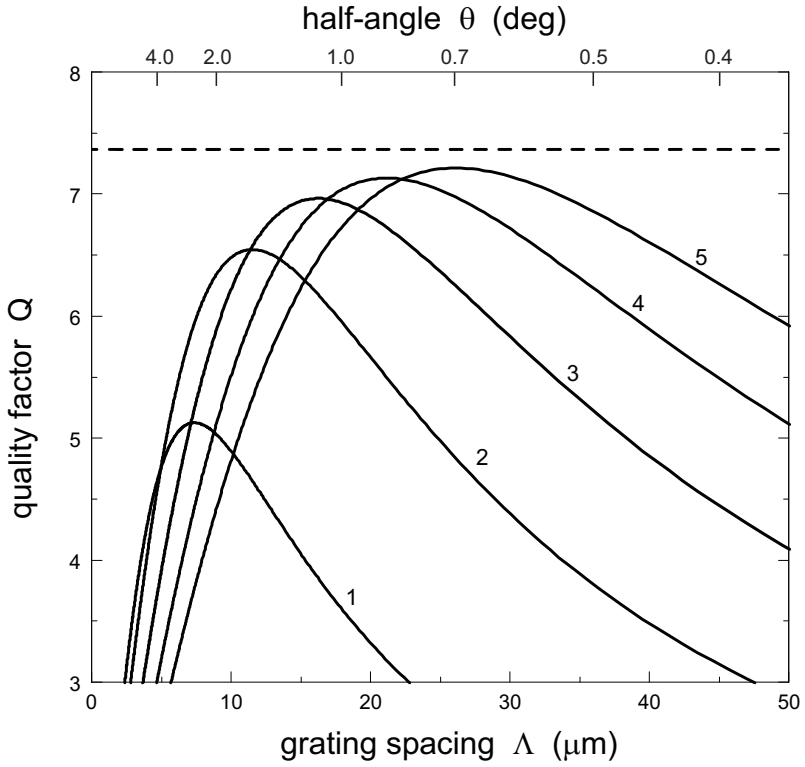

Fig.2.2. Dependence $Q(\Lambda)$ for $\epsilon\epsilon_0 = 50$, $N_t = 2 \cdot 10^{16}$ cm^{-3}, $\mu\tau = 3 \cdot 10^{-7}$ cm^2/V, and several values of E_0. The curves 1, 2, 3, 4, and 5 correspond to $E_0 = 4$, 8, 12, 16 and 20 kV/cm, respectively. The dashed line shows the value of Q_{max} for the accepted material parameters.

The most important features of the dependence $Q(K, E_0)$ can be described as follows. For E_0 considerably larger than $(N_tk_bT/\epsilon\epsilon_0)^{1/2}$ (which is typically of the order of a few kV/cm) the diffusion contribution to Q [the last term in Eq. (2.4)] can be neglected. In this case, the optimum value of the grating vector, $K_{opt} \simeq$

$E_0^{-1}\,(qN_t/\epsilon\epsilon_0\mu\tau)^{1/2}$ and the corresponding peak value of $Q(K)$ is not far from Q_{max}. This is illustrated by Fig.2.2 for the above presented material parameters. Note that for $E_0 \sim 10$ kV/cm the optimum value of K corresponds to the half-angle θ between the incident light beams (see Fig.2.1) of the order of a few degrees. The larger E_0, the wider (in Λ) is the region of large Q. The presence of the ac-enhancement manifests itself clearly in experiments on light-induced scattering in the sillenites [16, 30, 31]: The strongest scattering angles correspond to K_{opt}.

The introduced quality factor has also an apparently different implication. It defines the threshold of the so-called subharmonic generation in the sillenites, which corresponds to the parametric instability against excitation of weakly damped space-charge waves [26, 32]. Lastly we mention that the quality factor can be directly measured experimentally [33].

Let us return to Eq. (2.3) valid in the low contrast approximation. The presence of the imaginary unit i means that the photorefractive response is nonlocal, i.e., the light and field fringes are shifted to each other by a quarter of a period.

Since the amplitude of the space-charge field related to the first Fourier harmonic is $2|E_K|$, we have $E_{sc}^{(1)}/E_0 \simeq mQ$. Hence already at $m \approx Q^{-1} \ll 1$, the space-charge field becomes comparable with the applied field. The linear approximation (ignoring the material nonlinearity) is clearly broken here. This situation differs strongly from that typical for slow ferroelectrics, which is caused by the difference in values of the lifetime-mobility product for photo-excited charge carriers [26].

Recently, the procedure of averaging over the fast ac-oscillations was applied to the nonlinear case (an arbitrary light contrast) to obtain a simple differential equation for the normalized space-charge field $e = E_{sc}(x)/E_0$ in the diffusion-free limit $E_0 \gg (N_t k_b T/\epsilon\epsilon_0)^{1/2}$. This ordinary second-order equation reads [27],

$$\left[\frac{(e^2-1)\,(1+\tilde{I})}{1+l_s\,e_x}\right]_x = \frac{e\,(1+\tilde{I})}{l_0} \tag{2.6}$$

where the subscript x denotes the x-differentiation, $l_0 = \mu\tau E_0$ is the characteristic drift length, and $l_s = \epsilon\epsilon_0 E_0/qN_t$ the characteristic saturation length. For representative parameters of the sillenites and $E_0 = 20$ kV/cm we have the estimates, $l_0 \approx 50$ μm, $l_s \approx 0.4$ μm. Correspondingly, the grating vector K has to range between l_0^{-1} and l_s^{-1} to meet the requirement $Q \gg 1$.

Within the linear approximation in $\tilde{I}$ we have from here $l_0 l_s e_{xx} - e = l_0 \tilde{I}_x$ and for the first harmonic E_K we return immediately to Eq. (2.3). In the general case, an even intensity distribution $\tilde{I}(x)$ produces an odd distribution $e(x)$.

The distinctive feature of Eq. (2.6) is the presence of the smallest characteristic length l_s before the derivative e_x in the denominator. As soon as the nonlinear terms (in m) become important, this feature causes a highly peculiar behavior of the field profile $e(x)$. Namely, this profile cannot be smooth on the scale of the grating period $\Lambda = 2\pi/K$, it has to include a discontinuity of $e(x)$. If we assume the opposite, the term $l_s e_x$ can be neglected; then Eq. (2.6) becomes a first-order differential equation which cannot possess any periodic solution for e. Therefore the solution of Eq. (2.6) must possess discontinuities. Their width can be estimated as $\approx l_s$.

2.3 Space-charge fields harmonics

Recently, equation (2.6) was applied to the beam propagation problem [28]. Below we use it to describe the characteristics of light-induced gratings arising during 2W-mixing. Correspondingly, the modulated part $\tilde{I}$ of the intensity distribution was chosen in the form $\tilde{I} = m\cos(Kx)$. Apart from the low-contrast limit, Eq. (2.6) can be solved only numerically.

Figure 2.3 shows the main tendencies in the change of the space-charge field profile with increasing contrast for $Q \approx 6$. One sees that a sine-like profile occurs only for $m \lesssim 0.05$. With increasing m, the discontinuity (situated at the intensity maximum) quickly progresses; far from the discontinuity the function $e(x)$ experiences a strong saturation and approaches the square-wave form $e = \pm 1$. The light-induced field never exceeds the applied field, $|E_{sc}| < E_0$. It is curious that a strong steepening of the field profile at the intensity minima ($x/\Lambda \simeq \pm 0.5$) occurs only when m is approaching unity.

Since the function $e(x)$ is odd, all its Fourier harmonics are imaginary,

$$e_n(m) \equiv \frac{E_n(m)}{E_0} = -2i \int_0^{1/2} e(\xi, m)\sin(2\pi n\xi)\, d\xi \tag{2.7}$$

with $\xi = x/\Lambda$. This means, in particular, that the fundamental component of $E_{sc}(x)$ is $\pi/2$-shifted with respect to the intensity distribution for any value of the contrast, i.e., the photorefractive ac-enhancement response is always nonlocal. Using the approximation of a square-wave profile of $e(x)$ for $m = 1$, we obtain the following estimate of the limit values of the spatial harmonics: $e_n(1) \simeq -2i/n\pi$ for odd numbers ($n = 1, 3, \ldots$) and $e_n(1) = 0$ for even numbers, ($n = 2, 4, \ldots$). For the fundamental component we expect, therefore, the limit value $|e_1(m = 1)| \simeq 2/\pi \simeq 0.64$.

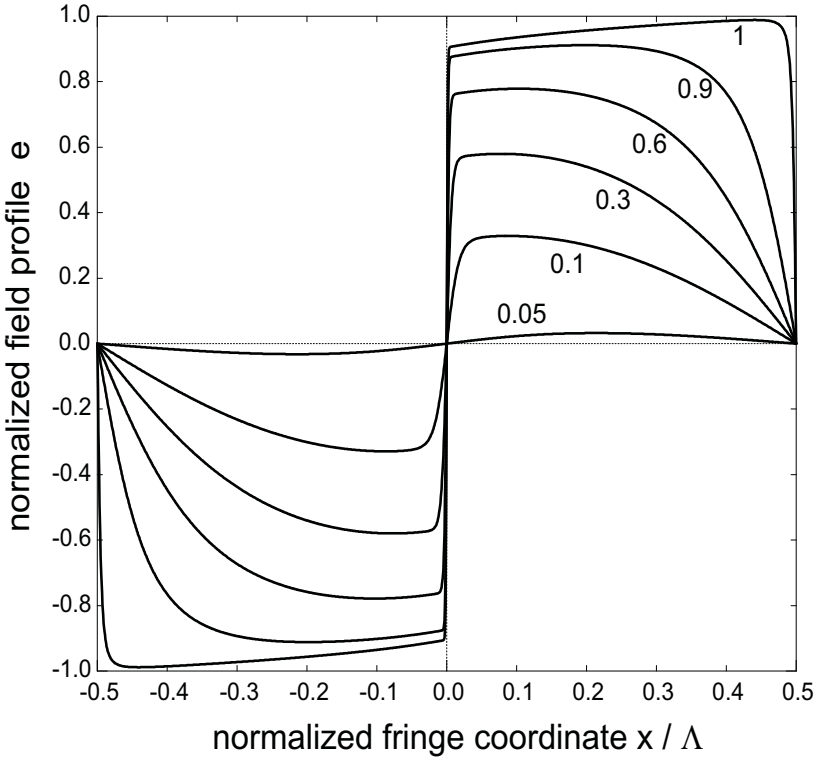

Fig.2.3. The profile $e(x)$ for the accepted material parameters, $E_0 = 13$ kV/cm, $\Lambda = 30$ μm, ($Q \simeq 6.2$), and several values of the contrast. The curves 1, 2, 3, 4, 5, and 6 correspond to $m = 0.05$, 0.1, 0.3, 0.6, 0.9, and 1.0, respectively.

For what follows it is useful to represent the dependence $e_1(m) \equiv E_K(m)/E_0$ in the form

$$e_1 = -(imQ/2)\, f(Q, m) \tag{2.8}$$

where $f(Q, m)$ is a dimensionless function with a unit initial value, $f(Q, 0) = 1$. While using Eq. (2.8) for the description of the vectorial coupling [16, 31], it is important to keep the phase factor $\exp(i\varphi) = 2(\mathbf{a}_2^* \cdot \mathbf{a}_1)/m$ in Eq. (2.2).

The solid curve in Fig.2.4 shows the result of our numerical calculation of the function $|e_1| = Qmf(m)/2$ on the basis of Eq. (2.6); it corresponds to $Q \simeq 6.2$. This curve, which is remarkable, can be considered as a characteristic one. Fairly wide changes of the parameters N_t, $\mu\tau$, E_0, and Λ do not affect it seriously, provided the corresponding values of the quality factor Q lie within the range $(5 - 7)$ which is most interesting for experiment. The vertical bars in Fig.2.4 show the spread of the results obtained for $N_t = (1 - 6) \cdot 10^{16}$ cm^{-3}, $\mu\tau = (0.7 - 4.2) \cdot 10^{-7}$ cm^2/V, $E_0 = (12 - 30)$ kV/cm, and $\Lambda = (10 - 50)$ μm. With increasing contrast this spread is decreasing. At $m = 1$ we have $|e_1| \simeq 0.62$, which agrees well with the above made

analytic estimate. The close proximity of different curves means (i) that the quality factor Q determines the photorefractive nonlinear response in the whole range of the light contrast m and (ii) that the dependence of this response on Q is saturated for $Q \gg 1$.

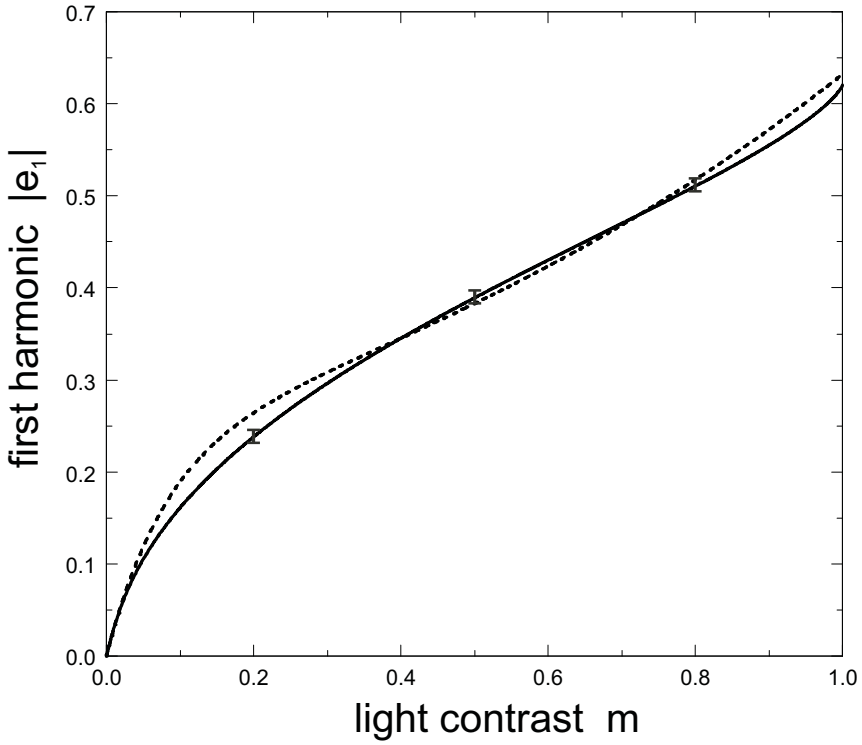

Fig.2.4. The solid lien is the calculated dependence of $|e_1|$ on the light contrast for $Q = 6.2$. The dotted curve corresponds to the phenomenological Eq. (2.9) with $Q = 6.2$ and $a = 2.15$.

It is of interest to compare the results of our numerical calculations with the expression used in [19, 20] for fitting the numerical results and experimental data. In our terms, this fit is equivalent to the representation of the function $e_K(m)$ in the form

$$e_K = (-iQ/2a)[1 - \exp(-am)]\,\exp(m) \tag{2.9}$$

where a is a fitting parameter. The dotted curve in Fig.2.4 shows the best fit of our numerical results, it corresponds to $a = 2.15\,Q$. One sees that the fitting function given by Eq. (2.9) reproduces fairly well the main features of the photorefractive ac-response. At the same time, the difference between the solid and dotted lines is noticeable for $m \approx 0.15$.

Instead of the contrast m, it is often useful to employ the pump intensity ratio β. These quantities are coupled by the relation $m = 2\sqrt{\beta}/(1+\beta)$ with β ranging from 1 to ∞. Figure 2.5 shows the dependence $|e_1(\beta)|/m(\beta) = Q\, f(\beta)$ in a logarithmic scale for 8 different combinations $\mu\tau$, N_t, E_0, and Λ. For the curves 2 – 7 the quality factor ranges from 6 to 7, whereas the curves 1 and 6 are plotted for considerably smaller and bigger values of Q, respectively. For very large intensity ratios, $\log_{10}(\beta) > (4-5)$ (the low-contrast limit), each curve is characterized by a plateau on the level of $Q/2$; all the curves are clearly separated here. In the opposite case, $\log_{10}(\beta) \lesssim 2$ ($m \gtrsim 0.2$), the curves with $Q \geq 6$ practically coincide.

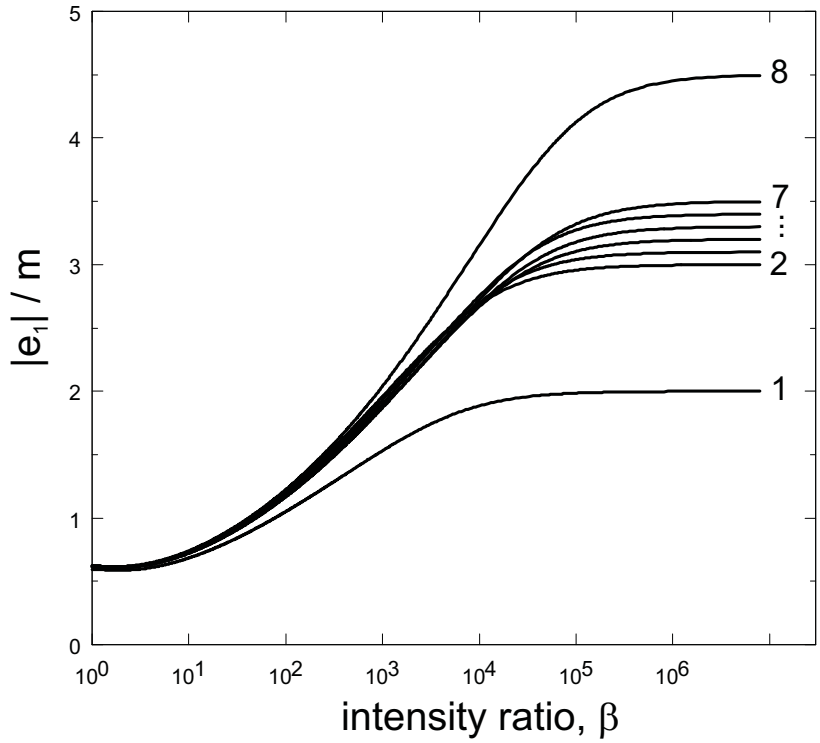

Fig.2.5. Dependence of $|e_K|/m$ on β. The values of Q, $\mu\tau$ (in 10^{-7} cm^2/V), N_t (in 10^{16} cm^{-3}), Λ (in μm), and E_0 (in kV/cm) for the curves 1 – 8 are the following: 1 – (4.0, 1.63, 2.37, 40, 18); 2 – (6.0, 2.51, 2.38, 10, 18); 3 – (6.2, 4.23, 1.06, 20, 12); 4 – (6.4, 7.68, 6.6, 15, 30); 5 – (6.6, 1.48, 4.23, 25, 24); 6 – (6.8, 4.03, 1.44, 35, 14); 7 – (7.0, 3.34, 2,94, 50, 20); 8 – (9.0, 3.12, 2.94, 25, 20).

As seen from Figs. 2.4, 2.5, the whole contrast range can roughly be separated into two regions. The region $0 < m \lesssim 0.05$ ($\beta \gtrsim 10^4$) corresponds to the linear theory [5]. Here the fundamental amplitude E_K grows rapidly with the contrast and the rate of spatial amplification of weak signals is extremely high, up to 10^2 cm^{-1}. In

the second region, $0.05 \lesssim m \leqslant 1$, the growth of $E_K(m)$ is strongly saturated. This region is more appropriate for grating recording than for the spatial amplification purposes.

It should be underlined that the results exhibited are related to the case $Q \gtrsim (3-5)$ which is our prime interest. While the quality factor approaches unity, the effects of ac-enhancement fade quickly.

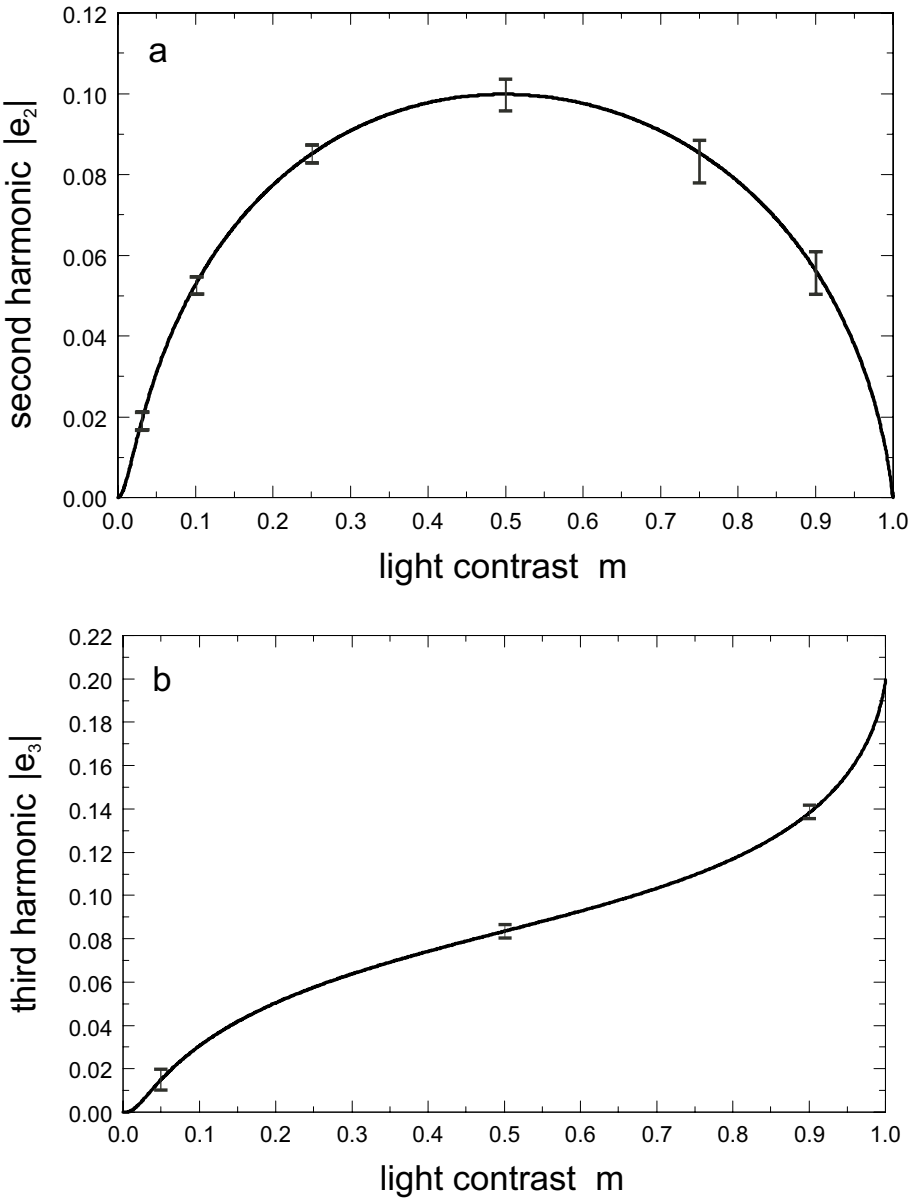

Fig.2.6. Dependence of the second (a) and third (b) spatial harmonics on the contrast m. The assumptions made are the same as for Fig.2.4.

Apart from the fundamental harmonic e_K, responsible for beam-coupling effects, the first higher harmonics $e_2 = E_{2K}/E_0$ and $e_3 = E_{3K}/E_0$ are of practical interest. These harmonics can be measured with the help of auxiliary Bragg-matched light beams, they are important for characterization purposes. Since the function $e(x)$ is odd, all the higher Fourier harmonics are imaginary. Figures 6a and 6b show the dependences $|e_2(m)|$ and $|e_3(m)|$, respectively calculated for the same parameters as the solid curve of Fig.2.4. The function $|e_2(m)|$ peaks at $m \simeq 0.5$ and turns (as expected) to zero at $m = 1$. This dependence corresponds to the formation of the step-like field profile with increasing m, see Fig.2.3. Note that the initial (quadratic) interval of $|e_2(m)|$ is extremely narrow, $m \lesssim 0.02$, and the maximum expected value of $|E_{sc}^{(2)}|$ is about $0.2E_0$. The spread of the curve in Fig.2.6(a) (shown by the vertical bars) is noticeably larger than that in Fig.2.4, especially in the region of relatively large m. The dependence $e_3(m)$ shown in Fig.2.6(b) looks quite different. It tends first to saturate at $m \simeq 0.2$ but experiences then a remarkable growth with m approaching unity. The maximum value of $E_{sc}^{(3)}$ is about $0.4E_0$. Both dependences of Fig.2.6 can be considered as the fingerprints of the ac-response in the sillenites.

Let us comment first on the relationship between our results and the numerical results presented in [19, 20]. First of all, we note that there is no serious contradiction between them. But there are, nevertheless, some differences. Partially, the parameters used in these papers correspond to the case $E_0 \lesssim (N_t k_b T/\epsilon\epsilon_0)^{1/2}$, which is of minor interest and lies outside the field of applicability of Eq. (2.6). Simulation of the time development of the charge density on the basis of the conventional one-species model restricted the possibilities of numerical experiments. In particular, the states attained were not fully stationary yet. It is not quite clear also whether the coordinate step used was always considerably smaller than the saturation length l_s. The mentioned circumstances can be the reason for minor quantitative distinctions in the cases where the approaches used can be compared.

Introduction of the quality factor Q has allowed us to represent the data on the fundamental harmonic in a fairly simple manner. This is especially true for the case $Q \gg 1$ which has become topical during the last years. The form of our results allows their incorporation into the theory of vectorial beam coupling (see Chapter 3). Also we get the new data on the higher spatial harmonics $E_{2K,3K}$.

Several implications of the ac-response considered are also worth of discussion. The first one is how to measure the dependences $E_{nK}(m)$ experimentally. In our opinion, the standard coupling geometries (the longitudinal, transverse, and diagonal), where the recording light beams propagate near the [110] (or [$\bar{1}$10]) axis, are

not very useful for this purpose. The point is the coupling effects (involving also the polarization changes) can hardly be excluded even for relatively thin ($\sim$ 1 mm) samples. The most useful one seems to be the geometry used in [32, 33] where the recording beams propagate nearby the [001] axis and the testing Bragg-matched beams propagate nearby [110]. In this case, the recorded space-charge field is not distorted by coupling effects and the minor remaining theoretical problem is to take into account the influence of optical activity and the ac-induced birefringence on the measured diffraction efficiency [18]. A similar technique was used to measure the higher harmonics of E_{sc} induced in the case of the co-called resonant dc-enhancement of the photorefractive response [34, 35].

The next aspect is the influence of the m-dependence of the fundamental harmonic on the characteristics of two-beam coupling in the sillenites. It is important to realize that this coupling is essentially vectorial, i.e., it cannot be reduced to the scalar one in the general case. The aforesaid is especially true with respect to the cases where the optical activity is essentially involved (which is, e.g., always the case for BSO crystals). The use of the formulae of the scalar theory for fitting of the experimental dependences can result here in misleading conclusions. In the next Chapter, we apply the information obtained here to expand the vectorial beam coupling theory on the whole range of light contrast.

2.4 Resume

Using the governing equation for the space-charge field induced during 2W-coupling under an ac-field in the sillenites, we have analyzed numerically the dependences of the first Fourier harmonics, $E_{1,2,3}$ on the light contrast ranging from 0 to 1. We found out that these rather peculiar dependences are strongly controlled by the only scalar parameter - the quality (enhancement) factor Q. Comparison with the results of the previous studies is performed and the possibility for experimental detection of the theoretical predictions are discussed.

Chapter 3

Exact solution for vectorial beam coupling

3.1 Introduction

The vectorial character of beam coupling in sillinite crystals arises due to their cubic symmetry. As known, for this kind of symmetry the wave vectors of two orthogonal eigenmodes are equal. Even for sufficiently large applied electric field, the induced birefringence cannot exclude the coupling of waves with different polarizations. Therefore, the energy exchange between light waves is accompanied by polarization changes. Furthermore, specific features of the electro-optic effect and the presence of optical activity in cubic crystals lead to a high sensitivity of beam coupling to the input beam polarizations, crystal cut, orientation of the applied field, etc.

The theoretical description of the photorefractive nonlinear phenomena in cubic crystals was for a long time very fragmental. First studies were devoted to the analysis of vectorial beam coupling via a spatially uniform index grating [18, 29, 36, 37, 38]. The results show the importance of the polarization degree of freedom and of the orientation of the grating fringes for the optimization of the readout process. Most of these papers use various approximations or numerical methods to solve the vectorial Bragg-diffraction problem. In [18, 36] this problem was exactly solved in the paraxial limit. In any case, the assumption of a uniform grating cannot be applied to the cases of strong energy and polarization exchange between the interacting light waves.

A number of publications deal with the analysis of strong nonlinear effects caused

by the enhanced PR response [12, 39, 40]. Unfortunately, the authors restrict themselves usually to the formulation of the governing equations for the wave amplitudes and to particular numerical solutions of these equations. The corresponding numerical results give no general insight into the nonlinear phenomena under study. Moreover, the initial equations often do not include details essential for the wave coupling such as, for instance, secondary electro-optic effect and the effect of the external electric field on the linear properties of the crystal.

The theory of the vectorial beam coupling, which summarized most features of the beam coupling in cubic crystals, was developed in [16]. The simplicity and efficiency of this theoretical description allowed to explain well many observable phenomena. Unfortunately, this approach was also restricted by the region of small light contrast.

The purpose of this Chapter is to investigate (analytically and numerically) the vectorial two-beam coupling process in the case of ac-enhancement. Our findings can be considered as an extension of the classical results obtained for the case of scalar beam coupling [1, 3] to the vectorial case.

3.2 Vectorial diffraction equation

Let two light waves, 1 and 2, be coupled in a cubic PR crystal via diffraction from a light-induced grating of the space-charge field whose grating vector $\vec{K}$ is the difference of the light wave vectors, see Fig. 3.1(a).

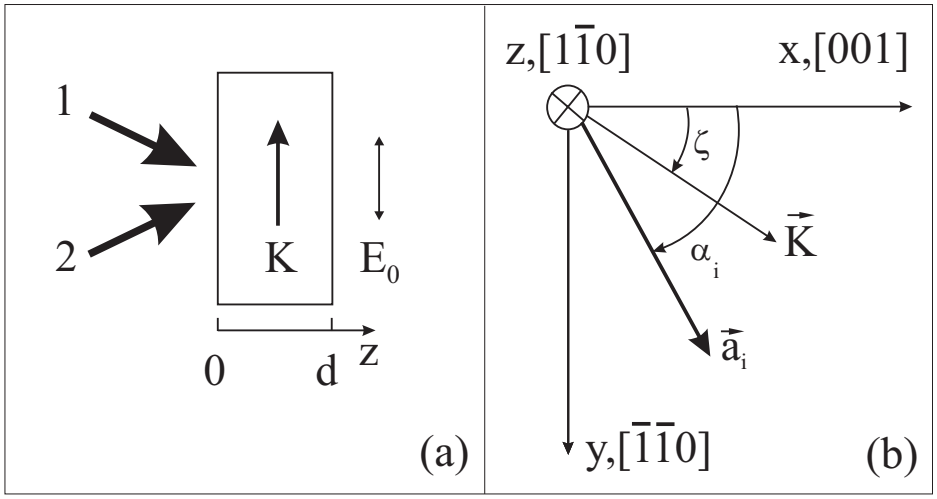

Fig. 3.1. (a) Schematic of a two-wave coupling experiment. (b) Orientation of the main 2D vectors about the crystal axes, $\vec{a}_i$ is the amplitude of the i^{th} wave ($i = 1, 2$).

As soon as light absorption is neglected, the total intensity of the waves does not depend on the propagation coordinate, z, and we can normalize the vectorial complex wave amplitudes $\vec{a}_1, \vec{a}_2$ in such a way that $|\vec{a}_1|^2 + |\vec{a}_2|^2 = 1$. The amplitude of the light-induced space-charge field we denote E_K; it is generally a function of z. With this notation and within the conventional paraxial approximation, the set of equations describing vectorial Bragg diffraction from the grating can be presented in the following general and compact form [16]:

$$(\frac{d}{dz} - i\boldsymbol{\kappa} \cdot \hat{\boldsymbol{\sigma}})\, \vec{a}_1 = iE_K\, (\nu_0 + \boldsymbol{\nu} \cdot \hat{\boldsymbol{\sigma}})\, \vec{a}_2 \tag{3.1}$$

$$(\frac{d}{dz} - i\boldsymbol{\kappa} \cdot \hat{\boldsymbol{\sigma}})\, \vec{a}_2 = iE_K^*\, (\nu_0 + \boldsymbol{\nu} \cdot \hat{\boldsymbol{\sigma}})\, \vec{a}_1 \tag{3.2}$$

Here $\boldsymbol{\kappa} = (\kappa_1, -\rho, \kappa_3)$ (ρ is the rotatory power) and $\boldsymbol{\nu} = (\nu_1, 0, \nu_3)$ are known real 3D vectors, ν_0 is a known real scalar, $\hat{\boldsymbol{\sigma}} = (\sigma_1, \sigma_2, \sigma_2)$ the standard set of 2×2 Pauli matrices, see [64], and $\vec{a}_{1,2}$ are 2D vectors with x and y components (**NB:** the 3D quantities with $1, 2, 3$-components are denoted by bold letters). The vector $\boldsymbol{\kappa}$ characterizes the linear optical properties; its components $\kappa_{1,3}$ account for the changes of the optical permittivity induced by a uniform applied electric field via the linear electro-optic effect and the component $\kappa_2 = -\rho$ accounts for the effect of optical activity (if it is present in the crystal). The vector $\boldsymbol{\nu}$ and the scalar ν_0 are responsible for the anisotropic and isotropic parts of diffraction, respectively. The fact that the component $\nu_2 = 0$ means that the light-induced space-charge field does not produce any changes of the rotatory power ρ. The set (3.1), (3.2) can be considered as an extension of the known scalar Kogelnik theory to the vectorial case. One can check that the hermitian property of the σ-matrices ensures the conservation of the total wave intensity, i.e.,

$$I_0 = |\vec{a}_1|^2 + |\vec{a}_2|^2 = 1 \tag{3.3}$$

is the integral of Eqs. (3.1), (3.2). In the case of a uniform grating, $E_K(z) = const$, the set (3.1), (3.2) admits nontrivial exact general solutions for the vectorial diffraction [18, 16].

In the case of nonuniform index grating $E_K(z)$ the expression for the grating amplitude E_K was obtained in the Chapter 2 (see Eq.(2.8)).

The coefficients $\kappa_{1,3}$ and $\nu_{0,1,3}$ entering Eqs. (3.1), (3.2) can be calculated for any orientation of the applied field $\vec{E}_0$ and the grating vector $\vec{K}$ about the crystal axes.

Below we restrict ourselves to the case where the propagation axis z is directed along $[1\bar{1}0]$, see Fig. 3.1(b), and the applied field $\vec{E}_0$ is parallel to the grating vector $\vec{K}$; this covers most of the topical situations. Then the components $\kappa_{1,3}$ can be presented in the form

$$\kappa_1 = sE_0 \sin\zeta \qquad \kappa_3 = -\frac{sE_0}{2} \cos\zeta \tag{3.4}$$

where ζ is the angle between $\vec{K}$ and the [001] crystal axis, $s = -\pi n_0^3 r_{41}/\lambda$, n_0 the non-perturbed refractive index, r_{41} the only non-zero electro-optic constant, and λ the wavelength. The sign of E_0 can be positive and negative in Eqs. (3.4). The coefficients $\nu_{0,1,3}$ include generally not only electro-optic but also elasto-optic contributions, the latter can sometimes be of importance. If we neglect the elasto-optic contributions, then

$$\nu_0 = \frac{s}{2} \cos\zeta \qquad \nu_1 = s \sin\zeta \qquad \nu_3 = -\frac{s}{2} \cos\zeta \tag{3.5}$$

The data on $\nu_{0,1,3}(\zeta)$ with the elasto-optic contributions taken into account can be found in [16].

Three particular cases are especially important for the experiments:

• The transverse (T) geometry, $\vec{K}, \vec{E}_0 \perp [001]$, i.e., $\zeta = 90°$. Here $\kappa_1 = sE_0, \kappa_3 = 0$. The elasto-optic contributions renormalize here slightly the electro-optic constant r_{41}, therefore $\nu_0 = 0, \nu_1 \simeq s$, and $\nu_3 = 0$.

• The longitudinal (L) optical configuration, $\vec{K}, \vec{E}_0 \parallel [001]$, i.e., $\zeta = 0$. Here $\kappa_1 = 0, \kappa_3 = sE_0/2$. The elasto-optic contributions are absent here, hence $\nu_0 = s/2, \nu_1 = 0$, and $\nu_3 = -s/2$.

• The diagonal (D) geometry, $\vec{K}, \vec{E}_0 \parallel [111]$, $\zeta = \arctan(\sqrt{2}) \simeq 54.7°$. Here $\kappa_1 = \sqrt{2}\, sE_0, \kappa_3 = -sE_0/2\sqrt{3}$. The elasto-optic contributions to $\nu_{0,1,3}$ are clearly pronounced here, they can give up to 40% corrections to the values given by Eqs. (3.5), see Chapter 5.

There is a big number of optical configurations that are equivalent (for symmetry reasons) to the above considered, these configurations are listed in [16].

Commenting the above relations for the optical configurations, we mention first that the isotropic part of diffraction is absent in the T-geometry. This case is maximally different from the familiar scalar diffraction. Furthermore, there is no case where the anisotropic part of diffraction is absent or small as compared to the isotropic part. Hence strong polarization effects are expected in cubic PR crystals.

It is important for what follows that the vectors $\boldsymbol{\kappa}$ and $\boldsymbol{\nu}$ are parallel to each other in the L- and T-geometries if the optical activity is absent (crystals of the $\bar{4}3m$ point

group). In the sillenites (where $\rho \neq 0$) $\boldsymbol{\kappa}$ is approximately parallel to $\boldsymbol{\nu}$ for $s|E_0| \gg \rho$, which means suppression of optical activity by the applied field. This situation is typical for ac-experiments with BTO crystals, where $\rho \simeq 6.5\,\mathrm{deg/mm} \simeq 1.1\ \mathrm{cm}^{-1}$, $|s| \simeq 4 \cdot 10^{-4}\ \mathrm{V}^{-1}$, and the amplitude $|E_0|$ ranges from 10 to 50 kV/cm. In the D-geometry, it is necessary to be careful when using the approximation $\boldsymbol{\kappa} \parallel \boldsymbol{\nu}$ because of noticeable elasto-optic contributions to $\boldsymbol{\nu}_{1,3}$.

3.3 Analysis and simplification of vectorial equations

First, using Eq. (2.8), we exclude E_K from Eqs. (3.1)-(3.2) and obtain the closed set of equations for $\vec{a}_{1,2}$,

$$(\frac{d}{dz} - i\boldsymbol{\kappa}\cdot\hat{\boldsymbol{\sigma}})\,\vec{a}_1 = Q|E_0|\,f(m)\,(\vec{a}_1\cdot\vec{a}_2^*)\,(\nu_0 + \boldsymbol{\nu}\cdot\hat{\boldsymbol{\sigma}})\,\vec{a}_2 \tag{3.6}$$

$$(\frac{d}{dz} - i\boldsymbol{\kappa}\cdot\hat{\boldsymbol{\sigma}})\,\vec{a}_2 = -Q|E_0|\,f(m)\,(\vec{a}_1^*\cdot\vec{a}_2)\,(\nu_0 + \boldsymbol{\nu}\cdot\hat{\boldsymbol{\sigma}})\,\vec{a}_1 \tag{3.7}$$

where, as earlier, $m = 2|\vec{a}_1\cdot\vec{a}_2^*|$.

In the next step we prove that the light interference fringes experience neither bending nor tilting inside the crystal despite of the coupling effects. This is an important generalization of the property of beam coupling known for the nonlocal response in the scalar case on the vectorial case. We note first that the light intensity pattern inside the crystal is proportional to $[1 + m\cos(\vec{K}\cdot\vec{r} + \Phi)]$, where $\Phi = \arg(\vec{a}_1\cdot\vec{a}_2^*)$ and $\vec{K} \perp \mathbf{z}$. If $\Phi(z) = const$, the light fringes remain perpendicular to the input face. Multiplying the vectorial equations (3.6) and (3.7) scalarly by $\vec{a}_2^*$ and $\vec{a}_1^*$, respectively, combining the obtained scalar relations, and using the hermitian property of the σ-matrices, we obtain the necessary equality $\partial_z\Phi_z = 0$. This general property of the light fringes was missed in [16]. Being very simple, it simplifies greatly the following considerations.

Since the phase $\Phi(z) = const$, we can put it equal zero without any loss of generality. In other words, one can make the replacement $\vec{a}_{1,2} \to \vec{a}_{1,2}\,\exp(\pm i\Phi/2)$ to work then with new fully equivalent vectorial light amplitudes. Therefore, from now on we set $\vec{a}_1\cdot\vec{a}_2^* = m/2$.

At this point, we need to make the main approximation of this paper, namely $\boldsymbol{\kappa} \parallel \boldsymbol{\nu}$. The situations where it is justified have been considered in the previous section. Within this approximation, the set of nonlinear equations (3.6), (3.7) admits

exact solutions while the polarization properties of beam coupling remain far from trivial.

To get rid of the linear terms in Eqs. (3.6), (3.7), we perform a unitary transformation from $\vec{a}_{1,2}$ to the amplitudes $\vec{b}_{1,2}$,

$$\vec{a}_{1,2} = \exp[i(\boldsymbol{\kappa} \cdot \hat{\boldsymbol{\sigma}})\, z]\, \vec{b}_{1,2} \tag{3.8}$$

This transformation does not change the scalar products; in particular, $|\vec{a}_{1,2}(z)|^2 = |\vec{b}_{1,2}(z)|^2$ and $\vec{a}_1(z) \cdot \vec{a}_2^*(z) = \vec{b}_1(z) \cdot \vec{b}_2^*(z) \equiv m(z)/2$. It does not change also the input values of the amplitudes, $\vec{b}_{1,2}(0) = \vec{a}_{1,2}(0)$. After the unitary transformation we have (using the property $\boldsymbol{\kappa} \parallel \boldsymbol{\nu}$):

$$\frac{d}{dz}\, \vec{b}_1 = +\, (Q|E_0|/2)\, m f(m)\, (\nu_0 + \boldsymbol{\nu} \cdot \hat{\boldsymbol{\sigma}})\, \vec{b}_2 \tag{3.9}$$

$$\frac{d}{dz}, \vec{b}_2 = -\, (Q|E_0|/2)\, m f(m)\, (\nu_0 + \boldsymbol{\nu} \cdot \hat{\boldsymbol{\sigma}})\, \vec{b}_1 \tag{3.10}$$

Lastly, we transfer from the propagation coordinate z to the variable ξ (an effective coordinate),

$$\xi = (Q|E_0|/2) \int_0^z m(z')\, f[m(z')]\, dz' \tag{3.11}$$

to obtain instead of Eqs. (3.9), (3.10):

$$\frac{d}{d\xi}\, \vec{b}_1 = +\, (\nu_0 + \boldsymbol{\nu} \cdot \hat{\boldsymbol{\sigma}})\, \vec{b}_2 \tag{3.12}$$

$$\frac{d}{d\xi}\, \vec{b}_2 = -\, (\nu_0 + \boldsymbol{\nu} \cdot \hat{\boldsymbol{\sigma}})\, \vec{b}_1 \tag{3.13}$$

This set of differential equations is already *linear*, it describes vectorial diffraction from a uniform grating and admits an exact general solution in the terms of the effective coordinate ξ. The nonlinear part of the problem is therefore reduced to determination of the function $\xi(z)$, which is monotonously increasing starting from zero, $\xi(0) = 0$. As soon as the dependence $m(\xi)$ is found from Eqs. (3.9), (3.10), the function $\xi(z)$ can be obtained by integration (analytical or numerical).

3.4 Exact solutions

It is not difficult to check, see also [18, 16], that the exact solution of Eqs. (3.12), (3.13) with the boundary conditions $\vec{b}_{1,2}(0) = \vec{b}^0_{1,2}$ is

$$\begin{aligned}\vec{b}_1 =&[\cos(\nu_0\xi)\,\cos(\nu\xi) - (\mathbf{n}\cdot\hat{\boldsymbol{\sigma}})\,\sin(\nu_0\xi)\,\sin(\nu\xi)\,]\,\vec{b}^0_1 + \\ &[\sin(\nu_0\xi)\,\cos(\nu\xi) + (\mathbf{n}\cdot\hat{\boldsymbol{\sigma}})\,\cos(\nu_0\xi)\,\sin(\nu\xi)\,]\,\vec{b}^0_2 \qquad (3.14)\\ \vec{b}_2 =&-[\sin(\nu_0\xi)\,\cos(\nu\xi) + (\mathbf{n}\cdot\hat{\boldsymbol{\sigma}})\,\cos(\nu_0\xi)\,\sin(\nu\xi)\,]\,\vec{b}^0_1 + \\ &[\cos(\nu_0\xi)\,\cos(\nu\xi) - (\mathbf{n}\cdot\hat{\boldsymbol{\sigma}})\,\sin(\nu_0\xi)\,\sin(\nu\xi)\,]\,\vec{b}^0_2 \qquad (3.15)\end{aligned}$$

where $\nu = |\boldsymbol{\nu}|$ is the scalar characterizing the strength of anisotropic diffraction and $\mathbf{n} = (n_1, 0, n_3) = \boldsymbol{\nu}/\nu$ is the real unit 3D vector. Two spatial frequencies, ν_0 and ν, are present in Eqs. (3.14), (3.15). One can check furthermore that $|\vec{b}_1(\xi)|^2 + |\vec{b}_1(\xi)|^2 = 1$.

Using Eqs. (3.14), (3.15), we find the contrast $m = 2\,(\vec{b}_1 \cdot \vec{b}^*_2)$ as a function of ξ,

$$\begin{aligned}m =& m_0\,\cos(2\nu_0\xi)\,\cos(2\nu\xi) - W_0\,\sin(2\nu_0\xi)\,\cos(2\nu\xi) - \\ &F_0\,\cos(2\nu_0\xi)\,\sin(2\nu\xi) - P_0\,\sin(2\nu_0\xi)\,\sin(2\nu\xi) \qquad (3.16)\end{aligned}$$

where $m_0 = m(0)$ is the input value of the contrast and W_0, F_0, P_0 are the input values of the following real scalar characteristics of the vectorial coupling:

$$W = |\vec{b}_1|^2 - |\vec{b}_2|^2 \quad F = \langle 1|(\mathbf{n}\cdot\hat{\boldsymbol{\sigma}})|1\rangle - \langle 2|(\mathbf{n}\cdot\hat{\boldsymbol{\sigma}})|2\rangle \quad P = 2\,\mathrm{Re}\,\langle 1|(\mathbf{n}\cdot\hat{\boldsymbol{\sigma}})|\,2\rangle \quad (3.17)$$

We have used here the conventional quantum-mechanic notation for the matrix elements, e.g., $\langle 1|(\mathbf{n}\cdot\hat{\boldsymbol{\sigma}})|2\rangle = \vec{b}^*_1 \cdot (\mathbf{n}\cdot\hat{\boldsymbol{\sigma}})\,\vec{b}_2$. As follows from Eqs. (3.17), W is the normalized difference of the beam intensities, F characterizes the polarization freedom degrees, and P describes a correlation of polarizations in the beams 1 and 2. To make this assertion more clear, we recall, see also [41, 42], that the real 3D vector $\mathbf{S}_i = \langle i|\hat{\boldsymbol{\sigma}}|i\rangle/|\vec{b}_i|^2$ $(i = 1, 2)$ is the unit Stokes vector for i^{th} beam, its components $(S_i)_{1,3}$ characterize the degree of linear polarization and the component $(S_i)_2$ characterizes the degree of ellipticity. In what follows, we shall provide the reader with particular examples of polarization characterization.

The structure of Eq. (3.16) makes us to expect that explicit relations for m, W, F, and P, that follow from Eqs. (3.14), (3.15), form a closed set. It is not difficult

to find out that

$$\begin{aligned} W =& m_0 \sin(2\nu_0\xi)\cos(2\nu\xi) + W_0 \cos(2\nu_0\xi)\cos(2\nu\xi) - \\ & F_0 \sin(2\nu_0\xi)\sin(2\nu\xi) + P_0 \cos(2\nu_0\xi)\sin(2\nu\xi) \qquad (3.18) \\ F =& m_0 \cos(2\nu_0\xi)\sin(2\nu\xi) - W_0 \sin(2\nu_0\xi)\sin(2\nu\xi) + \\ & F_0 \cos(2\nu_0\xi)\cos(2\nu\xi) + P_0 \sin(2\nu_0\xi)\cos(2\nu\xi) \qquad (3.19) \\ P =& -m_0 \sin(2\nu_0\xi)\sin(2\nu\xi) - W_0 \cos(2\nu_0\xi)\sin(2\nu\xi) - \\ & F_0 \sin(2\nu_0\xi)\cos(2\nu\xi) + P_0 \cos(2\nu_0\xi)\cos(2\nu\xi) \qquad (3.20) \end{aligned}$$

From here one finds algebraically that the quantity

$$I_p = m^2 + W^2 + F^2 + P^2 \qquad (3.21)$$

remains constant across the crystal, i.e., I_p is a new (in addition to I_0) integral of the set (3.1), (3.2). It involves the polarization degrees of freedom. One can show that, depending on polarizations of the input beams, I_p ranges from 1 to 2. It is worth mentioning that the unitary transformation (3.8) does not change the quantities W, F, and P, defined by Eqs. (3.17); instead of the new amplitudes $\vec{b}_{1,2}$ one can use the old amplitudes $\vec{a}_{1,2}$ in these equations.

The ξ-dependences given by the Eqs. (3.16), (3.18) – (3.20) include a great deal of information on the vectorial coupling. At the first sight, these oscillating dependences look unusual for the nonlocal response which is distinguished by a one-directional energy transfer [3]. Moreover, the possibility for the contrast m to change sign, that formally follows from Eq. (3.16), seems to be confusing. As a matter of fact, this feature is beyond of the field of applicability of the exact relations. It will be shown in the next section, that this field is restricted to the region of ξ where $m \geq 0$; within this region the propagation coordinate $z = z(\xi)$ ranges from 0 to ∞.

Particular cases

• *Transverse configuration.* Here $\nu_0 = 0$ and the relations (3.16), (3.18) – (3.20) acquire the following simplified form (with the only spatial frequency 2ν present):

$$m = m_0\cos(2\nu\xi) - F_0\sin(2\nu\xi) \qquad F = m_0\sin(2\nu\xi) + F_0\cos(2\nu\xi) \qquad (3.22)$$

$$W = W_0\cos(2\nu\xi) + P_0\sin(2\nu\xi) \qquad P = -W_0\sin(2\nu\xi) + P_0\cos(2\nu\xi) \qquad (3.23)$$

From here we have:

$$m^2(\xi) + F^2(\xi) = m_0^2 + F_0^2 \qquad W^2(\xi) + P^2(\xi) = W_0^2 + P_0^2 \qquad (3.24)$$

One sees that m is coupled only with F, W only with P, and instead of the integral $I_p = m^2+W^2+F^2+P^2$ we have two integrals, $h_0^2 = m^2+F^2$ and $g_0^2 = W^2+P^2$. It is interesting that evolution of the light contrast m is affected by the input value of the polarization characteristic F_0. Depending on F_0, the contrast can be an increasing or a decreasing function of ξ (and z) near the input face. A similar situation takes place for the intensity difference W; the sign of the derivative $dW/d\xi$ at $\xi = 0$, i.e., the direction of the energy transfer, is controlled by the sign of P_0. For any input values m_0, F_0, W_0, and P_0 the functions given by Eqs. (3.22) oscillate around zero.

Note that F_0 is expressed by the input intensities of the beams $I_{1,2}^0$ and the input Stokes vectors $\mathbf{S}_{1,2}^0$, $F_0 = I_1^0(\mathbf{n}\cdot\mathbf{S}_1^0) - I_2^0(\mathbf{n}\cdot\mathbf{S}_2^0)$. If the input polarizations are the same, $\mathbf{S}_1^0 = \mathbf{S}_2^0 = \mathbf{S}_0$, then $F_0 = W_0\,(\mathbf{n}\cdot\mathbf{S}_0)$ and $P_0 = m_0\,(\mathbf{n}\cdot\mathbf{S}_0)$. For $m_0 \ll 1$ the value of F_0 can be comparable with one, which means a strong effect of the polarization degrees on the spatial evolution of the contrast.

Let the input beams 1 and 2 be linearly polarized and α_1 and α_2 be the corresponding input polarization angles measured from the [001] axis, see Fig. 3.1b. Then the input values m_0, W_0, F_0, P_0 can be expressed as follows:

$$m_0 = \sqrt{1-W_0^2}\,\cos\alpha_- \qquad F_0 = n_1\Big(\cos\alpha_+\sin\alpha_- + W_0\,\sin\alpha_+\cos\alpha_-\Big) \tag{3.25}$$

$$W_0 = I_1^0 - I_2^0 \qquad P_0 = n_1\sqrt{1-W_0^2}\,\sin\alpha_+ \tag{3.26}$$

where $\alpha_\pm = \alpha_1 \pm \alpha_2$, $n_1 = \pm 1$ specifies the sign of the nonlocal response. Since the sum of the normalized intensities $I_1^0 + I_2^0 = I_0 = 1$, we have three independent variable input parameters, the normalized intensity difference W_0 and two polarization angles. The integrals h_0^2 and g_0^2 are also functions of these input parameters. The maximum values of h_0^2 and g_0^2, as functions of the angles, occur at $\alpha_{1,2} = \pi/4$ and equal unity. The corresponding minimum values are 0 and W_0^2; they take place at $\alpha_1 = \alpha_2 = \pi/2$.

To illustrate the consequences of Eqs. (3.25), (3.26), we consider again the situation when the input intensities are the same, $W_0 = 0$, whereas the input polarizations are almost perpendicular to each other, $\cos\alpha_- \ll 1$, $m_0 \ll 1$. Here we have $h_0^2 \simeq \cos^2\alpha_+$ and $g_0^2 \simeq \sin^2\alpha_+$. Hence the maximum attainable values of m and $|W|$ during two-wave coupling are controlled by the sum of the input polarization angles α_+. They can, by will, be made small or large, see also the next section.

• *Longitudinal configuration.* Here $\nu_0 = \nu$ and we obtain from Eqs. (3.16), (3.18)

the following explicit relations for m and W:

$$2m = m_0 - P_0 + (m_0 + P_0)\,\cos(4\nu\xi) - (W_0 + F_0)\,\sin(4\nu\xi) \tag{3.27}$$

$$2W = W_0 - F_0 + (m_0 + P_0)\,\sin(4\nu\xi) + (W_0 + F_0)\,\cos(4\nu\xi) \tag{3.28}$$

Furthermore one can find from Eqs. (3.19), (3.20) that the polarization characteristics P and F are expressed linearly by m and W:

$$P - P_0 = m - m_0 \qquad F - F_0 = W - W_0 \tag{3.29}$$

Again we have a strong effect of the polarization degrees of freedom on the coupling characteristics.

To illustrate the polarization effects covered by Eqs. (3.27) – (3.29), we consider the case of equal input intensities, $W_0 = 0$, and linear input polarizations. For the longitudinal optical geometry instead of the Eqs.(3.25)-(3.26) we have the following expressions:

$$m_0 = \sqrt{1 - W_0^2}\,\cos\alpha_- \qquad F_0 = n_3\Big(W_0\,\cos\alpha_+ \sin\alpha_- - \sin\alpha_+ \sin\alpha_-\Big) \tag{3.30}$$

$$W_0 = I_1^0 - I_2^0 \qquad P_0 = n_3\sqrt{1 - W_0^2}\,\cos\alpha_+ \tag{3.31}$$

We can use these equations to express m_0, F_0, and P_0 by the input polarization angles $\alpha_\pm$. Figure 3.2 shows the dependences $m(\xi)$ and $W(\xi)$ for several values of α_+ and a small input value of the contrast, $m_0 = \cos\alpha_- = 0.1$. For $35^\circ \lesssim \alpha_+ \lesssim 185^\circ$ the contrast decreases with ξ and turns to zero at a certain value of the effective coordinate ξ. When α_+ is increasing, the function $m(\xi)$ experiences a maximum before turning to zero. Then, within the interval $325^\circ \lesssim \alpha_+ \lesssim 35^\circ$, this function experiences oscillations (likewise the intensity difference $W(\xi)$) and remains positive for any ξ. The value of $[m(\xi)]_{max}$ reaches unity at $\alpha_+ \simeq 0$. For larger values of $185^\circ \lesssim \alpha_+ \lesssim 325^\circ$ the ξ-dependence of the contrast ends up again with a zero value. Thus, we have qualitative different behavior of $m(\xi)$ and $W(\xi)$ depending on the input polarization state.

• *The same input polarizations meeting the condition* $(\mathbf{n}\cdot\mathbf{S}_{1,2}^0) = \pm 1$. This special choice means that the input vectorial amplitudes, $\vec{a}_{1,2}^{\,0} \equiv \vec{b}_{1,2}^{\,0}$, are the eigen-vectors of the interaction matrix, i.e., the vectorial diffraction does not affect the polarization state. In other words, this case corresponds to scalar beam coupling. The necessary input Stokes vectors correspond to the linear input polarizations. In particular, for the T-geometry the corresponding polarization angles are $\alpha = \pm\pi/4$; for the L-configuration we have instead $\alpha = 0$ and $\pi/2$.

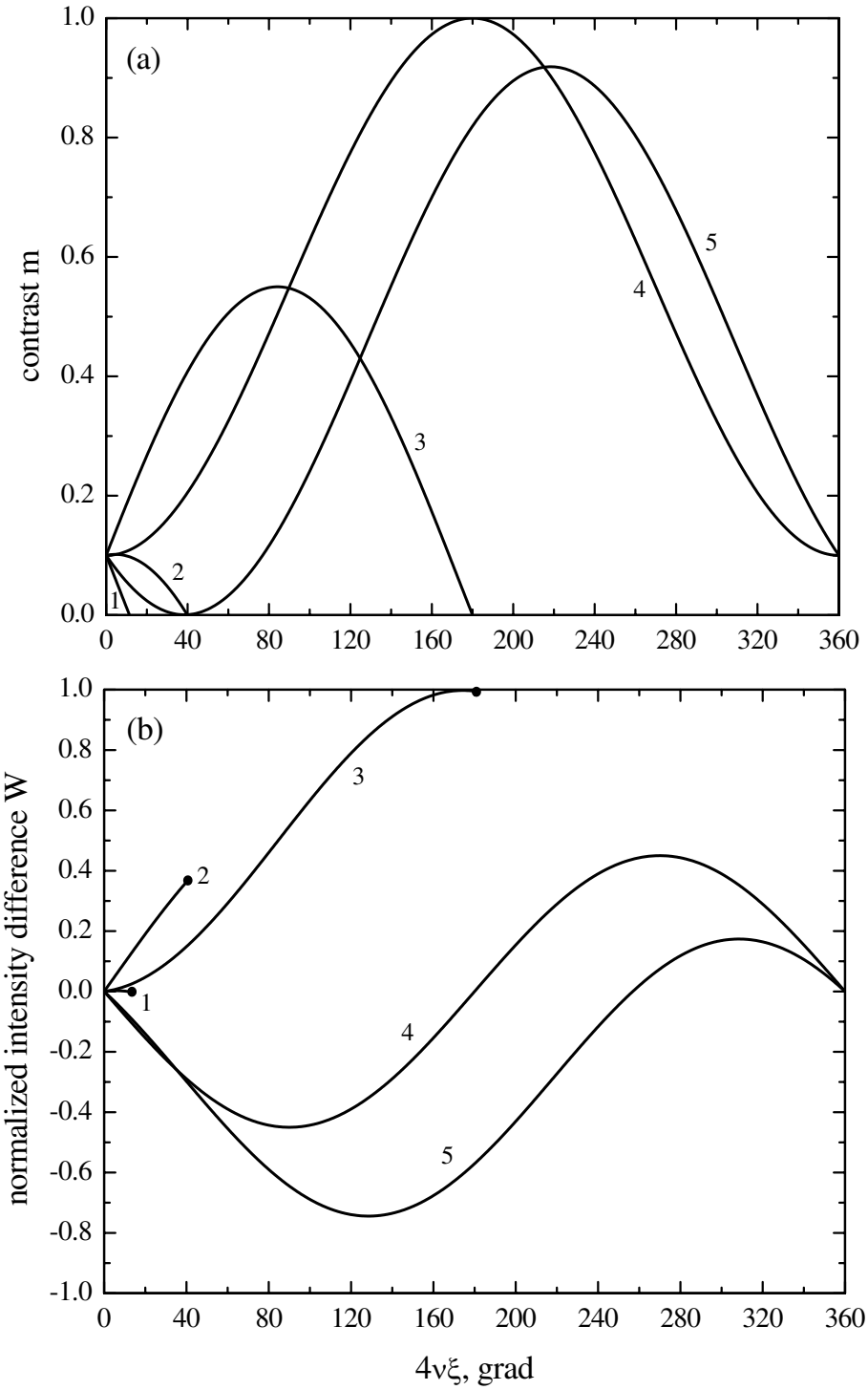

Fig. 3.2. Dependences $m(\xi)$ and $W(\xi)$ for the L-configuration, $m_0 = 0.1$, and $W_0 = 0$. The curves 1, 2, 3, 4, and 5 are plotted for the polarization angle $\varphi_+ = 0$, 90°, 180°, 270°, and 302°, respectively. The dots in the sub-figure (b) mark the limiting values of $W(\xi)$ which correspond to the condition $m(\xi) = 0$.

With our choice we have at the input: $F_0 = \pm W_0$, $P_0 = \pm m_0$. One can see from the Eqs. (3.19), (3.20) that these relations hold true during propagation, i.e., the variables m and W are sufficient for a complete description. These variables obey the relations

$$m = m_0 \cos[2(\nu_0 \pm \nu)\xi] - W_0 \sin[2(\nu_0 \pm \nu)\xi] \tag{3.32}$$

$$W = m_0 \sin[2(\nu_0 \pm \nu)\xi] + W_0 \cos[2(\nu_0 \pm \nu)\xi] \tag{3.33}$$

The only difference between the upper and lower signs in Eq. (3.32),(3.33) is the value of the effective coupling constant $\nu_0 \pm \nu$. In any case we have $m^2 + W^2 = 1$.

One more interesting particular case is the case of identical circular input polarization (left or right) where $(\mathbf{n} \cdot \mathbf{S}^0_{1,2}) = 0$ and $F_0 = P_0 = 0$. Only isotropic diffraction, which is characterized by the scalar ν_0, takes place here.

3.5 Transition from the ξ to the z-representation

The above exact solutions have been obtained in terms of the effective coordinate ξ which is coupled with the propagation coordinate z by Eq. (3.11). Since we know the dependence $m(\xi)$, see the Eqs. (3.16), (3.22), and (3.27), we can write down in the general case:

$$z = \frac{2}{Q|E_0|} \int_0^{\xi} \frac{d\xi'}{m(\xi')\, f[m(\xi')]} \tag{3.34}$$

This integral can be calculated analytically or numerically for any particular case. A step by step exhaustion of special cases is beyond the scope of this paper. Below we focus our attention on the most important features and consequences of the $\xi \to z$ transition.

Consider first the low-contrast case, $m \lesssim m_c$, where $f(m) \simeq 1$, see Section 2b. For the T-geometry, this condition can be fulfilled for any propagation distance if the input parameters are chosen in such a way that $h_0 = (m_0^2 + F_0^2)^{1/2} \lesssim m_c$. By setting $f = 1$ in Eq. (3.34) and using Eq. (3.22) for $m(\xi)$, one can obtain the following explicit analytic expression for $z(\xi)$:

$$z = \frac{1}{\Gamma_0} \ln \left[\frac{\tan(\nu\xi_\infty)}{\tan(\nu\xi_\infty - \nu\xi)} \right] \tag{3.35}$$

where $\Gamma_0 = h_0 Q \nu |E_0| > 0$, $\nu\xi_\infty = \arctan[\sqrt{(1-q_0)/(1+q_0)}]$, and $q_0 = F_0/h_0$. The increment Γ_0 characterizes the rate of spatial changes (in z) and ξ_∞ is the limiting

value of ξ that corresponds to the first zero point of the function $m(\nu\xi)$ and ranges from 0 to $\pi/2\nu$. The value of $\nu\xi_\infty$ is uniquely expressed by the input parameter q_0, see Fig. 3.3. The values $\nu\xi_\infty = \pi/2$, 1, and 0 correspond to $F_0 = -h_0$ ($m_0 = 0$), $F_0 = 0$ ($m_0 = h_0$), and $F_0 = h_0$ ($m_0 = 0$), respectively. The same input value of the contrast, m_0, corresponds generally to two different values of ξ_∞; this is caused by the fact that the system is not symmetric to the beam interchange in the case of non-local PR response.

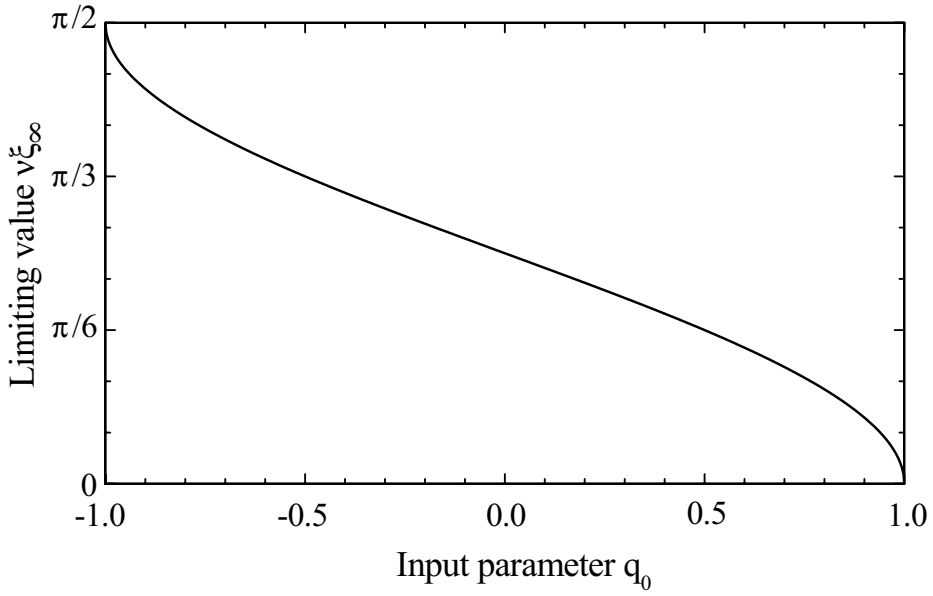

Fig. 3.3. The limiting value $\nu\xi_\infty$ versus the input parameter q_0 for the T-configuration.

Figure 3.4 shows the dependence $\nu\xi(z)$ for several representative values of $\nu\xi_\infty$. One sees that the effective coordinate ξ tends monotonously to its limiting value ξ_∞ when $z \to \infty$; with $\nu\xi_\infty$ approaching $\pi/2$ the growth of $\xi(z)$ becomes strongly slowed down in the regions of small and large z (where $m \simeq h_0$).

Next, using Eq. (3.35), we express by z the trigonometric functions $\sin(2\nu\xi)$ and $\cos(2\nu\xi)$ entering Eqs. (3.22), (3.23) for m, F, W, and P,

$$\sin(2\nu\xi) = \frac{m_0}{h_0}\,\frac{\sinh(\Gamma_0 z) + q_0\coth(\Gamma_0 z) - q_0}{\coth(\Gamma_0 z) + q_0\sinh(\Gamma_0 z)} \tag{3.36}$$

$$\cos(2\nu\xi) = \frac{1 + q_0[\sinh(\Gamma_0 z) + q_0\coth(\Gamma_0 z) - q_0]}{\coth(\Gamma_0 z) + q_0\sinh(\Gamma_0 z)} \tag{3.37}$$

In the limit $\Gamma_0 z \to \infty$ we have from here $\sin(2\nu\xi_\infty) = m_0/h_0$ and $\cos(2\nu\xi_\infty) = F_0/h_0$.

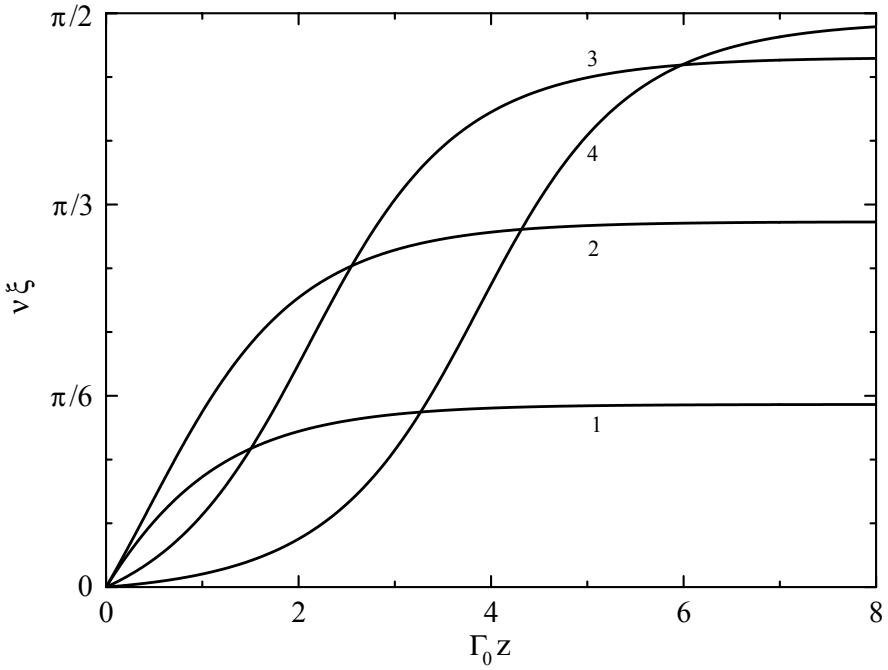

Fig.3.4. Dependence $\nu\xi(z)$ for the T-geometry. The curves 1, 2, 3, and 4 are plotted for $\nu\xi_\infty = 0.5$, 1.0, 1.45, and 1.55, respectively.

Now, using Eqs. (3.22), (3.23), and (3.36), (3.37), one can describe analytically the dependences of m, F, W, and P on the propagation coordinate z. We restrict ourselves to the functions $m(z)$ and $F(z)$,

$$\frac{m}{m_0} = \frac{1}{\coth(\Gamma_0 z) + q_0 \sinh(\Gamma_0 z)} \qquad \frac{F}{F_0} = \frac{1 + q_0^{-1} \tanh(\Gamma_0 z)}{1 + q_0 \tanh(\Gamma_0 z)} \tag{3.38}$$

The input parameter $q_0 = F_0/\sqrt{F_0^2 + m_0^2}$ entering the right-hand sides of these expressions ranges from -1 to 1. Figure 3.5 illustrates the possible scenarios of the spatial behavior of the light contrast m. For $q_0 > 0$, the contrast monotonously decreases with z tending to zero; if, additionally, $m_0 \ll h_0$ (i.e., $q_0 \simeq 1$), then $m \simeq m_0 \exp(-\Gamma_0 z)$. In the case $q_0 < 0$, the function $m(z)$ experiences first a maximum (where $m = h_0$ and $F = 0$) and then tends to zero; if, additionally, $m_0 \ll h_0$, then $m \simeq m_0 \exp(\Gamma_0 z)$ at the initial stage of growth.

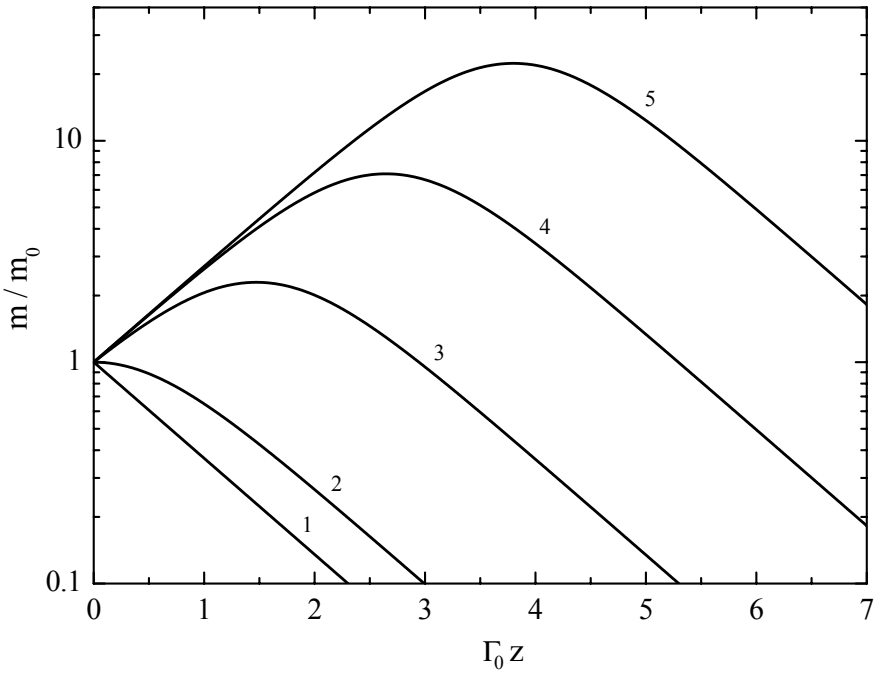

Fig.3.5. The ratio m/m_0 versus $\Gamma_0 z$ for the T-geometry; the curves 1, 2, 3, 4, and 5 are plotted for $q_0 = 1$, 0, -0.9, -0.99, and -0.999, respectively.

Qualitatively, the above features are not surprising for nonlocal response; the regime with an intermediate maximum corresponds, e.g., to the energy transfer from the initially weakest to the strongest beam. Specific properties (which are not available in the scalar case) are here the possibility to restrict the growth of m from above and to affect the rate and direction of the energy transfer by the polarization degrees of freedom.

To gain an impression about the expected rates of spatial changes, we produce some numerical estimates relevant to ac-experiments with BTO crystals. By setting $|s| = 4 \cdot 10^{-4}$ V^{-1}, $|E_0| = 20$ kV/cm, and $Q = 6$, we have $\nu Q|E_0| \approx 50$ cm^{-1}. Despite the fact that $h_0 \ll 1$, the product $\Gamma_0 z = h_0 Q \nu |E_0|\, z$ can easily be made considerably larger than unity.

We continue our analysis of the low-contrast case for the T-configuration with specification of the values of F, W, and P that take place for $\Gamma_0 z \gg 1$ ($\xi \to \xi_\infty$). These limiting values are

$$F_\infty = \sqrt{m_0^2 + F_0^2} \qquad W_\infty = \frac{W_0 F_0 + m_0 P_0}{\sqrt{m_0^2 + F_0^2}} \qquad P_\infty = \frac{P_0 F_0 - m_0 W_0}{\sqrt{m_0^2 + F_0^2}} \tag{3.39}$$

The limiting value of F coincides, indeed, with that prescribed by Eqs. (3.38).

It is important that the inequalities $m(z), |F(z)| \le h_0 \ll 1$ do not impose

severe restriction on the variation range of $W(z)$ and $P(z)$. To make this point clear, we consider the case of equal input intensities ($W_0 = 0$) and linear input polarizations. The condition $h_0 \equiv \sqrt{m_0^2 + F_0^2} \ll 1$ can be fulfilled here only for $\cos^2\alpha_\pm \ll 1$; this means either $\alpha_1 \simeq \pi/2$, $\alpha_2 \simeq 0$ ($\alpha_+ \simeq \pi/2$) or $\alpha_1 \simeq \pi$, $\alpha_2 \simeq \pi/2$ ($\alpha_+ \simeq 3\pi/2$). Correspondingly, we have $h_0^2 \simeq \cos^2\alpha_+ + \cos^2\alpha_-$ and $q_0 = cos\alpha_+/\sqrt{\cos^2\alpha_+ + \cos^2\alpha_-}$. On the other hand, we have here from Eqs. (3.25), (3.27), and (3.39), $W_\infty = \sqrt{1-q_0^2}\,\sin\alpha_+ \simeq \pm\sqrt{1-q_0^2}$, $P_\infty = q_0\,\sin\alpha_+ \simeq \pm q_0$. Thus, the signs of W_∞ and P_∞ are controlled by the sign of $\sin\alpha_+$ and the absolute value $|W_\infty|$ (or $|P_\infty|$) can approach unity.

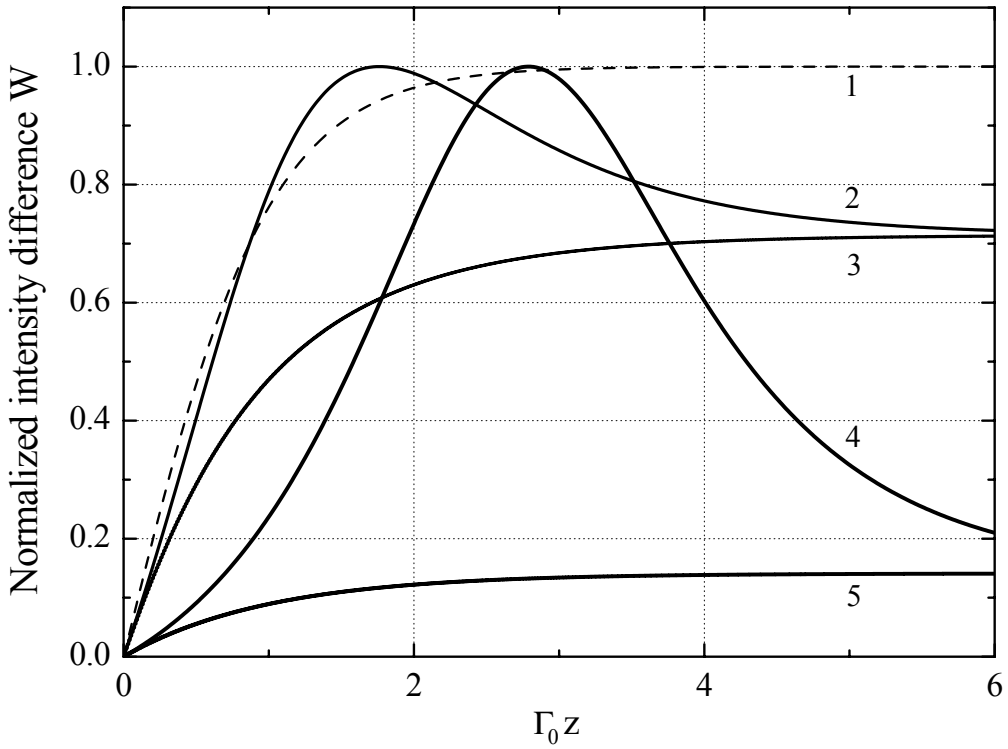

Fig.3.6. The normalized intensity difference W versus $\Gamma_0 z$ for the T-geometry and $\sin\varphi_+ \simeq 1$; the lines 1, 2, 3, 4, and 5 correspond to $q_0 = 0$, -0.7, 0.7, -0.99, and 0.99, respectively.

Figure 3.6 exhibits the coordinate dependence of the normalized intensity difference. For $q_0 > 0$ we have a monotonous growth of $W(z)$ up to the value of $\sqrt{1-q_0^2}$. When q_0 changes its sign, the function $W(z)$ shows a maximum ($W_{max} = 1$) and approaches then the same limiting value. The nearer q_0 to -1, the stronger is the shift of this maximum to the right.

Now we extend our study to the whole-contrast range with emphasis on the region

$m_c \lesssim m \leq 1$ where the function $f(m)$ experiences a strong saturation. The main expected advantage of this region is the maintenance of high values of light contrast (because of decreasing the rate of energy exchange) during recording. Large values of m, necessary for recording, mean identical input polarizations and comparable intensities. We consider therefore the case where the input polarization vectors are the eigen-vectors of the interaction matrix, see Eqs. (3.32). Then, using Eq. (3.34) and the notation $\nu_\pm = \nu_0 \pm \nu$, we obtain for $m(z)$,

$$\nu_\pm |E_0| z = \int_m^{m_0} \frac{dm}{Qmf(m)\sqrt{1-m^2}} \tag{3.40}$$

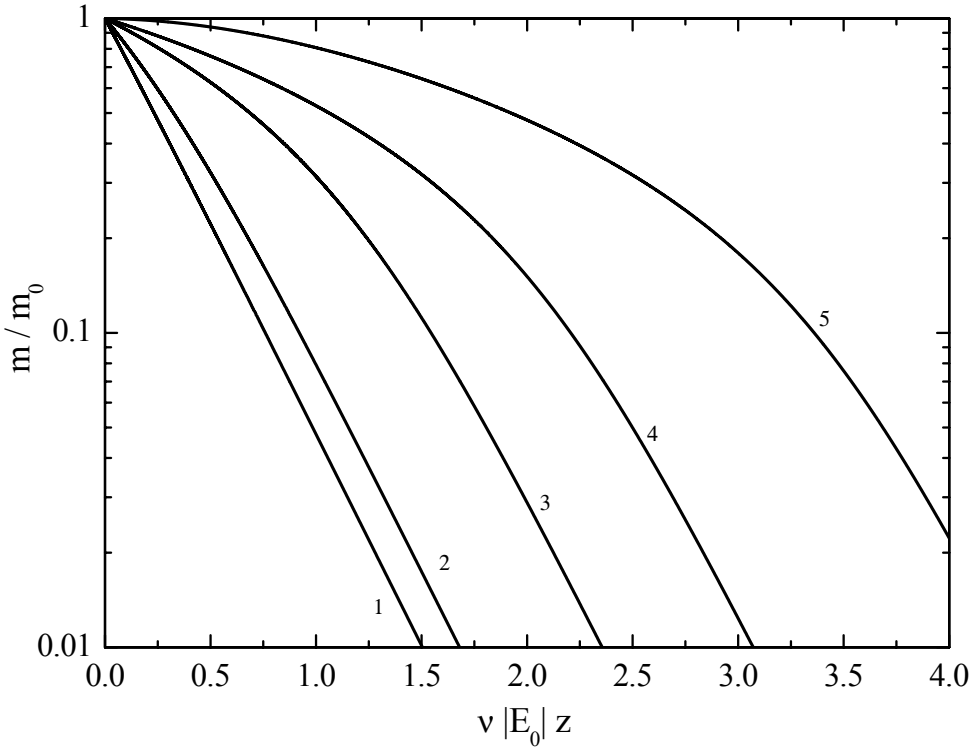

Fig.3.7. Dependence $m(z)$ for the scalar case in the whole contrast range; the curves 1 – 5 are plotted for $m_0 = 0.01$, 0.1, 0.4, 0.7 and 1.

Figure 3.7 shows the coordinate dependence of the ratio m/m_0 in a logarithmical scale for several values of m_0 ranging from 0.01 (low-contrast region) to unity. For $m_0 = 0.01$ we have a steep linear decrease which is described by the single-exponential function $m/m_0 = \exp(-Q\nu_\pm|E_0|z)$. With increasing m_0, decrease of $m(z)/m_0$ becomes less and less pronounced at the initial stage. As a result, the interval where the recorded index grating remains approximately uniform, in-

creases remarkably with m_0. If we define the uniformity range z_u by the equality $m(z_u) = m_0/2$, then we can see that z_u becomes larger by a factor of ≈ 7 when m_0 is increasing from 0.01 to 1. This result may have important consequences for the effects relevant to the grating recording [24, 25]. Moreover, strong coupling effects and recording of quasi-uniform gratings can co-exist in one sample.

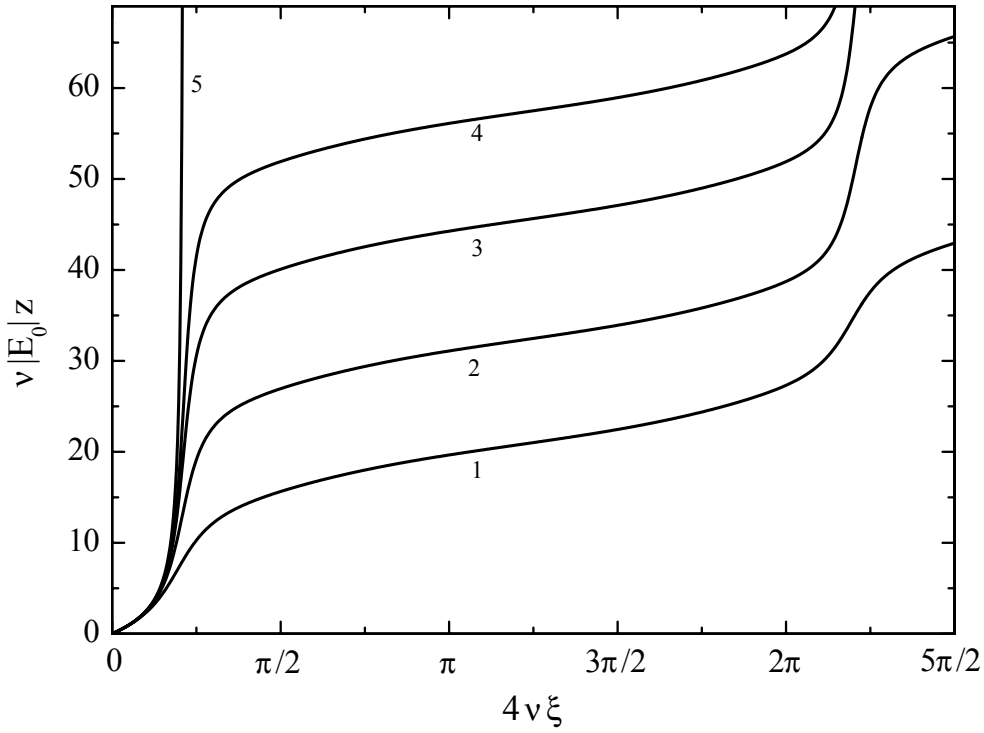

Fig. 3.8. Dependence $z(\xi)$ for the L-configuration. The curves 1 - 5 correspond to $\varphi_+ = 33.8°$, $34.0°$, $34.6°$, $34.8°$, and $35.1°$. Other input parameters are specified in the caption of Fig. 3.2

Lastly, we consider the $\xi \to z$ transformation for the L-configuration. As we know, the contrast m becomes in this case a positive, oscillating function of ξ within an interval of the input polarization angles, see Fig. 3.2(a). This means indeed crossover to periodic dependences $m(z)$ and $W(z)$ and to a qualitatively new dependence $z(\xi)$. Figure 3.8 shows what happens with the function $z(\xi)$ when the input polarization angle α_+ increases from $31.8°$ to $35.1°$ (transition from periodic to non-periodic states occurs at $\alpha_+ \simeq 35°$). For $185° < \alpha_+ < 325°$ the function $z(\xi)$ is finite and single-valued. It shows a linear growth superimposed by strong periodic oscillations. The average slope tends to infinity when α_+ is approaching $35°$. At $\alpha_+ = 35.1°$ the propagation coordinate z tends to infinity for $\xi \to \xi_\infty$; the limiting

value ξ_∞ is, as earlier, the first zero-point of the function $m(\xi)$.

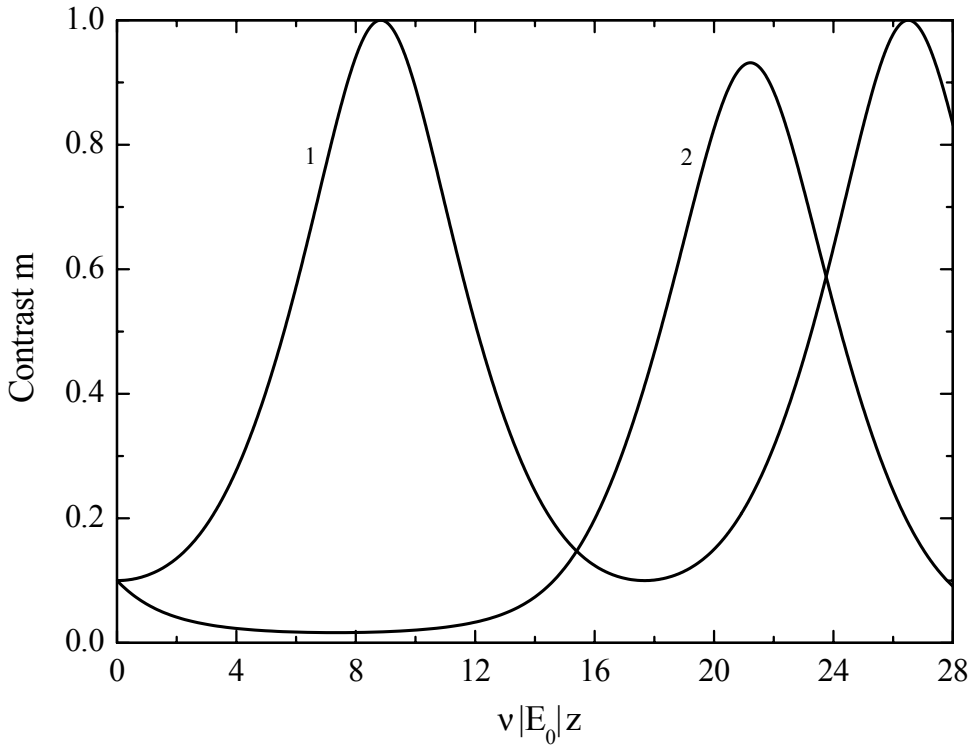

Fig. 3.9. Dependence $m(z)$ for the L-geometry. Curves 1 and 2 are plotted for $\varphi_+ = 34°$ and 35.1°, respectively.

The lines 1 and 2 in Fig. 3.9 correspond to the lines 4 and 5 in Fig. 3a and exhibit a periodic behavior of the light contrast. Nontrivial and strong periodic oscillations of $m(z)$ originate from harmonic oscillations of $m(\xi)$. The oscillation period for the curve 2 is considerably larger than that for the curve 1. This is fully due to the proximity of the curve 5 in Fig. 3a to zero. With α_+ increasing, this curve touches the horizontal; the period of oscillation becomes here infinitely long and the periodic oscillations of $m(z)$ transform into a monotonous decrease.

3.6 Resume

The main findings of this Chapter can be summarized as follows:
– Vectorial two-wave coupling caused by the ac-enhanced nonlinear response possesses different quantitative properties in the regions of low ($0 \leq m \lesssim m_c \ll 1$) and high ($m_c \lesssim m \leq 1$) light contrast m. The narrow low-contrast range is optimal for

the spatial amplification of weak waves, while the high-contrast region is preferable for recording of refractive index gratings.

– The light interference fringes experience neither bending nor tilting during vectorial two-wave coupling under an ac-field; this result is valid in the whole contrast region irrespectively of the input polarizations of the interacting waves.

– Owing to this property of the light fringes and under certain assumptions on the coupling characteristics (applicable, e.g., to BTO crystals and crystals of the $\bar{4}3m$ point group), the nonlinear problem of vectorial coupling is reduced to a linear problem of vectorial Bragg diffraction; the latter admits an exact solution.

– Analysis of the auxiliary linear problem has shown the presence of an additional (to the energy conservation law) integral of motion which involves the polarization degrees of freedom; this conclusion is not restricted to any particular contrast range.

– Consideration of particular cases relevant for the experiments has allowed to reveal the possibilities for further simplifications of the vectorial equations and predict a number of new regimes with a strong influence of the input polarizations on the output energy and polarization characteristics.

Chapter 4

Linear signal detection with cubic photorefractive crystals under an ac-field: influence of coupling effects

4.1 Introduction

One of the important application of PR crystals is the detection of small-amplitude ultrasonic vibrations. This technique is used for nondestructive testing, quality control, and condition monitoring. The surface under inspection is usually optically rough resulting in a scattered beam with a random distribution of intensity and phase. When this beam is made to interfere with a reference beam in a conventional interferometer, the small phase shift produced by ultrasound is nearly averaged out, which results in low sensitivity. PR two-beam coupling is known as the simplest solution of this problem. In this technique, two beams, a reference beam and a phase-modulated object beam, couple in a PR crystal. The output intensities of the beams appear to be linearly modulated by the input phase.

The linear detection of small phase excursions via PR two-beam coupling were investigated in different publications. Many of them deal with conventional scalar two-beam coupling. The vectorial character of beam coupling was taken into account only recently [15, 24, 25]. In these works, the linear detection theories incorporate correctly the vectorial effects, but use the linear-in-contrast approximation or the assumption of a spatially uniform index grating. Usually, the linear-in-contrast

approximation is not valid in experiments and applications, where input beams with equal intensities and polarizations are used. The assumption of constant grating amplitude is well justified only for thin crystals where the effects of beam coupling between the pump beams are negligible and the detection quality is weak. In thick crystals, beam coupling effects become very strong and the changing of the grating amplitude along the crystal is sufficiently large. In this Chapter we use the vectorial beam coupling theory, developed in Chapter 3, to describe the linear detection in thick crystals and for the whole range of the light contrast.

4.2 Exact solution under phase scanning

Let us have the space-charge field grating which is recorded under the assumptions made in Chapter 3. After the grating is recorded, a phase change φ is introduced for a short time (compared with the PR response time) into one of the input beams. The phase change does not affect the space-charge field, so that only the readout conditions are varying. The output intensities of the readout beams are modulated by the input phase.

To describe the influence of the input phase change on the output intensities, we use the exact solution given by Eqs.(3.14)-(3.15) with new boundary conditions, which correspond to the phase scanning procedure (the amplitudes of the readout beams we denote as $\vec{p}_{1,2}$):

$$\vec{p}_1(0) = \vec{a}_1(0)\, e^{i\varphi} \quad \vec{p}_2(0) = \vec{a}_2(0) \tag{4.1}$$

Then we introduce the new amplitudes $\vec{r}_{1,2}(z)$ similarly to Eq.(3.8),

$$\vec{r}_{1,2}(z) = \exp[-i(\boldsymbol{\kappa}\cdot\hat{\boldsymbol{\sigma}})\, z]\, \vec{p}_{1,2}(z) \tag{4.2}$$

Solution of the Eqs.(3.6),(3.7) for the readout beams with the boundary conditions (4.1) follows from the Eqs.(3.14),(3.15) by the replacement of $\vec{b}_{1,2}(\xi)$ by $\vec{r}_{1,2}(\xi)$ and $\vec{b}^0_{1,2}$ by $\vec{r}^0_{1,2} = \vec{r}_{1,2}(0) = \vec{p}_{1,2}(0)$. This is true because of the phase varying does not change the grating amplitude $E_K(z)$ and the variable $\xi(z)$. Combining Eqs.(3.14),(3.15) and (4.1), we obtain:

$$\vec{r}_{1,2}(\xi) = \vec{b}_{1,2}(\xi) + \vec{R}_{1,2}(\xi)(e^{i\varphi} - 1), \text{where} \tag{4.3}$$

$$\vec{R}_1(\xi) = [\cos(\nu_0\xi)\, \cos(\nu\xi) - (\mathbf{n}\cdot\hat{\boldsymbol{\sigma}})\, \sin(\nu_0\xi)\, \sin(\nu\xi)]\, \vec{b}^0_1 \tag{4.4}$$

$$\vec{R}_2(\xi) = -[\sin(\nu_0\xi)\, \cos(\nu\xi) + (\mathbf{n}\cdot\hat{\boldsymbol{\sigma}})\, \cos(\nu_0\xi)\, \sin(\nu\xi)]\, \vec{b}^0_1 \tag{4.5}$$

By returning to the amplitudes $\vec{p}_{1,2}(\xi)$, we have:

$$\vec{p}_{1,2} = \exp[i(\boldsymbol{\kappa}\cdot\hat{\boldsymbol{\sigma}})\,z]\,\vec{r}_{1,2} = \vec{a}_{1,2} + (e^{i\varphi}-1)\,\exp[i(\boldsymbol{\kappa}\cdot\hat{\boldsymbol{\sigma}})\,z]\,\vec{R}_{1,2} \tag{4.6}$$

The introduction of the phase change leads to the appearance of additional terms in the output amplitudes $\vec{p}_{1,2}$. These terms are proportional to $(e^{i\varphi}-1)$; they depend on the input intensities and polarizations of the recording beams and also on the optical configuration in question. As a consequence, the output intensities of the readout beams $\tilde{I}_{1,2}$ have constant on φ and φ-dependent parts.

Substituting the Eqs. (3.14),(3.15) and (4.3)-(4.5) in Eq.(4.6) and using the notation (3.17) we obtain the expressions for the output intensities with and without phase scanning, $\tilde{I}^d_{1,2}$ and $I^d_{1,2}$ consequently:

$$\begin{aligned}\tilde{I}^d_{1,2} = |\vec{p}_{1,2}(\xi_d)|^2 = I^d_{1,2} \mp \big(1-\cos\varphi\big)\Big[&\frac{m_0}{2}\sin(2\nu_0\xi_d)\cos(2\nu\xi_d)\\ &+ \mathrm{Re}J_0\cos(2\nu_0\xi_d)\sin(2\nu\xi_d)\Big]\\ &\mp \sin\varphi\Big[\cos(2\nu_0\xi_d)\sin(2\nu\xi_d)\mathrm{Im}J_0\Big]\end{aligned} \tag{4.7}$$

$$\begin{aligned}2I^d_{1,2} = 1 &\pm W_0\cos(2\nu_0\xi_d)\cos(2\nu\xi_d) \pm m_0\sin(2\nu_0\xi_d)\cos(2\nu\xi_d)\\ &\pm P_0\cos(2\nu_0\xi_d)\sin(2\nu\xi_d) \mp F_0\sin(2\nu_0\xi_d)\sin(2\nu\xi_d)\end{aligned} \tag{4.8}$$

where $\xi_d \equiv \xi(z=d)$, d is the crystal thickness and $J_0 = \vec{a}^{\,0*}_1(\boldsymbol{n}\cdot\hat{\boldsymbol{\sigma}})\vec{a}^{\,0}_2$ is a characteristic of phase scanning. One can check that $|J_0| \leqslant 1/2$. For linearly polarized input beams (real vectors $\vec{a}^{\,0}_{1,2}$), the factor J_0 is real and the difference $\tilde{I}^d_{1,2} - I^d_{1,2}$ varies as $(1-\cos\varphi)$. The same situation takes place when input beams are polarized identically. In other cases, J_0 is complex and the difference $\tilde{I}^d_{1,2} - I^d_{1,2}$ contains both type of terms varying as, $(1-\cos\varphi)$ and $\sin\varphi$.

Note, that the introduction of the phase change into the second beam leads to the sign and index change in the Eqs.(4.4)-(4.5): $\vec{b}^{\,0}_1 \leftrightarrow \vec{b}^{\,0}_2$, $\vec{R}_{1,2} \leftrightarrow -\vec{R}_{2,1}$; also the sign before $\sin\varphi$ in Eq.(4.7) changes. The Eqs.(4.3), (4.8) are the vectorial generalization of the equations for the scalar grating translation technique [43].

4.3 Linear detection of small signals

The phase scanning procedure is widely used for the linear detection of weak and fast signals. In our case, small varying of the input phase, $\varphi << 1$, plays the role of

such a signal. Then the output intensities can be represented as a linear functions of the phase change:

$$\tilde{I}^d_{1,2} = A_{1,2} + B_{1,2}\,\varphi \tag{4.9}$$

The coefficients $A_{1,2}$ and $B_{1,2}$ are called background intensities and modulation coefficients. The expressions for them follow from the Eqs.(4.7), (4.8):

$$A_{1,2} = \frac{1}{2} \pm \frac{1}{2}\Big[W_0 \cos(2\nu_0\xi_d)\cos(2\nu\xi_d) + m_0 \sin(2\nu_0\xi_d)\cos(2\nu\xi_d) + P_0 \cos(2\nu_0\xi_d)\sin(2\nu\xi_d) - F_0 \sin(2\nu_0\xi_d)\sin(2\nu\xi_d)\Big] \tag{4.10}$$

$$B_{1,2} = \mp \cos(2\nu_0\xi_d)\sin(2\nu\xi_d)\mathrm{Im}J_0 \tag{4.11}$$

Linear detection is possible if the modulation coefficients $B_{1,2}$ are nonzero. With $\nu \neq 0$ (the presence of anisotropic diffraction) this condition is fulfilled when the factor $\mathrm{Im}J_0$ differs from zero, what is valid only for differently polarized input light beams and at least one of them must be elliptically polarized.

To optimize the conditions for linear detection, we have to maximize first the value of $|B_{1,2}|$ and then, if possible, to minimize $A_{1,2}$ to increase the parameter $|B_{1,2}|/\sqrt{A_{1,2}}$. This parameter controls the signal-noise ratio because the actual noise is proportional to the square root of the background intensity.

The coefficients $A_{1,2}$ and $B_{1,2}$ are functions of input beam characteristics, the crystal thickness d and the external field amplitude E_0. The exact form of these functions depends on the particular optical configuration. The simplest case corresponds to the transverse geometry, where $\nu_0 = 0$. In this case, the expressions for $A_{1,2}$ and $B_{1,2}$ acquire the form:

$$A_{1,2} = \frac{1}{2} \pm \frac{1}{2}\Big[W_0 \cos(2\nu\xi_d) + P_0 \sin(2\nu\xi_d)\Big] \tag{4.12}$$

$$B_{1,2} = \mp \sin(2\nu\xi_d)\,\mathrm{Im}J_0 \tag{4.13}$$

We consider the following useful optimization scheme. Let the input beam amplitudes be $\vec{a}^0_1 = (1/2, \exp(i\delta)/2)$ and $\vec{a}^0_2 = (1/\sqrt{2}, 0)$. This means that the first input beam is elliptically polarized (with the ellipticity $\tan(\delta/2)$), the second beam is linearly polarized in the x direction (see Fig.1), the input beam intensities are the same, and the input contrast $m_0 = 1/\sqrt{2}$. Then we have from the Eqs.(4.12), (4.13):

$$A_{1,2} = \frac{1}{2} \pm \frac{1}{2\sqrt{2}} n_1 \sin(2\nu\xi_d)\cos\delta \tag{4.14}$$

$$B_{1,2} = \mp \frac{1}{2\sqrt{2}} n_1 \sin(2\nu\xi_d)\sin\delta \tag{4.15}$$

where the first component of the vector $\boldsymbol{n}$, $n_1 = \pm 1$, specifies the sign of the nonlocal response (see Sec.3.4). To maximize $|B_{1,2}|$ we set $\delta = \pi/2$. For this δ and chosen crystal thickness d we use an amplitude of the external field E_0 which maximizes the factor $\sin(2\nu\xi_d)$.

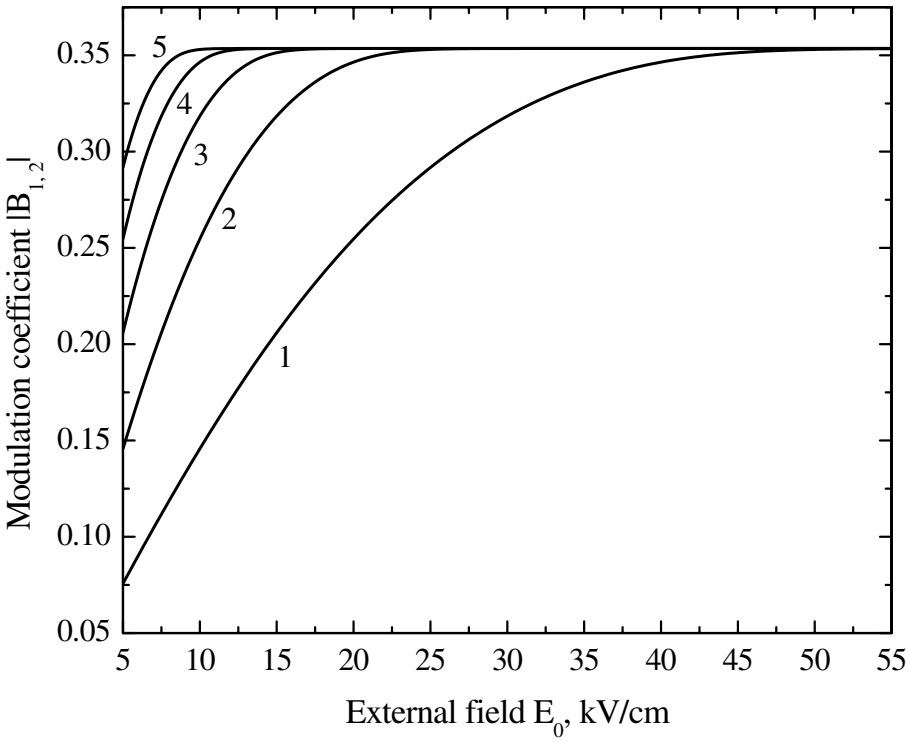

Fig. 4.3. Dependence of $|B_1|$ on external field amplitude E_0. The curves 1, 2, 3, 4 and 5 are plotted for the crystal thicknesses $d = 1$, 2, 3, 4, 5, mm, respectively.

Figure 3 shows the dependences $|B_{1,2}(E_0)|$ for different crystal thicknesses d and typical BTO parameters (see Chapter 3). One can see, that the larger is the crystal thickness, the smaller is the external field amplitude, at which $|B_{1,2}|$ reaches its maximal value $2^{-3/2}$. The parameters $|B_{1,2}|/\sqrt{A_{1,2}}$ equal $1/2$, when the modulation coefficients are maximal (see Eqs.(4.14), (4.15)).

The obtained values of $B_{1,2}$ are approximately 44% larger than the one reported for the linear detection with polarization filtering [25]. Using more complicated optimization schemes and other optical configurations can give higher values of the modulation coefficients $|B_{1,2}|$ and the parameters $|B_{1,2}|/\sqrt{A_{1,2}}$. The limiting value of the modulation coefficients is $1/2$, what follows from the definition of the parameter J_0 and Eq.(4.11),.

4.4 Linear detection of small signals by polarization filtering

As we have mentioned, the imaginary part of the parameter J_0 equals to zero if both input light beams are linearly polarized. Then the modulation coefficients $B_{1,2}$ also equals to zero and linear signal detection becomes impossible. However, as was recently shown, accomplishing the detection scheme by a polarization filtering allows performing the detection with linear polarized beams [25]. Let us have two linearly polarized input beams with polarization angles α_1 and α_2. A polarization filter $\mathbf{P}$, which transmits a linearly polarized component of outgoing beams, is placed behind the crystal. The filter is characterized by the unit vector $\vec{e}_p$, the orientation of which is determined by the angle β. All angles are measured from the [001] axis, see Fig.4.4 Then the output intensities after the polarization filter are equal to $|\vec{e}_p \cdot \vec{p}_{1,2}(d)|^2$.

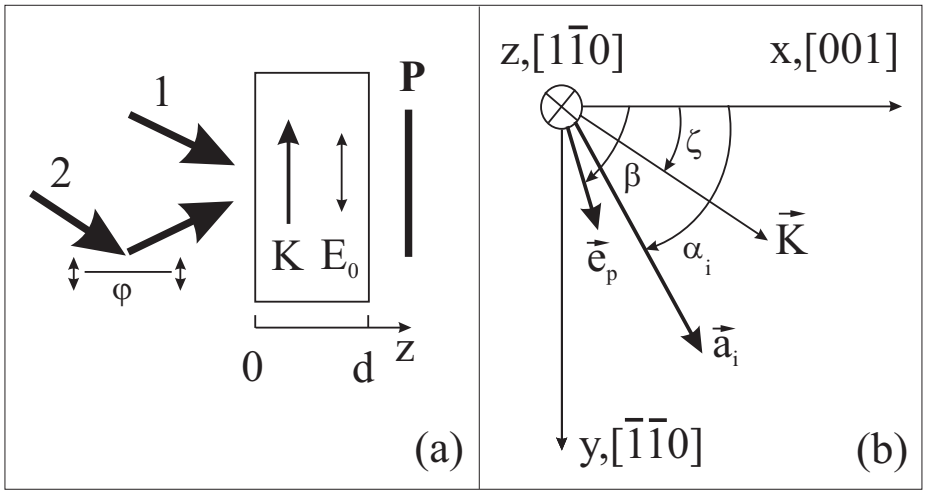

Fig. 4.4. Scheme of the linear detection with polarization filtering.

Representing the filtered output intensities in the same form as in Eq.(4.9) and using the Eqs.(4.3)-(4.6) we get for the background intensities $A_{1,2}$ and modulation coefficients $B_{1,2}$:

$$A_{1,2} = \cos^2(\kappa d)\left(\vec{e}_p \cdot \vec{b}_{1,2}\right)^2 + \frac{\sin^2(\kappa d)}{\kappa}\left[\vec{e}_p\,(\boldsymbol{\kappa} \cdot \hat{\boldsymbol{\sigma}})\,\vec{b}_{1,2}\right] \tag{4.16}$$

$$B_{1,2} = \frac{\sin(2\kappa d)}{\kappa}\left[\left(\vec{e}_p \cdot \vec{R}_{1,2}\right)\left(\vec{e}_p\,(\boldsymbol{\kappa} \cdot \hat{\boldsymbol{\sigma}})\,\vec{b}_{1,2}\right) - \left(\vec{e}_p \cdot \vec{b}_{1,2}\right)\left(\vec{e}_p\,(\boldsymbol{\kappa} \cdot \hat{\boldsymbol{\sigma}})\,\vec{R}_{1,2}\right)\right] \tag{4.17}$$

where the vectors $\vec{b}_{1,2}$ and $\vec{R}_{1,2}$ are taken at $\xi = \xi_d$. The necessary condition for linear detection is $B_{1,2} \neq 0$. As in the previous section, we will try first to maximize

the value of $|B_{1,2}|$ and then to minimize $A_{1,2}$. Here the coefficients $|A_{1,2}|$ and $|B_{1,2}|$ are functions not only of the parameters d, E_0 and the characteristics of the input beams, $\alpha_{1,2}$, $I^0_{1,2}$, but also of the angle β. The particular dependences vary for different optical configurations. Below we optimize the linear signal detection for the T- and L- optical configurations and using material parameters typical for BTO crystals.

4.4.1 Optimization for T-geometry

For the transverse configuration, the coefficient B_1 equals:

$$B_1 = -\frac{1}{4} n_1 \sqrt{1 - W_0^2} \sin(2\,\kappa\, d)\, \sin(2\,\nu\, \xi_d) \cos(2\,\beta) c_+ \tag{4.18}$$

where $c_+ = \cos(\alpha_+)$ and $\alpha_+ = \alpha_1 + \alpha_2$. The factor $n_1 = \pm 1$ is the first component of the vector $\boldsymbol{n}$. We omit the expression for the background intensity A_1 since it looks very cumbersome. The coefficient B_2 which characterizes the second beam, can be found from relation: $B_2(n_1) = -B_1(-n_1)$. As follows from Eq.(4.18) $|B_1| \leqslant 1/4$.

Due to large number of variable parameters, the optimization procedure of the coefficients A_1 and B_1 is rather complicated. The most simple case corresponds to the input beams with equal polarizations and intensities, $\alpha_1 = \alpha_2 = \alpha$ and $I^0_1 = I^0_2$. Then we have $W_0 = 0$, $m_0 = 1$, $F_0 = 0$, $\alpha_+ = 2\alpha$ and then $m(d) = \cos(2\nu\xi_d)$ (see Eq.(3.16)). For the absolute value of the coefficient $|B_1|$ we obtain from Eq.(4.18):

$$\begin{aligned} |B_1| =& \frac{1}{4} \cos(2\nu\xi_d)\, \left| \sin(2\,\kappa\, d)\, \cos(2\,\beta) c_+ \right| = \\ & \frac{1}{4} \sqrt{1 - m^2(d)}\, \left| \sin(2\,\kappa\, d)\, \cos(2\,\beta) c_+ \right| \end{aligned} \tag{4.19}$$

To study the influence of the coupling effects, we compare our formulae with the results, obtained under the assumption of constant grating amplitude [25]. To get the formula for the modulation coefficient $|\bar{B}_1|$ from [25], we should substitute $\xi_d = E_K d$ in Eq.(4.18):

$$|\bar{B}_1(d)| = \frac{1}{4} \left| \sin(2\,\kappa\, d) \sin(2\,\nu\, E_K d) \right| \tag{4.20}$$

.

where $E_K = 0.62 E_0$ is the grating amplitude for the unit light contrast, see Chap.2. In the following, the modulation coefficients and background intensities, which correspond to this assumption, we denote with overlined letters. There are four combinations of α and β that maximize $|B_1|$, i.e. $\alpha = 0, \beta = 0; \alpha = \pi/2, \beta = \pi/2; \alpha = 0, \beta = \pi/2; \alpha = \pi/2, \beta = 0$. The values of the angles that differ by π are equivalent.

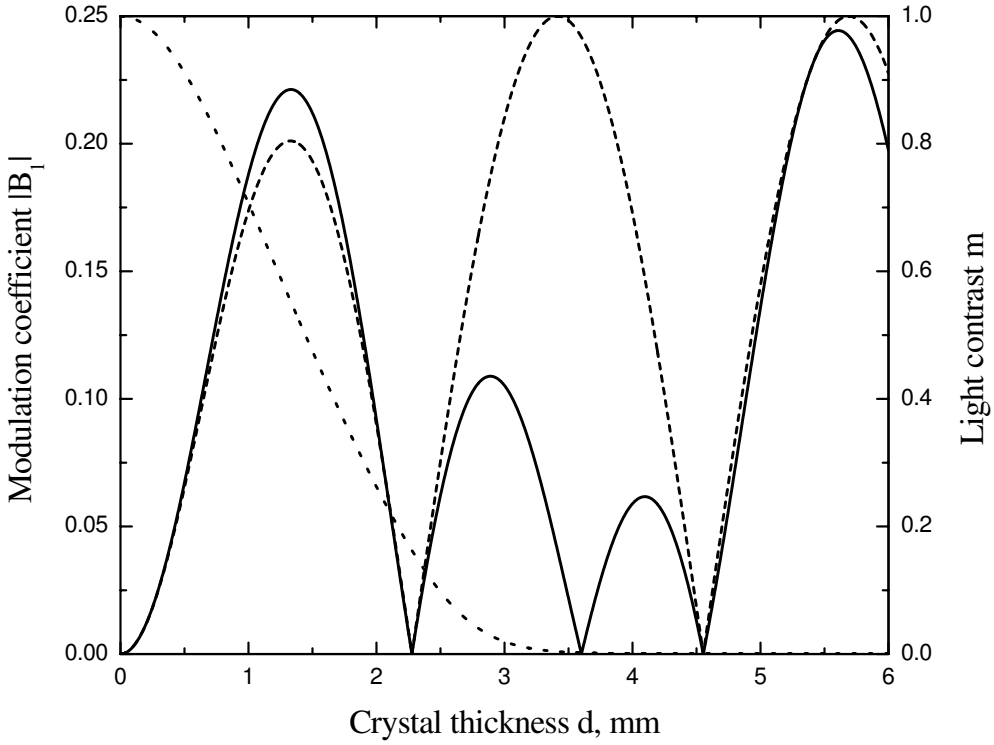

Fig. 4.5. Dependences of the modulation coefficients $|B_1|$ and $|\bar{B}_1|$ on the crystal thickness d. Solid and dashed lines correspond to the nonuniform and constant index grating consequently, dotted line is the light contrast m.

Figure 4.5 shows the dependences of $|B_1|$ (solid line) and $|\bar{B}_1|$ (dashed line) on crystal thickness d after the angular optimization. The dotted line in Fig.4.5 corresponds to the light contrast $m(d)$. One can see that for small thickness ($d \lesssim 2.3$ mm) the dependences $|B_1(d)|$ and $|\bar{B}_1(d)|$ practically coincide. The difference between the first maxima is approximately 10%. For large crystal thickness $d \geq 0.3$ mm our results deviate strongly from that obtained for the constant grating amplitude. The coefficient $|\bar{B}_1(d)|$ changes as the product of two harmonic functions with spacial frequencies 2κ and $2\nu E_K$, while $|B_1(d)|$ tends to the function $|\sin(2\kappa d)|$, what follows from Eq.(4.19) and the light contrast behavior, see Fig.5. The maxima of $|B_1(d)| = 1/4$ occur at the points $d_l \approx (\pi/2 + \pi l)/2\kappa$, with $l = 1, 2, ...$ Changing the external field amplitude, E_0, in the range from 10 to 50 kV/cm, only shifts the extrema of $|B_1(d)|$ and $|\bar{B}_1(d)|$ along the d axis. Their maximal values vary approximately 1%.

For the angles α, β which optimize B_1, the background intensities for the nonuniform and uniform index grating, A_1 and $\bar{A}_1$, are:

$$A_1(d) = \frac{1}{4}\Big[1 + \cos(2\nu\xi_d)\cos(2\kappa d)\Big] \; = \frac{1}{4}\Big[1 + m(d)\cos(2\kappa d)\Big] \tag{4.21}$$

$$\bar{A}_1(d) = \frac{1}{4}\Big[1 + \cos(2\,\nu\,E_K d)\cos(2\kappa d)\Big] \tag{4.22}$$

The coefficient $A_1(d)$ reaches its minimal zero value at $m = 1$ and $\cos(2\kappa d) = -1$. Due to the coupling effects, $m(d)$ equals to unity only near the input crystal face, where $d = 0$. Therefore, the minimum of A_1 is larger than zero.

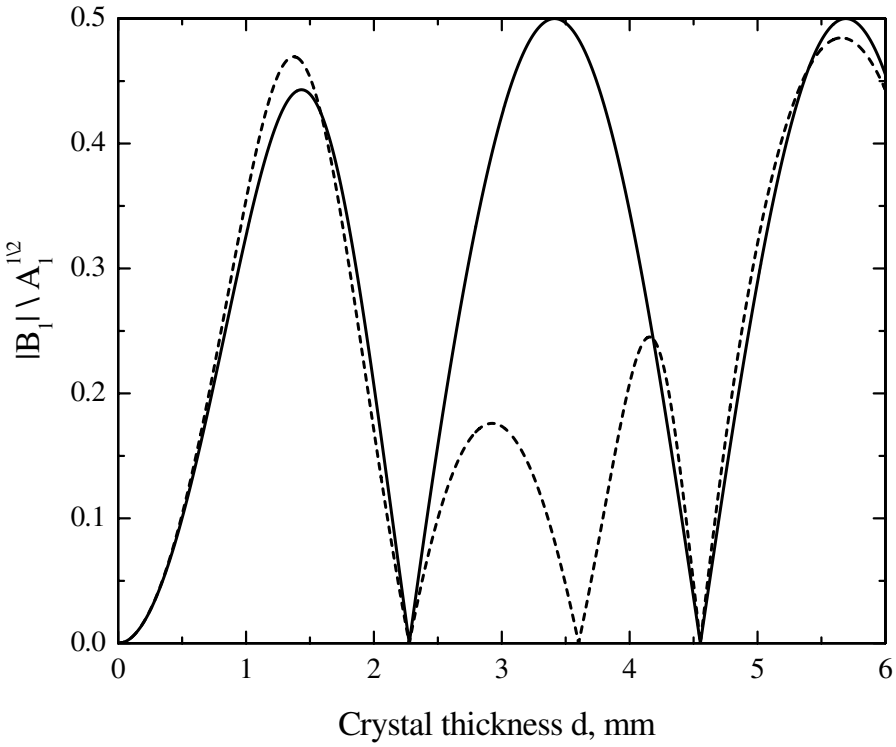

Fig. 4.6. Dependences of the parameters $|B_1|/\sqrt{A_1}$ on the crystal thickness d. Solid and dashed lines correspond to the nonuniform and constant index grating consequently.

We compare in Fig.4.6 the parameter $|B_1|/\sqrt{A_1}$ for the cases of nonuniform (solid line) and uniform (dashed line) index grating. For small crystal thickness these dependences are very close. For large values of d, where the light contrast is small, $m \ll 1$, the background intensity A_1 is close to $1/4$, as follows from Eq.(4.21), and the parameter $|B_1(d)|/\sqrt{A_1(d)}$ tends to the function $|\sin(2\kappa d)|/2$. It reaches the value of $1/2$ at the same points, where the maxima of $|B_1(d)|$ occur. It is remarkable, that taking into account coupling effects leads to simpler dependences of $|B_1|$ and

the parameter $|B_1|/\sqrt{A_1}$ on the crystal thickness d than under the assumption of constant grating amplitude.

4.4.2 Optimization for L-geometry

Here we have $\nu_0 = -n_3\nu$ and $\nu_1 = \kappa_1 = 0$ and then the coefficient B_1 has the form:

$$B_1 = -\frac{1}{4} n_3 \sqrt{1 - W_0^2}\, \sin(2\,\kappa\, d)\, \sin(2\,\nu\,\xi_d)\ \sin(2\,\beta)(s_+ - s_-) \tag{4.23}$$

where $s_\pm = \sin(\alpha_\pm)$, $\alpha_- = \alpha_1 - \alpha_2$ and the factor $n_3 = \pm 1$ is the third component of the vector $\boldsymbol{n}$. Eq.(4.23) is very similar to Eq.(4.18) for the transverse geometry. The main difference between them is the limiting value of $|B_1|$. For the L-configuration, the modulation coefficient is proportional to the factor $|s_+ - s_-|$ which maximal value is 2. Therefore, the limiting value of $|B_1|$ is 1/2 here, what is two-times larger than in the T-case. The next difference is the appearance of an extra factor of 1/2 in the parameters κ, ν. It means that we need two-times-thicker crystals to get the same values of the modulation coefficients as in the transverse geometry.

The simplest situation corresponds to the identical linearly polarized input light beams: $I^0_{1,2} = 1/2$, $\alpha_1 = \alpha_2 = \alpha$. Then $W_0 = 0$, $m_0 = 1$, $F_0 = 0$, $\alpha_+ = 2\alpha$, $\alpha_- = 0$ and $m(d) = 1 + (c_+ - 1)\sin^2(2\nu\xi_d)$. In this case B_1 has the form:

$$B_1 = -\frac{1}{4} n_3\ \sin(2\,\kappa\, d)\, \sin(2\,\nu\,\xi_d)\ \sin(2\,\beta) s_+ \tag{4.24}$$

To maximize the coefficient $|B_1|$ we set $\alpha_+ = \pm\pi/2$ and $\beta = \pm\pi/4$. The dependence $|\bar{B}_1(d)|$ for the constant index grating can be obtained from Eq.(4.24) in the same way as in Eq.(4.20). With the optimum angles, the dependences $|B_1(d)|$ and $|\bar{B}_1(d)|$ look very similar to the ones from Figure 4.5. The only qualitative difference is that the maxima of $|B_1(d)|$ and $|\bar{B}_1(d)|$ are reached in twice thicker crystals.

We omit again the expressions for the background intensities A_1, $\bar{A}_1$ and show in Fig.4.7 the dependences of the parameter $|B_1|/\sqrt{A_1}$ on thickness d, for the cases of nonuniform (solid line) and constant (dashed line) index grating. For small crystal thickness, as expected, the dependences $|B_1|/\sqrt{A_1}$ and $|\bar{B}_1|/\sqrt{\bar{A}_1}$ are practically the same. In the region where the light contrast $m(d)$ is close to zero, the maximum of $|B_1|/\sqrt{A_1}$ equals 0.71, what is 42% larger than the maximum of the corresponding dependence for the constant index grating. In contrast to the transverse geometry, see Fig.6, the assumption of the nonuniform grating amplitude does not simplify the optimization of the parameter $|B_1|/\sqrt{A_1}$.

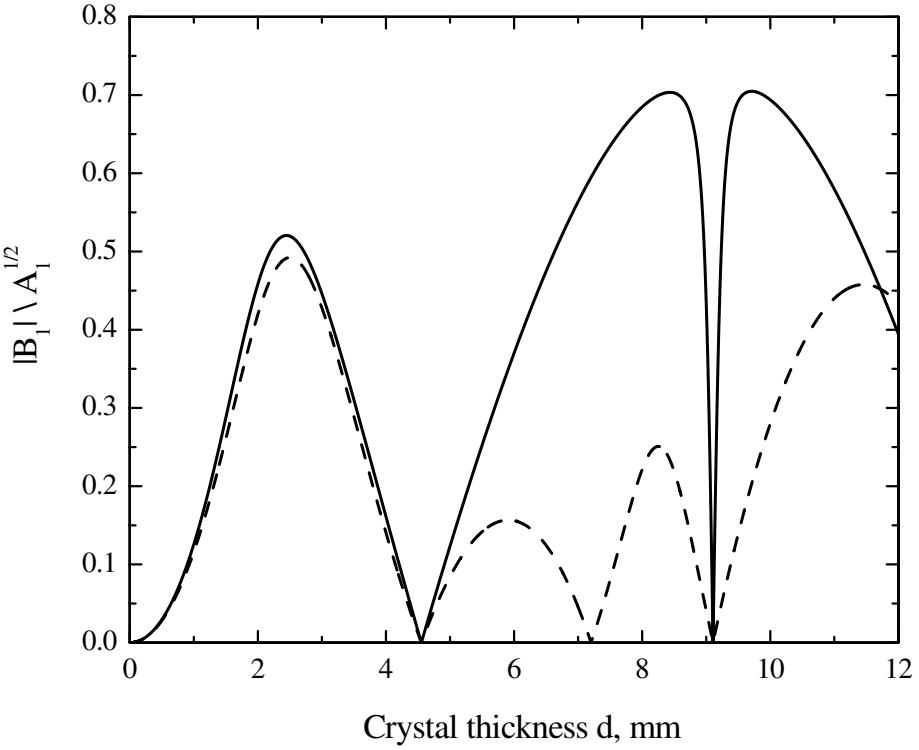

Fig. 4.7. Dependences of the parameter $|B_1(d)|/\sqrt{A_1(d)}$ on the crystal thickness d. Solid and dashed lines correspond to the nonuniform and constant index grating consequently.

Until now we have considered the simplest values of the input polarization angles. In these cases, the light contrast m decreases from unity to zero along the crystal and the optimum (maximum) modulation coefficient $|B_1|$ and parameter $|B_1|/\sqrt{A_1}$ correspond to very small output values of m. The maximum of $|B_1|$ is limited here by 1/4. However, as we have mentioned, this limiting value of $|B_1|$ can be exceeded by using specially polarized input light beams.

To illustrate the optimization of the linear detection in this case, we use input beams with equal intensities ($W_0 = 0$) and such polarization angles $\alpha_\pm$, which yield the light contrast oscillation along the crystal, see Chapter 3. For instance, we take $\alpha_- = 84^0$ and $\alpha_+ = 332^0$. Then the input light contrast is small, $m_0 = 0.1$, and the factor $|s_+ - s_-|$ in Eq.(4.23) equals approximately 1.46.

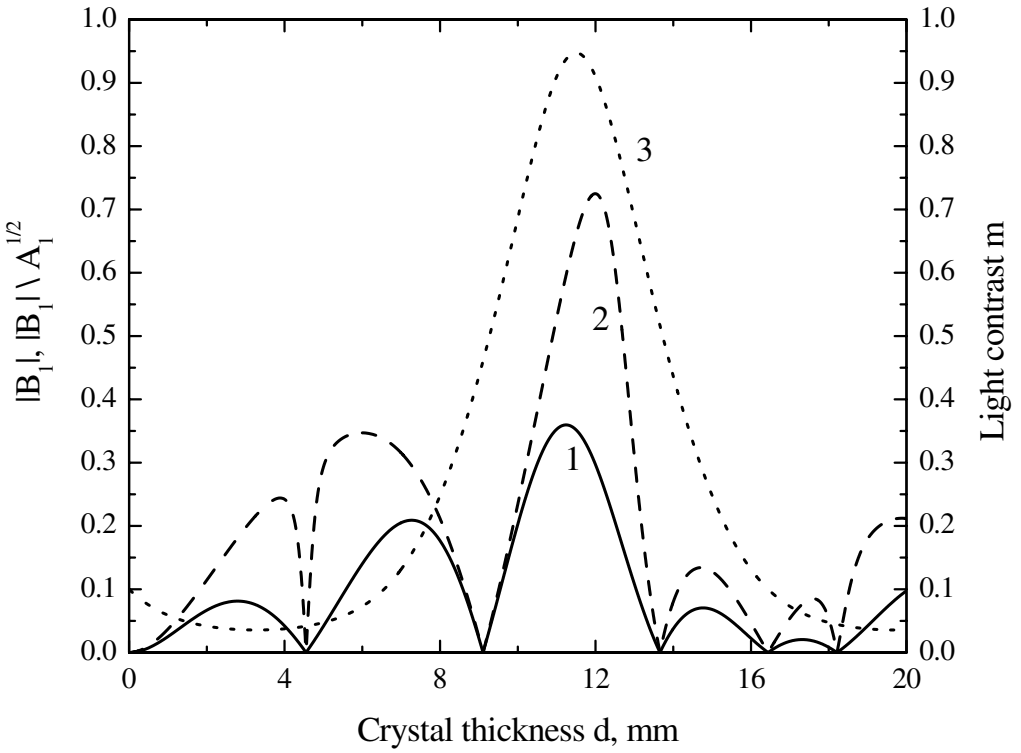

Fig. 4.8. The curves 1, 2, 3 are the dependences of $|B_1(d)|$, $|B_1(d)|/\sqrt{A_1(d)}$ and $m(d)$ respectively. The input parameters are $m_0 = 0.1$, $W_0 = 0$, $\alpha_+ = 332^0$, $E_0 = 15kV/cm$.

Figure 4.8 shows the dependences of m (dotted line), the parameter $|B_1|/\sqrt{A_1}$ (dashed line) and the modulation coefficient $|B_1|$ (solid line) on crystal thickness d. The light contrast $m(d)$ oscillates between 0.04 and 0.95 with a period of approximately 12 mm. The maxima of $|B_1| \approx 0.36$ and $|B_1|/\sqrt{A_1} \approx 0.72$ occur in the vicinity of the maxima of the light contrast dependence. The obtained values of the modulation coefficient and the parameter $|B_1|/\sqrt{A_1}$ are larger than for linear detection with polarization filtering and comparable with ones from the Sec.4.3. In that way, the L-geometry is found to have certain advantages for linear detection with thick crystals in comparison with the T-geometry.

4.5 Resume

We have used the vectorial wave coupling theory to describe linear signal detection in cubic PR crystals under ac-enhancement. In contrast to previous studies, we have investigated the influence of the coupling effects on the characteristics of the linear signal detection such as, modulation coefficient and background intensity.

We have optimized the linear detection with polarization filtering for T- and L-optical configurations. We have found that coupling effects are not critical in thin crystals and lead to only 10% decrease of the maximal value of the modulation coefficient. In thick crystals, the influence of the coupling effects becomes very strong. The calculated values of the modulation coefficient for nonuniform and constant index grating differ by several times. The predicted maxima of the modulation coefficient are approximately 10% larger than for thin crystals. It is also remarkable, that the optimization procedure for linear detection is considerably simpler without the assumption of constant grating amplitude.

The developed vectorial theory of the linear detection allows us to predict that a maximum value of the modulation coefficient twice larger than reported earlier [25] is achievable. In particular, the performed optimization scheme was made for the L-geometry, thick crystals ($d \approx 10$ mm) and specially linearly polarized input light beams. The calculated exceeding of the modulation coefficient was about 41%.

We have shown, that linear detection in the case of nonlocal response is also possible without polarization filtering. For this purpose we suggest to use elliptically polarized input light beams. The simple optimization scheme has been made for T-geometry, thin crystal and one circular and one linear polarized input beams. With these conditions, we have got the maximum of the modulation coefficient 44% larger than reported.

Chapter 5

Polarization properties of light-induced scattering in BTO crystals: Theory and experiment for the diagonal geometry

5.1 Introduction

Light-induced scattering of holographic type in PR crystals is due to the formation of secondary noise gratings between light noise, originating from various inhomogeneities, and the pump waves [1, 44] The light scattering in PR crystals can be phase-matched or not. In the first case, only those components of the light noise are amplified which are parametrically coupled to the pump waves. Phase-matched scattering may be realized when two or more pump waves propagate inside the sample. This leads to narrow scattering patterns like rings [45, 46], open lines [47] and bright dots [48, 49]. In the presence of one pump wave, phase-matched scattering can be realized in crystals with anisotropy [44]. It results in ring-like scattering patterns [50, 51, 52, 53, 54].

The induced birefringence in sillenites is weak even for high applied voltages. Therefore non-phase-matched scattering is observed if there is only one pump wave [40, 55, 56, 57]. That is, many different components of the light noise may be amplified by interaction with the pump wave. This interaction may be considered as two-beam coupling between the pump wave and the individual scattered plane waves if the amplification is weak. In this case, the intensity distribution of the scattered

light follows the angular dependence of the two-beam coupling amplification [**?**]. Since the scattered beam intensity is much smaller than the pump beam intensity, the space-charge grating formation can be considered in the low-contrast approximation.

Various publications investigate angular distributions of the light scattering in ac-biased sillinites crystals [40, 55, 56, 57], but the polarization states of scattered waves were never analyzed theoretically. In this Chapter we apply the vectorial beam coupling theory in the low-contrast approximation to describe the polarization properties of small-angle, light-induced scattering in BTO crystals.

5.2 Basic relations

Assuming that the scattered waves are weak compared to the pump beam propagating along the $[\bar{1}10]$ crystal axis, we neglect pump depletion and consider the spatial amplification of a scattered wave travelling at a small angle to $[\bar{1}10]$. The scheme of an experiment is shown in Fig.5.1.

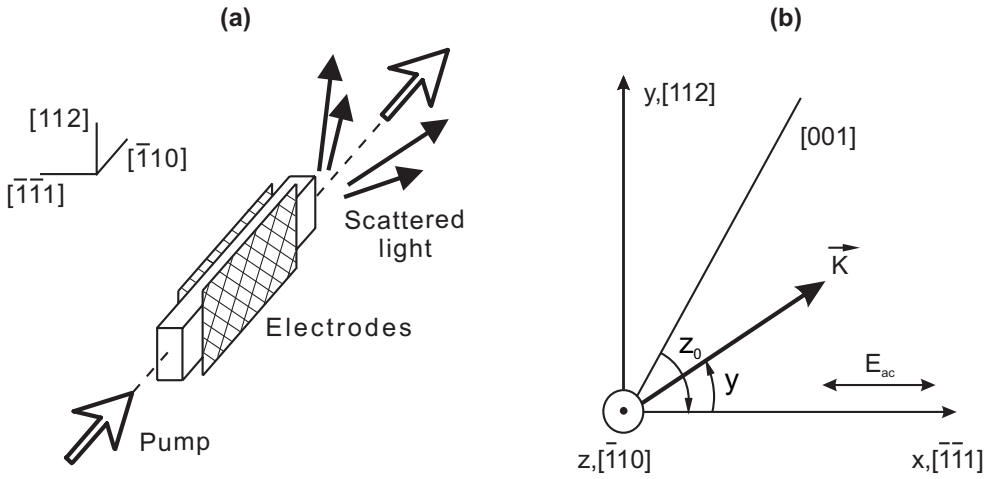

Fig. 5.1. (a) Schematic of an experiment on light-induced scattering. (b) Geometrical diagram for the diagonal geometry, ψ is the polar angle measured from the $[\bar{1}\bar{1}1]$ axis, ζ_0 is the angle between $[\bar{1}\bar{1}1]$ and [001], and the propagation direction is $[\bar{1}10]$.

The vectorial complex amplitudes of the pump and scattered waves we denote by $\vec{e}$ and $\vec{a}$, respectively, they are generally functions of the propagation coordinate z. The pump intensity is normalized in such a way that $|\vec{e}|^2 = 1$, this means that $\vec{e}$ can be treated as a unit polarization vector. Within the paraxial approximation,

the light amplitudes possess only x and y components. The amplitude $\vec{a} = \vec{a}(z)$ is governed by the ordinary first-order differential equation [16]

$$\frac{d\vec{a}}{dz} - i(\boldsymbol{\kappa} \cdot \hat{\boldsymbol{\sigma}})\,\vec{a} = Q|E_0 \cos\psi|\,(\vec{a} \cdot \vec{e}^{\,*})\,(\nu_0 + \boldsymbol{\nu} \cdot \hat{\boldsymbol{\sigma}})\vec{e} \tag{5.1}$$

As we have neglected the pump depletion, the governing equation for the pump amplitude $\vec{e} = \vec{e}(z)$ differs from Eq. (5.1) for $\vec{a}$ only by the absence of the right-hand side. This means that $\vec{e}$ changes only because of optical activity and the ac-field induced optical anisotropy. From now on we restrict ourselves to the so-called diagonal configuration ($\vec{E}_0 \parallel [\bar{1}\bar{1}1] \perp [\bar{1}10]$), distinguished by the strongest nonlinear coupling [58, 59]. Furthermore, the relevant experimental characteristics are obtained just for this geometry.

Here, in contrast to Chapters 3,4, the coupling parameters ν_0 and $\boldsymbol{\nu}$, in contrast to the parameters $\kappa_{1,3}$, generally include not only the electro-optic but also elasto-optic contributions [60, 61, 62]; the later result from the deformations produced by the space-charge field via the piezo-effect. Furthermore, in specifying these parameters we should keep in mind that the grating vector $\vec{K}$ is not parallel to the diagonal $[\bar{1}\bar{1}1]$. In other words, these parameters are functions of the angle ψ between $\vec{K}$ and $[\bar{1}\bar{1}1]$. If we provisionally neglect the elasto-optic contributions, then the nonzero coupling parameters are

$$\nu_{0,3} = \pm\frac{s}{2}\,\cos(\zeta_0 + \psi) \qquad \nu_1 = s\,\sin(\zeta_0 + \psi) \tag{5.2}$$

where $\zeta_0 = \arctan(\sqrt{2}) \simeq 54.7°$, see Fig. 5.1(b). For $\psi = 0$ we have $\kappa_1/\nu_1 = \kappa_3/\nu_3 = E_0$. The elasto-optic contributions modify the dependences $\nu_{0,1,3}(\psi)$. A relevant example for BTO crystals is presented in Fig. 5.2. One sees that the components ν_0 and ν_3 are subjected to the strongest changes. Anyhow the relative changes do not exceed 40%. In the subsequent calculations of the scattering characteristics (section 4) the elasto-optic contributions are taken into consideration.

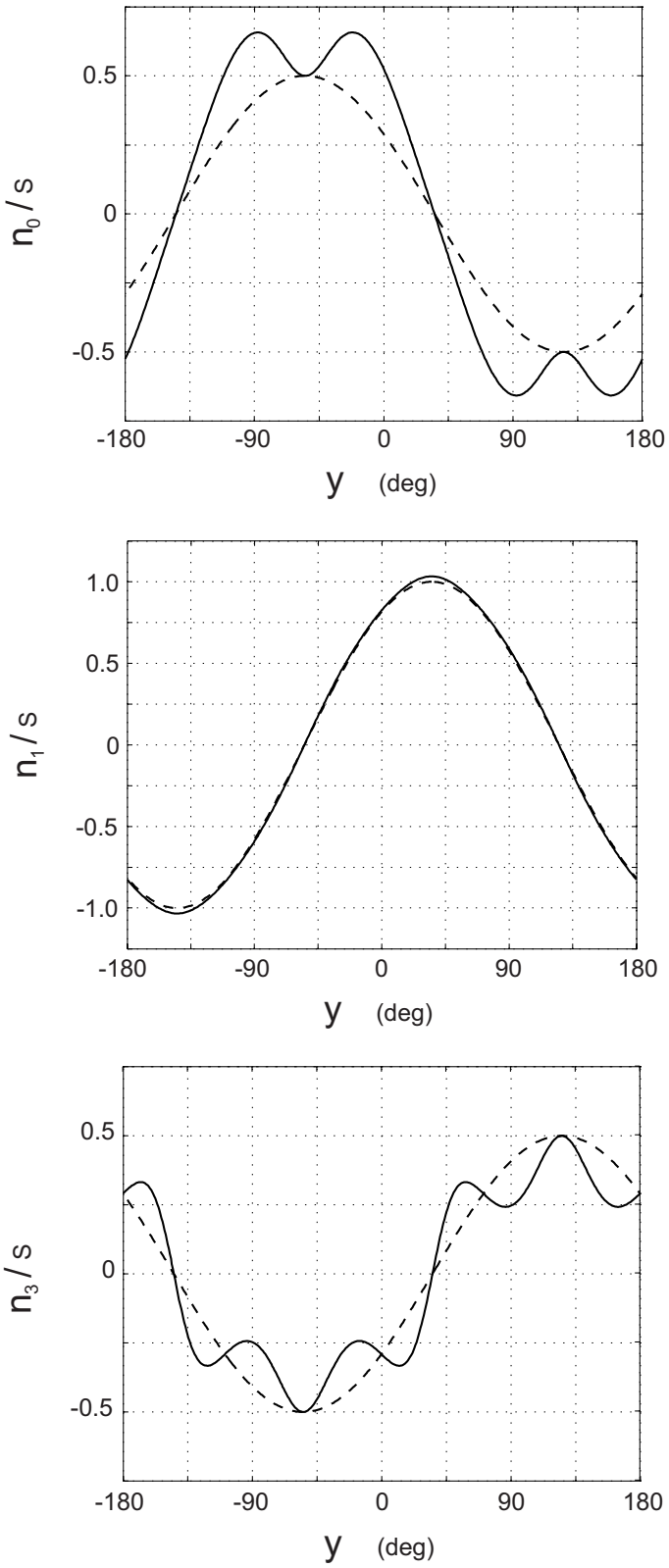

Fig. 5.2. Dependences $\nu_{0,1,3}(\psi)$ for the diagonal geometry; the dotted lines are plotted for zero elasto-optic contributions.

Figure 5.3 exhibits the angular dependence of the factor $\tilde{Q} = Q(\vec{K})|\cos\psi|$ entering Eq. (5.1) for $|E_0| = 17$ kV/cm and the light wave length $\lambda = 633$ nm. For the sake of convenience, we use the azimuth angle ψ and the polar angle θ instead of the components K_x and K_y. The polar scattering angle θ is recalculated for air. One sees that the maximum value of $\tilde{Q}(\theta, \psi)$ occurs at $\theta_{max} \approx 5^\circ$, $\psi_{max} = 0, \pi$. With increasing $|E_0|$ the value of θ_{max} decreases while the value of $\tilde{Q}_{max}$ remains almost constant. Increasing the ratio $\mu\tau/N_t$ makes the angle θ_{max} smaller but does not change $\tilde{Q}_{max}$ [26]. The latter is determined by the product $\mu\tau N_t$. The above mentioned features are important for understanding many features of light-induced scattering.

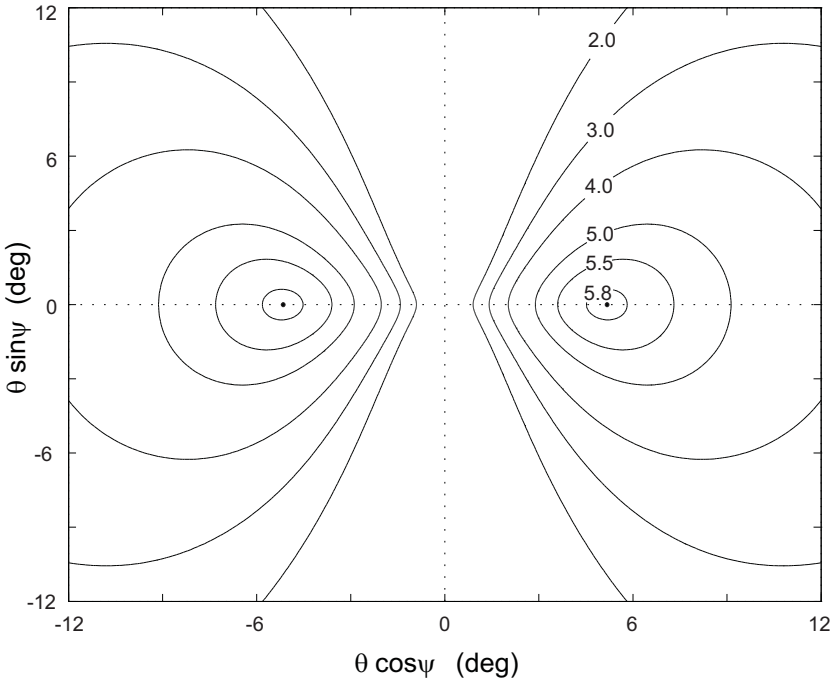

Fig. 5.3. Contour plots $\tilde{Q}(\theta, \psi) = \text{const}$ for $|E_0| = 17$ kV/cm, $\mu\tau = 10^{-7}$ cm^2/V, and $N_t = 3 \times 10^{16}$ cm^{-3}. The dots mark the positions of two symmetric maxima.

To complete the background information, we comment shortly on the status of our theory. The conventional one-species model [3] is used for the description of the photorefractive AC response. The amplitudes of the scattered waves are supposed to be small as compared to the pump wave amplitude. With respect to other relevant aspects our basic equations are quite general. They incorporate the electro- and

elasto-optic contributions to the optical permittivity and optical activity. They include fully the vectorial character of beam coupling in cubic photorefractive crystals, i.e., the possibility for light polarization change. In this sense, the vectorial theory is a generalization of the scalar theory which is applicable to birefrigent media. An application of the scalar theory to the description of light-induced scattering can be found in Ref [63].

5.3 Linear properties

The linear optical properties, determined by the 3D-vector $\boldsymbol{\kappa}$, are of importance for what follows. Within the linear approximation we have for the pump amplitude $\vec{e}$,

$$\frac{d\,\vec{e}}{dz} = i(\boldsymbol{\kappa}\cdot\hat{\boldsymbol{\sigma}})\,\vec{e} \tag{5.3}$$

The same linearized equation for $\vec{a}(z)$ follows from Eq. (5.1). To find the optical eigen-modes, we search the solution of Eq. (5.3) in the form $\vec{e} \propto \exp(i\delta k\, z)$, where δk is the wave vector measured from its non-perturbed value $k_0 = 2\pi n_0/\lambda$. Then we arrive at the 2D eigenproblem:

$$(\boldsymbol{\kappa}\cdot\hat{\boldsymbol{\sigma}})\,\vec{e} = \delta k\,\vec{e} \tag{5.4}$$

From this equation one can find two eigen-values for $(\delta k)_\pm$ and two corresponding eigen polarization vectors $\vec{e}_\pm$. Since the matrix $\boldsymbol{\kappa}\cdot\hat{\boldsymbol{\sigma}}$ is hermitian, its eigen-values are real. Using the known properties of the σ-matrices [64, 65] we have immediately, $(\delta k)_\pm = \pm\kappa$, where $\kappa = |\boldsymbol{\kappa}|$. The distance between the wave surfaces is therefore 2κ. For the diagonal configuration we have $2\kappa = \sqrt{3s^2E_0^2 + 4\rho^2}$.

The eigen polarizations that correspond to the eigen-values $\pm\kappa$ are generally elliptical; one of the ellipses is extended along $[\bar{1}\bar{1}1]$ (parallel to $\vec{E}_0$) and another – along $[112]$ (perpendicular to $\vec{E}_0$). The degree of ellipticity (i.e. the ratio short axis/long axis) in both cases is the same, $|\rho|/(\kappa + \sqrt{3}|sE_0|/2)$. In the limit $|E_0| \gg E_c \equiv 2|\rho|/\sqrt{3}|s|$ the eigen-modes are polarized linearly, in the laboratory coordinate system the corresponding polarization vectors are $\vec{e}_+ = (1,0)$ and $\vec{e}_- = (0,1)$, in the experiments they are usually horizontal and vertical, respectively. This case is of practical interest for BTO crystals at $\lambda \simeq 630$ nm. The rotatory power is fairly small here, $|\rho| \simeq 6.5$ deg/mm, so that the characteristic field $E_c \simeq 3.2$ kV/cm. The values of the ac-fields used in experiment are typically much higher. In other words, the applied field suppresses strongly optical activity, which can actually be neglected [66].

The vectorial equation (5.1) admits the general solution,[16]

$$\begin{aligned}\vec{e}\,(z) &= \exp[i(\boldsymbol{\kappa}\cdot\hat{\boldsymbol{\sigma}})z]\,\vec{e}_0 \\ &= [\cos\kappa z + i\kappa^{-1}(\boldsymbol{\kappa}\cdot\hat{\boldsymbol{\sigma}})\,\sin\kappa z]\,\vec{e}_0\end{aligned} \tag{5.5}$$

where $\vec{e}_0 = \vec{e}\,(0)$ is the input pump polarization vector. If it is chosen to be an eigenvector, $\vec{e}_0 = \vec{e}_\pm$, no polarization changes occur during propagation. This means, in particular, that the vertical and horizontal input polarization are not subjected to any strong changes owing to the linear effects for $|E_0| \gg 3.2$ kV/cm.

5.4 Calculation of scattering characteristics

As we have seen, the vectorial pump amplitude $\vec{e}$ entering Eq. (5.1) is not constant in the general case, it changes because of the linear optical effects. The same is partly applicable to the probe amplitude $\vec{a}$. The linear effects do not influence directly the beam intensities. They change, however, the polarization state and affect in this way the polarization-sensitive nonlinear coupling.

Within the vectorial theory, we can get rid of the linear terms by switching from the vector $\vec{a}$ to the new vectorial amplitude $\vec{b}$,

$$\vec{a} = \exp[i(\boldsymbol{\kappa}\cdot\hat{\boldsymbol{\sigma}})z]\,\vec{b} \tag{5.6}$$

This procedure is similar to the above transition from $\vec{e}\,(z)$ to $\vec{e}_0$, see Eq. (5.5). As the matrix $\boldsymbol{\kappa}\cdot\hat{\boldsymbol{\sigma}}$ is hermitian, the transformation (5.6) is unitary; it changes neither the values of the 2D-vectors nor their scalar products. It is equivalent to the so-called interaction representation in quantum mechanics [64].

After the unitary transformation we have instead of Eq. (5.1):

$$\frac{d\vec{b}}{dz} = (\vec{b}\cdot\vec{e}_0^{\,*})\,(q_0 + \mathbf{q}\cdot\hat{\boldsymbol{\sigma}})\,\vec{e}_0 \tag{5.7}$$

where $q_0 = Q|E_0\cos\psi|\nu_0$ is a real constant and $\mathbf{q}$ is a real 3D-vector,

$$\begin{aligned}\mathbf{q} = Q|E_0\cos\psi|\,\Big[&\frac{\boldsymbol{\kappa}(\boldsymbol{\nu}\cdot\boldsymbol{\kappa})}{\kappa^2} \\ &+ \Big[\boldsymbol{\nu} - \frac{\boldsymbol{\kappa}(\boldsymbol{\nu}\cdot\boldsymbol{\kappa})}{\kappa^2}\Big]\,\cos 2\kappa z - \frac{(\boldsymbol{\nu}\times\boldsymbol{\kappa})}{\kappa}\,\sin 2\kappa z\Big]\end{aligned} \tag{5.8}$$

This vector depends on the propagation coordinate z, wherein the oscillating terms (presented in the second line) are due to the fact that $\boldsymbol{\kappa}$ and $\boldsymbol{\nu}$ are not parallel to

each other, i.e., the eigen-vectors of the operators $\boldsymbol{\kappa} \cdot \hat{\boldsymbol{\sigma}}$ and $\boldsymbol{\nu} \cdot \hat{\boldsymbol{\sigma}}$ are different. The spatial frequency of the oscillations is 2κ.

The problem of calculation of scattering characteristics is reduced now to two different tasks: (i) *Calculation of intensity distributions for different pump polarizations* and (ii) *Calculation of polarization properties of scattered light*. To solve the first task, it is sufficient to find $\vec{b}(z, \theta, \psi)$. Then the value $|\vec{b}(z_0)|^2 \equiv |\vec{a}(z_0)|^2$, where z_0 is the crystal thickness, defines the angular distribution of the light-induced scattering. The second task is more difficult. Direction of the vector $\vec{b}(z)$ is more sensitive to the model assumptions than its absolute value. Furthermore, it is necessary to perform the unitary transformation (5.6) from $\vec{b}(z_0)$ to $\vec{a}(z_0)$ to find the output polarization.

5.4.1 Intensity distributions

The spatially-oscillating terms in Eq. (5.8) are of minor importance in the case of strong spatial amplification. The point is that the presence of the spatially-uniform contribution to $\mathbf{q}$ and the spatially-uniform parameter q_0 gives rise to an exponential growth of $\vec{b}$ with increasing propagation distance z, whereas the oscillating contributions to $\mathbf{q}$ cannot produce any permanent spatial growth. Furthermore, the amplitudes of the oscillating terms in Eq. (5.8) are often relatively small for the actual angles θ and ψ. For these reasons, we neglect these terms in the leading approximation. Then we have from Eq. (5.7):

$$\vec{b} \approx \tilde{Q}|E_0|\,(\vec{e}_0^{\,*} \cdot \vec{b}_0)\,\frac{\exp(\Gamma z)}{\Gamma}\left[\nu_0 + \frac{(\boldsymbol{\nu} \cdot \boldsymbol{\kappa})(\boldsymbol{\kappa} \cdot \hat{\boldsymbol{\sigma}})}{\kappa^2}\right]\vec{e}_0 \tag{5.9}$$

where $\vec{b}_0 = \vec{b}(0)$ is the seed amplitude and Γ is the rate of spatial amplification called also *the increment*. The general expression for Γ can be presented as follows:

$$\Gamma = Q|E_0 \cos\psi|\left[\nu_0 + \kappa^{-2}\,(\boldsymbol{\nu} \cdot \boldsymbol{\kappa})\,(\boldsymbol{\kappa} \cdot \boldsymbol{S}_0)\right] \tag{5.10}$$

where $\boldsymbol{S}_0 = \vec{e}_0^{\,*} : \hat{\boldsymbol{\sigma}} : \vec{e}_0 \equiv \langle \vec{e}_0 | \hat{\boldsymbol{\sigma}} | \vec{e}_0 \rangle$ is the real 3D-vector characterizing the pump state and often called the Stokes vector [42]. The descriptions of the pump polarization by $\boldsymbol{S}_0$ and $\vec{e}_0$ are equivalent; they differ only in the degree of convenience. The absolute value of the Stokes vector $\boldsymbol{S}_0$ for a totally polarized pump wave equals to unity.

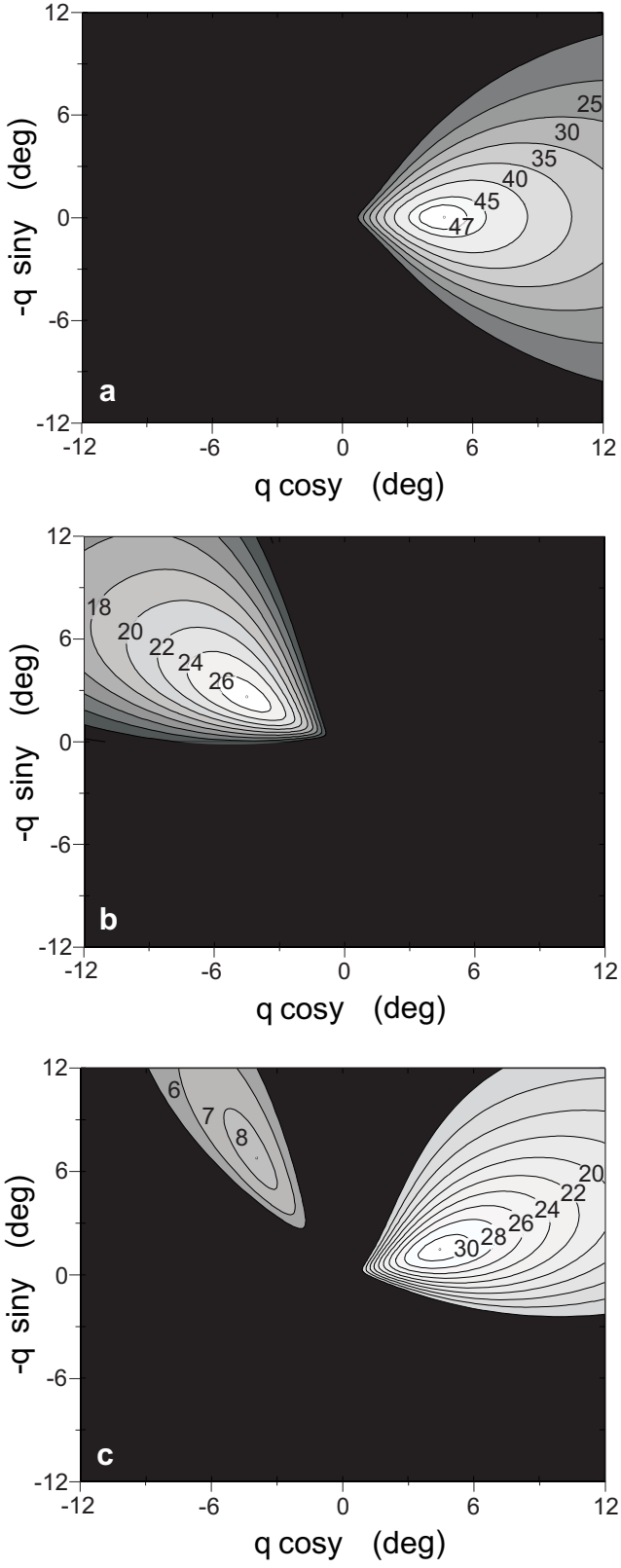

Fig. 5.4. Angular dependences of the increment for $|E_0| = 17$ kV/cm and the accepted parameters of BTO crystals. The cases (a), (b), and (c) correspond to horizontal, vertical, and circular pump polarization, respectively. The polar angle θ is recalculated for air.

The dependence of the increment on the polar scattering angle θ is defined by the factor $\tilde{Q}$, see Fig. 5.3. The dependence of Γ on the azimuth angle ψ comes from the factor Q and also from the parameters ν_0 and $\boldsymbol{\nu}$, see Fig. 5.2. Owing to the general properties of the last parameters, we have $\Gamma(\psi) = -\Gamma(\psi \pm \pi)$; in other words, the increment is an odd function of the scattering (grating) vector $\vec{K}$. This feature is indeed a generalization of the known property of the scalar spatial amplification, caused by a non-local photorefractive response, to the vectorial case [3]. The increment Γ does not depend on the polarization of the test beam. This polarization influences only the pre-exponent $(\vec{e}_0^{\,*} \cdot \vec{b}_0)$; most probably, $\vec{e}_0 \parallel \vec{b}_0$ so that $|\vec{e}_0^{\,*} \cdot \vec{b}_0| = |\vec{b}_0|$.

Let us consider several representative cases of the pump polarization. For the horizontal and vertical polarizations we have $\boldsymbol{\kappa} \cdot \boldsymbol{S}_0 = \pm\kappa$, respectively, so that the square bracket in Eq. (5.10) is simply $[\nu_0 \pm (\boldsymbol{\nu} \cdot \boldsymbol{\kappa})\kappa^{-1}]$. Figures 5.4(a) and 5.4(b) show the corresponding angular dependences of the increment [in the region of its positive values] for $|E_0| = 17$ kV/cm and the accepted BTO parameters. For the horizontal $(+)$ polarization, the dependence $\Gamma = \Gamma_+(\theta, \psi)$ is characterized by a pronounced horizontal right lobe. The maximum rate of spatial amplification ($\Gamma_+^{max} \approx 48$ cm^{-1}) takes place at $\psi = 0$, $\theta \simeq 5°$. Light-induced scattering is strongest in this case [16]. For vertical $(-)$ polarization the distribution $\Gamma_-(\theta, \psi)$ is quite different; it possesses one tilted left lobe at $\psi \approx 150°$. The maximum value of the increment is noticeably smaller here, $\Gamma_-^{max} \approx 27$ cm^{-1}.

Next we calculate the gain factor $\tilde{\Gamma} = (2z_0)^{-1} \ln(|\vec{a}(z_0)|^2/|\vec{a}(0)|^2)$ by solving numerically the initial vectorial Eq. (5.1) for the thickness $z_0 = 1$ cm and the same material and experimental parameters. We find that the angular distributions of the increment Γ and the gain $\tilde{\Gamma}$ differ from each other only in fine details. This proves that (i) the oscillating terms in $\mathbf{q}$ are of minor importance and (ii) the increment Γ is really a useful characteristic of the intensity distribution for light-induced scattering.

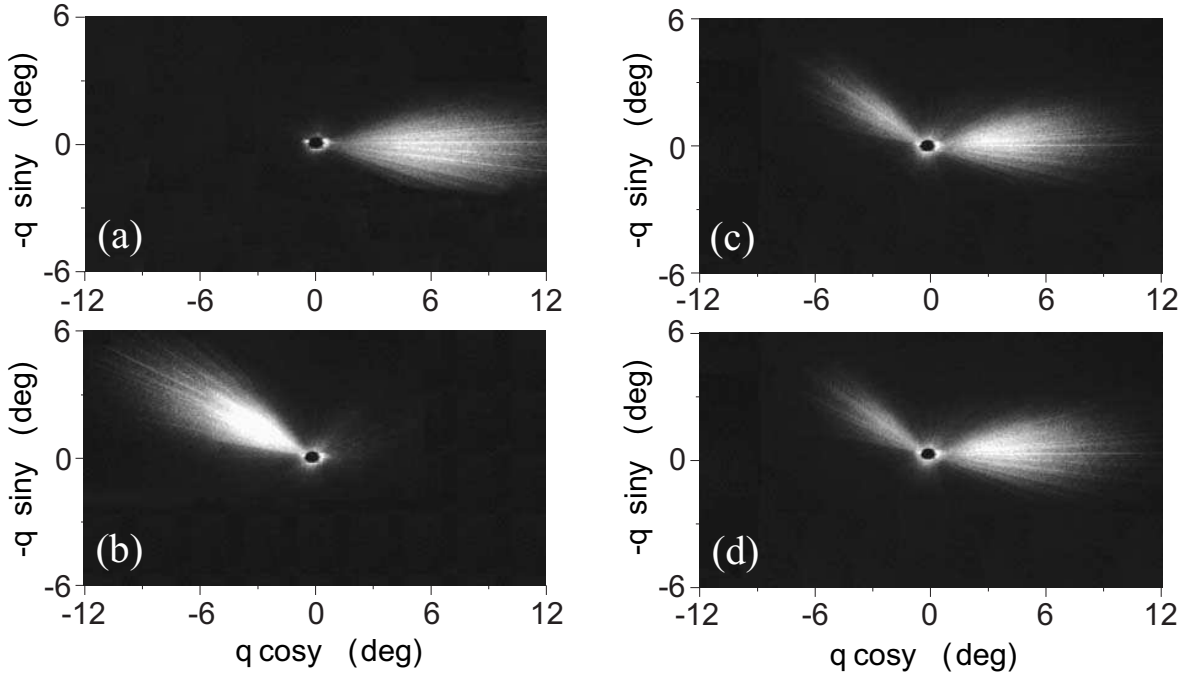

Fig. 5.5. Experimental distributions [7] of scattered light for $|E_0| = 17$ kV/cm for the diagonal geometry. The cases (a), (b), (c), and (d) correspond to horizontal, vertical, +45°, and (+)–circular pump polarization, respectively. The scattering distributions for −45° and (−)–circular polarization are not visually different from those shown for the cases (c) and (d).

Now we compare our results with an experiment made by the group of Kamshilin [7]. In this experiment a 9.94 mm-thick sample was used, the amplitude of the ac-field (applied along the diagonal $[\bar{1}\bar{1}1]$)) was $\approx 17kV/cm$, the typical pump intensity was $\approx 0.8W/cm^2$, and the AC frequency was $\approx 70Hz$. Figures 5.5(a) and 5.5(b) show intensity distributions for light-induced scattering, recorded from an observation screen placed in far-field, for $\vec{e}_0 \parallel [\bar{1}\bar{1}1]$ and $\vec{e}_0 \perp [\bar{1}\bar{1}1]$. One sees that the experiment gives very similar angular distribution of scattered light. The azimuth positions of the lobes and the polar angle θ_{max} are in good agreement with theory.

To analyze the effect of pump polarization on the scattering characteristics in more detail, we have considered the cases of right and left circular pump polarization and also two cases of linear polarization when the polarization angle $\varphi_0 = \angle\, \vec{e}_0\,, [\bar{1}\bar{1}1] = \pm 45°$. The main theoretical prediction is that the increment Γ is almost the same for these four cases,

$$\Gamma \simeq (\Gamma_+ + \Gamma_-)/2 = Q|E_0 \cos\psi|\,\nu_0 \tag{5.11}$$

To prove this assertion, we mention that for all four cases the pump polarization

vector can be represented as $\vec{e}_0 = c_+\vec{e}_+ + c_-\vec{e}_-$ with $|c_\pm| \simeq 1/\sqrt{2}$. This is true because the eigen-vectors $\vec{e}_\pm$ are parallel and perpendicular to the $[\bar{1}\bar{1}1]$-axis for $|E_0| \gg 3.2$ kV/cm. Therefore we have $(\boldsymbol{\kappa}\cdot\hat{\boldsymbol{\sigma}})\,\vec{e}_0 = \kappa(c_+\,\vec{e}_+ - c_-\,\vec{e}_-)$ which is perpendicular to $\vec{e}_0$, and from Eq. (5.10) we get immediately the necessary result. Note that the suppression of optical activity by the applied field is crucial for validity of Eq. (5.11).

Figure 5.4(c) shows the angular distribution $\Gamma(\theta,\psi)$ given by Eq. (5.11) for $|E_0| =$ 17 kV/cm. It is the sum of the distributions presented in the Figs. 5.4(a) and 5.4(b). Here we have two scattering lobes. The strongest one is tilted by $\approx 15^\circ$ to the horizontal. It originates indeed from the horizontal lobe of the increment $\Gamma_+(\theta,\psi)$, the tilt being caused by the influence of the "negative" lobe of $\Gamma_-(\theta,\psi)$ which can be obtained by a π-rotation of the positive lobe shown in Fig. 5.4(b). The weakest lobe in Fig. 5.4(c) originates from the tilted lobe presented in Fig. 5.4(b); its increasing tilt to the horizontal is caused by the influence of the negative horizontal lobe of $\Gamma_+(\theta,\psi)$ [situated symmetrically to the lobe shown in Fig. 5.4(a)]. The maximum values of Γ for the quasi-horizontal and tilted left lobes in Fig. 5.4(c) are $\simeq 30$ cm^{-1} and $\simeq 8$ cm^{-1}, respectively; they are considerably smaller than the corresponding values for Figs. 5.4(a) and 5.4(b). This is, indeed, due to the described partial compensation mechanism.

Direct simulation of the vectorial equations (5.6), (5.7) has shown that the spatial distributions of $\tilde{\Gamma} = (2z_0)^{-1}\ln(|\vec{a}(z_0)|^2/|\vec{a}(0)|^2)$ for the $(\pm)$-circular and $\pm 45^\circ$ pump polarization are in a good qualitative agreement with the distribution presented in Fig. 5.4(c). At the same time, quantitative distinctions become here noticeable.

Figures 5.6(a) and 5.6(b) show the angular dependence of the gain factor $\tilde{\Gamma}$ for right and left circular polarizations. These distributions are slightly different, which is fully due to the influence of optical activity. A bigger influence of optical activity (as compared to the cases of eigen pump polarization) is caused by a partial cancellation of the biggest contributions to Γ coming from Γ_+ and Γ_-.

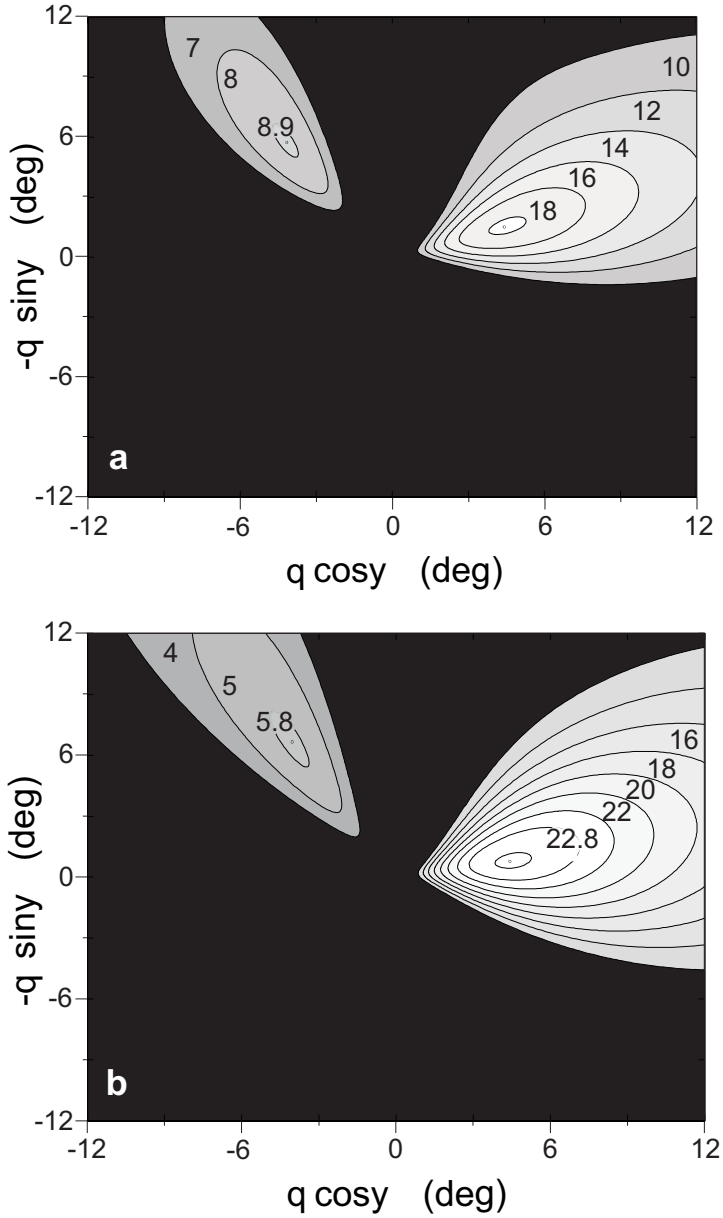

Fig. 5.6. Dependence $\tilde{\Gamma}(\theta, \psi)$ for (+) (a) and (−) (b) circular pump polarization. The maximum values for the main lobe are $\simeq 18.2$ and 22.9 cm^{-1}, whereas for the secondary lobe they are $\simeq 9.0$ and $\simeq 5.9$ cm^{-1}.

The experiment [7] did not show any noticeable difference between the intensity distributions for the above four different choices of pump polarization [7]. Figure 5.5(c) shows a representative distribution obtained for the left circular polarization at $|E_0| = 17$ kV/cm. In accordance with theory, there is a slightly tilted main right lobe and a considerably weaker, strongly tilted left lobe. The angular positions of

these lobes are $\psi \approx 5^\circ$ and $\approx 135^\circ$, respectively. These numbers are slightly different from the model predictions. The intensity of the scattered wave is, as expected, considerably lower than that for the cases (a) and (b). It should be understood that the pump is essentially depleted in the 9.94 mm-sample, i.e., the spatial growth experiences a saturation. This makes unreliable quantitative estimates of the total scattering intensity but can hardly affect strongly the angular and polarization scattering properties.

5.4.2 Scattering polarization

Polarization properties of scattered light seem to be more sensitive to the choice of experimental and material parameters than the intensity distributions. This is especially true with respect to the weakest lobes considered above.

Since the simplified model which ignores the spatially-oscillating contributions to $\vec{q}$ but includes elasto-optic contributions to Γ gives satisfactory results for the intensity distributions, it is natural to apply it to the description of the output polarizations. Therefore we have to calculate $\vec{b}(z_0)$ from Eq. (5.9) and perform the unitary transformation (5.6) to find $\vec{a}(z_0)$ as a function of θ and ψ. The most important propagation directions correspond indeed to the maxima of the increment Γ.

Let us revisit first the cases of horizontal and vertical input pump polarization. Here $\vec{e}_0$ is the eigen-vector of the operator $\boldsymbol{\kappa} \cdot \hat{\boldsymbol{\sigma}}$ with a good accuracy (we assume again that $|E_0| \gg E_c \simeq 3.2$ kV/cm). Therefore $\vec{b}(z_0)$ is almost parallel to $\vec{e}_0$. The unitary transformation does not change the eigen-vector directions. We come therefore to the conclusion that for the main horizontal lobe presented in Fig. 5.4(a) the scattering polarization has to be horizontal and for the tilted left lobe of Fig. 5.4(b) – vertical. Experimental polarization measurements confirm this prediction with a high accuracy.

In the case of mixed pump polarization it is useful to represent the amplitude $\vec{b}$ in the form $\vec{b} = b_+(z)\,\vec{e}_+ + b_-(z)\,\vec{e}_-$. Then for all the four cases considered above the ratio horizontal-to-vertical intensity components is the same,

$$|b_+/b_-|^2 = (\Gamma_+/\Gamma_-)^2 \tag{5.12}$$

This ratio depends on the azimuth angle ψ and does not depend on the polar angle θ. Let us estimate it first for the main scattering lobe of Fig. 5.4(c). At the maximum of $\Gamma(\theta, \psi)$ we have $|b_+/b_-|^2 \approx 10^2$. This means that the vector $\vec{b}(z_0)$ at this maximum

is almost horizontal, as well as the vector $\vec{a}(z_0)$. Simulation of the vectorial equation (8) with the oscillating terms and optical activity included followed by the unitary transformation (5.6) from $\vec{b}(z_0)$ to $\vec{a}(z_0)$ has given the range $(3-23)\times 10^2$ for the ratio of horizontally-to-vertically polarized intensity components for the above cases of mixed pump polarization. In this way, we expect from theory that the polarization of the quasi-horizontal (strongest) lobe is almost horizontal ($\vec{a}(z_0) \parallel [\bar{1}\bar{1}1]$) for the ($\pm$)-circular and $\pm 45°$-pump polarization. Experimental measurements confirm this result with a high accuracy.

We turn lastly to the weakest lobe of Fig. 5.4(c). Here the simplified model (neglected oscillating terms and optical activity) gives the estimate $|b_-/b_+|^2 \approx 3$ for the corresponding maximum of the increment. This number cannot be considered as big enough to expect a quasi-vertical polarization of the scattering lobe. More accurate numerical calculations based on Eqs. (5.6) – (5.8) have shown that the intensity ratio of vertical/horizontal components ranges from ≈ 1.6 to ≈ 12.5 for the cases of mixed pump polarization. This theoretical prediction has found only a qualitative experimental confirmation. Experiment shows that the polarization of the weakest (tilted) lobe is vertical with a good accuracy for ($\pm$)-circular and $\pm 45°$-pump polarization.

5.5 Resume

We have applied above the vectorial theory to describe the angular distributions and polarization properties of light-induced scattering in cubic ac-biased BTO crystals for different polarization states of the incident pump beam. The diagonal geometry, distinguished by the strongest vectorial coupling, was chosen for comparison between theory and experiment.

We have found that a great variety of the angular intensity distributions can be described uniformly within a relatively simple and transparent vectorial model of spatial amplification without an extensive use of numerical simulations. The measured scattering distributions are in good quantitative agreement with theory. The photo-elastic contributions to the coupling constants affect mostly the absolute values of the rates of spatial amplification.

For the strongest lobes of light-induced scattering, the theory allows also for a simple and satisfactory description of the main polarization properties. The polarization properties of the weakest scattering lobe are found to be sensitive to the model assumption made. At this point, there is only qualitative agreement between

experiment and theory (including numerical simulations).

The results obtained are of interest for the use of fast photorefractive materials for various interferometric applications,[15, 22, 23, 67] and also for characterization purposes [68, 69].

Chapter 6

Summary and outlook

6.1 Summary

The aim of this thesis was the extension of our knowledge about the vectorial beam coupling in sillinite crystals and the study of the possibilities of using vectorial effects in different important applications. In this section we collect the main significant findings of our work.

6.1.1 Space-charge field formation

- The space-charge field profile within one grating period strongly depends on the light contrast m. It has a sine-like form only for small contrast, $m \lesssim 0.05$. With increasing m, a discontinuity, situated at the intensity maximum, appears and the space-charge field profile tends to the square-wave form.
- All Fourier harmonics of the space-charge field are imaginary. It means, in particular, that the fundamental component is $\pi/2$-shifted with respect to the intensity distribution for any value of the contrast, i.e. the PR ac-response is always nonlocal.
- The quality factor of the space-charge waves, Q, determines the photorefractive nonlinear response in the whole contrast range. The dependencies of the space-charge field harmonics amplitudes on Q are saturated for $Q \gg 1$.
- The whole contrast range can roughly be divided into two regions. The region $0 < m \lesssim 0.05$ corresponds to the linear theory. Here the fundamental

amplitude E_K grows rapidly with the contrast and the rate of spatial amplification of weak signals is extremely high, up to 10^2 cm^{-1}. In the second region, $0.05 \lesssim m \leqslant 1$, the growth of $E_K(m)$ is strongly saturated. This region is more appropriate for grating recording.

6.1.2 Vectorial beam coupling theory

- It was proved that the light fringes remain straight inside the crystal in spite of coupling effects.
- The exact solution for the set of vectorial beam coupling equations was obtained. This solution is valid for arbitrary intensities and polarizations of the input light beams.
- New conservation laws involving polarization degrees of freedom were found.
- The obtained exact solution was applied to particular optical configurations and a number of new regimes, where the input beams parameters influence strongly the output energy and polarization characteristics, were predicted.

6.1.3 Grating translation technique

- Based on the improved vectorial coupling theory, the problem of transformation of the fast phase modulation of one of the input beams into output intensity modulation was solved.
- It was shown that the input beams polarizations affect essentially the output intensities modulation. Using input beams with linear or identical polarizations leads to the intensity modulation dependent on input phase φ as $\cos\varphi$. With other input beam polarizations, the output intensities have two terms, which are proportional to $\cos\varphi$ and $\sin\varphi$, respectively.

6.1.4 Linear signal detection

- The possibility of linear detection without polarization filtering by making use of elliptically polarized input light beams was shown.
- The theory of the linear detection with polarization filtering for the case of thick crystals was developed. The optimal experimental parameters, which maximize the output intensity modulation are found.

- It was predicted that the maximal value of the output intensity modulation is twice larger than was reported earlier. This maximum can be achieved with or without polarization filtering.

6.1.5 Polarization properties of the scattered light

- A big variety of the observed angular intensity distributions was explained uniformly within a relatively simple and transparent vectorial model of spatial amplification without an extensive use of numerical simulations.

- The scattered patterns consisting of two lobes are predicted for both, linear and circular polarizations of pump beam. For the strongest lobe, the theory allows a simple and satisfactory description of the main polarization properties. The polarization properties of the weakest scattering lobe are found to be sensitive to the model assumption made.

6.2 Outlook

Despite of numerous publications, vectorial beam coupling covers still many interesting and challenging problems. Some of them, which are related to this study and look promising for the use in different photorefractive applications, are formulated below.

6.2.1 Vectorial beam coupling

- The vectorial coupling theory can be extended to the case of the reflection geometry. The equation describing the dependence of the space-charge field amplitude on the light contrast does not depend on the geometry in question. Thus, only the vectorial Bragg diffraction equations need to be rewritten for a reflection configuration.

- It is interesting to investigate the influence of the vectorial effects on the feedback controlled space-charge field formation [70]. Until now feedback theories have been developed only for scalar beam interactions [71, 72, 73, 74, 75, 76].

- The phase conjugation problem was also considered in its scalar variant [11]. In the vectorial case, one can expect the appearance of new valuable polarization features.

6.2.2 Linear signal detection

- Within the performed simple optimization procedures the maximum of the modulation coefficient reaches only 72% of the theoretical predicted limiting value. Therefore, looking for new optimization schemes should allow further improving of the linear detection characteristics.

- It is attractive to consider the problem of linear signal detection in the reflection geometry.

Bibliography

[1] M. P. Petrov, S. I. Stepanov, and A. V. Khomenko, *Photorefractive Crystals in Coherent Systems*, *Springer-Verlag, Berlin*, 1991.

[2] P. Günter, *Nonlinear Optical Effects and Materials*, *Springer-Verlag, Berlin*, 2000.

[3] L. Solymar, D. J. Webb, and A. Grunnet-Jepsen, *The Physics and Applications of Photorefractive Materials*, *Claredon Press, Oxford*, 1996.

[4] P. Refregier, L. Solymar, H. Rajbenbach, and J. -P. Huignard, "Two-beam coupling in photorefractive $Bi_{12}SiO_{20}$ crystals with moving grating: theory and experiments", J. Appl. Phys. **58**, 45-57, 1985.

[5] S. I. Stepanov and M. P. Petrov, "Efficient unstationary holographic recording in photorefractive crystals under an external alternating electric field", Opt. Commun, **53**, 292-295, 1985.

[6] C. S. K. Walsh, A. K. Powel, and T. J. Hall, "Techniques for the enhancement of space-charge fields in photorefractive materials", J. Opt. Soc. Am. **B 7**, 288-303, 1990.

[7] E. Raita, A. A. Kamshilin, and T. Jaaskelainen, *Polarization properties of fanning light in fiberlike bismuth titanium oxide crystals*, *Opt. Lett.* **21**, 1897-1899, 1996.

[8] A. A. Kamshilin, V. V. Prokofiev, and T. Jaaskelainen, *Beam fanning and double phase conjugation in a fiber-like photorefractive sample*, *IEEE J. Quant. Electron.* **31**, 1642-1647, 1995.

[9] A. A. Kamshilin, T. Jaaskelainen, C. J. Lima, M. R. B. Andreeta, and V. V. Prokofiev, *2-Wave Mixing In Photorefractive Bi12SiO20 Fibers*, *Opt. Lett.* **18**, 690-692, 1993.

[10] A. A. Kamshilin, R. Ravattinen, H. Tuovinen, T. Jaaskelainen, and V. Prokofiev, *Double-Phase Conjugation In Bi12Tio20 Photorefractive Fiber-Like Crystal*, *Opt. Commun.* **103**, 221-226, 1993.

[11] E. Raita, A. A. Kamshilin, V. V. Prokofiev, and T. Jaaskelainen, *Fast mutually pumped phase conjugation using transient photorefractive coupling*, *Appl. Phys. Lett.* **70**, 1641-1643, 1997.

[12] A. A. Kamshilin, E. Raita, and A. V. Khomenko, *Intensity redistribution in a thin photorefractive crystal caused by strong fanning effect and internal reflections J. Opt. Soc. Am.* **B 13**, 2536-2543, 1996.

[13] A. A. Kamshilin, E. Raita, and T. Jaaskelainen, *Photorefractive Surface Waves in a Thin Bi12TiO20 Crystal*, *Optical Review*, **3**, 443-446, 1996.

[14] E. Shamonina, K. H. Ringhofer, B. I. Sturman, G. Cedilnik, A. Kießling, R. Kowarschik, A. A. Kamshilin, V. V. Prokofiev, and T. Jaaskelainen, *Opt. Lett.*, **23**, 1435-1438, 1998.

[15] A. A. Kamshilin, Y. Iida, S. Ashihara, T. Shimura, and K. Kuroda, *Linear sensing of speckle-pattern displacements using a photorefractive GaP crystal*, *Appl. Phys. Lett.* **74**, 2575-2577, 1999.

[16] B. I. Sturman, E. V. Podivilov, K. H. Ringhofer, E. Shamonina, V. P. Kamenov, E. Nippolainen, V. V. Prokofiev, and A. A. Kamshilin, *Theory of photorefractive vectorial wave coupling in cubic crystals*, *Phys. Rev.* **E 60**, 3332-3352, 1999.

[17] B. I. Sturman, A. I. Chernykh, V. P. Kamenov, E. Shamonina, and K. H. Ringhofer, *Resonant vectorial wave coupling in cubic photorefractive crystals*, *J. Opt. Soc. Am.* **B 17**, 985-996, 2000.

[18] B. I. Sturman, D. J. Webb, R. Kowarschik, E. Shamonina, and K. H. Ringhofer, *Exact solution of the Bragg-diffraction problem in sillenites*, *J. Opt. Soc. Am.* **B 11**, 1813-1819, 1994.

[19] G. A. Brost, *Photorefractive grating formations at large modulations with alternating electric fields*, *J. Opt. Soc. Am.* **B 9**, 1454-1460, 1992.

[20] J. E. Millerd, E. M. Garmine, M. B. Klein, B. A. Wechsler, F. P. Strohkendl, and G. A. Brost, *Photorefractive response at high modulation depths in Bi12TiO20*, *J. Opt. Soc. Am.* **B 9**, 1449-1453, 1992.

[21] C. A. Fuentes-Hernndez and A. V. Khomenko, *Beam Collapse and Polarization Self-Modulation in an Optically Active Photorefractive Crystal in an Alternating Electric Field*, *Phys. Rev. Lett.* **83**, 1143, 1999.

[22] Ph. Delaye, L. A. de Montmorillon, and G. Roosen, *Transmission Of Time Modulated Optical Signals Through An Absorbing Photorefractive Crystal*, *Opt. Commun.* **118**, 154, 1995.

[23] A. A. Kamshilin, K. Paivasaari, M. Klein, and B. Pouet, "Adaptive interferometer using self-induced electro-optic modulation", Appl. Phys. Lett. **77**, 4098-4100 (2000).

[24] K. Paivasaari, A. Kamshilin, V. V. Prokofiev, B. Sturman, G. F. Calvo, M. Carrascosa, and F. Agullo-Lopez, *Linear phase demodulation in photorefractive crystals with nonlocal response*, *J. Appl. Phys.* **90**, 3135-3141, 2001.

[25] G. F. Calvo, B. Sturman, M. Carrascosa, F. Agullo-Lopez, K. Paivasaari, and A. Kamshilin, *Grating translation technique for vectorial beam coupling and its applications to linear signal detection*, *J. Opt. Soc. Am.* **B 19**,1564-1574, 2002.

[26] B. I. Sturman, M. Mann, J. Otten, and K. H. Ringhofer, *Space-charge waves in photorefractive crystals and their parametric excitation*, *J. Opt. Soc. Am.* **B 10**, 1919-1932, 1993.

[27] G. F. Calvo, B. I. Sturman, F. Agull-Lpez, and M. Carrascosa, *Singular behavior of light-induced space charge in photorefractive media under an ac field*, *Phys. Rev. Lett.* **84**, 3839, 2000.

[28] G. Fernandez, B. Sturman, F. Agullo-Lopez, and M. Carrascosa, *Solitonlike beam propagation along light-induced singularity of space charge in fast photorefractive media*, *Phys. Rev. Lett.* **89**, 2002.

[29] A. Marrakchi, R. V. Johnson, and A. R. Tanguay, *Polarization Properties Of Photorefractive Diffraction In Electrooptic And Optically-Active Sillenite Crystals (Bragg Regime)*, *J. Opt. Soc. Am.* **B 3**, 321-336, 1986.

[30] H. Touvinen, A. A. Kamshilin, and J. Jaaskelainen, *Asymmetry of two-wave coupling in cubic photorefractive crystals* , *J. Opt. Soc. Am.* **B 14**, 3383, 1997.

[31] V. P. Kamenov, E. Shamonina, K. H. Ringhofer, E. Nippolainen, V. V. Prokofiev, and A. A. Kamshilin, *Two-wave mixing in (*111*)-cut Bi12SiO20 and Bi12TiO20 crystals: Characterization and comparison with the general orientation*, *Phys. Rev.* **E 62**, 2863-2870 (2000).

[32] T. E. McClelland, D. J. Webb, B. I. Sturman, and K. H. Ringhofer, *Generation Of Spatial Subharmonic Gratings In The Absence Of Photorefractive Beam Coupling*, *Phys. Rev. Lett.* **73**, 3082, 1994.

[33] H. C. Pedersen, D. J. Webb, and P. M. Johansen, *Influence of beam-coupling on photorefractive parametric oscillation in a dc-field-biased Bi12SiO20 crystal*, *J. Opt. Soc. Am.* **B 15**, 2439, 1998.

[34] T. E. McClelland, D. J. Webb, B. I. Sturman, M. Mann, and K. H. Ringhofer, *Low-Frequency Peculiarities Of The Photorefractive Response In Sillenites*, *Opt. Commun.* **113**, 371, 1995.

[35] T. E. McClelland, D. J. Webb, B. I. Sturman, E. Shamonina, M. Mann, and K. H. Ringhofer, *Excitation of higher spatial harmonics by a moving light pattern in sillenites*, *Opt. Commun.* **131**, 315, 1996.

[36] J. R. Goff,*Polarization properties of transmission and diffraction in BSO - a unified analysis*, *J. Opt. Soc. Am.* **B 12**, 99-116, 1995.

[37] S. Mallick and D. Rouède, *Influence Of The Polarization Direction On 2-Beam Coupling In Photorefractive Bi12Sio20 - Diffusion Regime*, *Appl. Phys.* **B 43**, 239-245, 1987.

[38] E. Shamonina, V. P. Kamenov, K. H. Ringhofer, G. Cedilnik, A.Kießling, and R.Kowarschik, *Optimum orientation of volume phase gratings in sillenite crystals: is it always 111 ?*, *J. Opt. Soc. Am.* **B 15**, 2552-2559, 1998.

[39] H. C. Pedersen and P. M. Johansen, *Analysis of wave coupling in photorefractive cubic media far from paraxial limit*, *J. Opt. Soc. Am.* **B 12**, 592-599, 1996.

[40] H. Tuovinen, A. A. Kamshilin, and J. Jaaskelainen, *Asymmetry of two-wave coupling in cubic photorefractive crystals* , *J. Opt. Soc. Am.* **B 14**, 3383-3392, 1997.

[41] L. D. Landau and E. M. Lifshiz, *Field Theory*, *Pergamon Press*, Oxford, 1969.

[42] M. Born and E. Wolf, *Principles of Optics*, London, 1959.

[43] B. Sturman and D. M. Giel, *Description of readout processes during strong beam coupling*, *Phys. Rev.* **E 69**, 2004.

[44] P. Günter, J.-P. Huignard *Photorefractive materials and their applications I and II*, *Springer Series in Optical Sciences*, vol.**59**, Springer-Verlag, Heidelber, 1991.

[45] B. Sturman, S. Odoulov, L. Holtmann, U. van Olfen, *Dynamics of parametric conical scattering of orthogonally polarized waves in BaTiO3*, Appl. Phys. A **52**, 2411-2418, 1995

[46] M. Horowitz, B. Fischer, *Parametric scattering with constructive and destructive light patterns induced by mutually inhogerent beams in photorefractive crystals*, *Opt. Lett.* **17**, 1082-1084, 1992

[47] B. Sturman, M. Goulkov, S. Odoulov, *Polarized-generate parametric light scattering in photorefractive crystals*, *Appl. Phys.* B **56**, 193-199, 1993

[48] B. Sturman, M. Goulkov, S. Odoulov, *Phenomenological analysis of the parametric scattering processes in photorefractive crystals*, *J. Opt. Soc. Am.* B **13**, 2602-2609, 1996

[49] M. Goulkov, S. Odoulov, B. Sturman, A. I. Chernukh, E. Krätzig, G. Jäkel, *Bright light dots caused by interference of parametric scattering processes in LiNbO3 crystals*, *J. Opt. Soc. Am.* B **13**, 2602-2609, 1996

[50] S. Odoulov, K. Belabaev, I. Kiseleva, *Degenerate stimulated parametric scattering in LiTaO3*, *Opt. Lett* **10**, 31-33, 1985

[51] K. Belabeev, I. Kiseleva, V. Obukhovskii, S. Odoulov, R. A. Taratura, *New parametric holographic-type scattering of light in lithium tantalate crystals*, *Sov. Phys. Solid State* **28**, 321-322, 1986

[52] D. A. Temple, C. Warde, *Anisotropic scattering in photorefractive crystals*, *J. Opt. Soc. Am.* B **3**, 337-341, 1986

[53] M. D. Ewbank, P. Yeh, J. Feinberg, *Photorefractive conical diffraction in BaTiO3*, *Opt. Commun.* **59**, 423-428, 1986

[54] R. A. Rupp, F. W. Dress, *Light-induced scattering in photorefractive crystals*, *Appl. Phys.* B **39**, 223-229, 1986

[55] H. C. Ellin, L. Solymar, *Light scattering in bismuth silicate: matching of experimental results*, *Opt. Commun.* **130**, 85-88, 1996

[56] H. Rajbenbach, J. P. Huignard, *Self-induced coherent oscillations with photorefractive Bi12SiO20*, *Opt. Lett.* **10**, 137-139, 1985

[57] H. Rajbenbach, A. Delboulbe, J. P. Huignard, *Noise suppression in photorefractive image amplifiers*, *Opt. Lett.* **14**, 1275-1277, 1989

[58] S. Stepanov, S. M. Shandarov, and N. D. Khat'kov, *Photoelastic contribution to the photorefractive effect in cubic crystals*, *Sov. Phys. Sol. State*, **29**, 1754-1756, 1987.

[59] E. Shamonina, V. P. Kamenov, K. H. Ringhofer, G. Cedilnik, A. Kiessling, and R. Kowarschik, *Optimum orientation of volume phase gratings in sillenite crystals: is it always [111]?*, *J. Opt. Soc. Am.* **B 15**, 2552-2559, 1998.

[60] V. V. Shepelevich, S. M. Shandarov, and A. E. Mandel, *Light diffraction by holographic gratings in optically active photorefractive piezocrystals*, *Ferroelectrics*, **110**, 235-249, 1990.

[61] G. Pauliat, P. Mathey, and G. Roosen, *Influence of piezoelectricity on the photorefractive effect*, *J. Opt. Soc. Am.* **B 8**, 1942-1946, 1991.

[62] M. Zgonik, K. Nakagava, and P. Günter, *Electro-optic and dielectric properties of photorefractive BaTiO3 and KNbO3 crystals*, *J. Opt. Soc. Am.* **B 12**, 1416-1421, 1995.

[63] G. Montemezzani, A. A. Zozulya, L. Czaia, D. Z. Anderson, M. Zgonik, P. Gunter, *Origin of the lobe structure in photorefractive beam fanning*, *Phys.Rev.* **A 52**, 1791, 1995.

[64] L. D. Landau and E. M. Lifshiz, *Quantum Mechanics*, *Pergamon Press*, Oxford, 1969.

[65] E. Merzbacher, *Quantum Mechanics* (Wiley, New York, 1970), p. 271.

[66] E. Shamonina, K. H. Ringhofer, B. I. Sturman, V. P. Kamenov, G. Cedilnik, M. Esselbach, A. Kiessling, R. Kowarschik, A. A. Kamshilin, V. V. Prokofiev, and T. Jaaskelainen, *Giant momentary readout produced by switching electric fields during two-wavemixing in sillenites*, *Opt. Lett.* **23**, 1435-1437, 1998.

[67] M. P. Georges, V. S. Scauflair, and P. C. Lemaire, "Compact and portable holographic camera using photorefractive crystals", Appl. Phys. **B 72**, 761-765 (2001).

[68] M. C. Barbosa, L. Mosquera, and J. Frejlich, *Speed and diffraction efficiency in feedback-controlled running holograms for photorefractive crystal characterization Appl. Phys.* **B 72**, 717-721, 2001.

[69] A. A. Freschi, P. M. Garcia, and J. Frejlich, *Charge-carrier diffusion length in photorefractive crystals computed from the initial phase shift*, *Appl. Phys. Lett.* **71**, 2427-2429, 1997.

[70] B. I. Sturman, A. S. Gorkunova and K. H. Ringhofer, *Feedback controlled periodic states for different kinds of photorefractive boblinear response*, *Eur. Phys. J.* **D**, 23, 291-297 (2003).

[71] A. Freschi, and J. Frejlich, *Stabilized Photorefractive Modulation Recording Beyond 100-Percent Diffraction Efficiency In Linbo(3)-Fe Crystals*, *J. Opt. Soc. Am.* **B 11**, 1837, 1994.

[72] P. M. Garcia, K. Buse, D. Kip, and J. Frejlich, *Self-Stabilized Holographic Recording In Linbo3-Fe Crystals*, *Opt. Commun.* **117**, 35, 1995.

[73] P. M. Garcia, A. A. Freschi, J. Frejlich, and E. Krätzig, *Scattering reduction for highly diffractive holograms in LiNbO3 crystals*, *Appl. Phys.* **B 63**, 207, 1996.

[74] V. P. Kamenov, K. H. Ringhofer, B. I. Sturman, and J. Frejlich, *Feedback-controlled photorefractive two-beam coupling*, *Phys. Rev.* **A 56**, R2541, 1997.

[75] E. V. Podivilov, B. I. Sturman, S. G. Odoulov, S. L. Pavlyuk, K. V. Shcherbin, V. Ya. Gayvoronsky, K. H. Ringhofer, and V. P. Kamenov, *Dynamics of feedback controlled photorefractive beam coupling*, *Phys. Rev.* **A 63**, 053805, 2001.

[76] E. V. Podivilov, B. I. Sturman, S. G. Odoulov, S. L. Pavlyuk, K. V. Shcherbin, V. Ya. Gayvoronsky, K. H. Ringhofer, and V. P. Kamenov, *Attractors and auto-oscillations for feedback controlled photorefractive beam coupling*, *Opt. Commun.* **192**, 399, 2001.

Acknowledgements

I am extremely grateful to Prof. Dr. K. H. Ringhofer for his invitation to work in Germany, friendly reception in his group, scientific working environment, and plenty of discussions, which contributed much to the success of this work. Professor Ringhofer was always willing to help me when problems of any kind arose. I thank him for his competent and patient advice in the fields of physics and daily life.

I am very thankful to Prof. Dr. E. Krätzig for necessary support in hard times, when Prof. Dr. K. H. Ringhofer was unable to work, due to his serious illness. Also I would like to thank Prof. Krätzig for his very interesting lectures and seminars, where I have learned much.

I would like to express my deep gratitude to Prof. Dr. B. I. Sturman from the International Institute for Nonlinear Studies, Novosibirsk, Russia, for steady collaboration, fruitful discussions and scientific stimulation that led to publications in high-quality journals. I thank Prof. B. I. Sturman for his readiness to share his immense knowledge and his ideas with me. Without him, this thesis would have been impossible.

I am very indebted to Dr. M. Gorkounov for his constructive criticism, comments and helpful discussions. I thank him for his support, good advice and help of any kind.

I thank Dr. Shamonina and Prof. Dr. M. Shamonin for fruitful discussions and for their permanent willingness to help me.

My special thanks are to my colleagues M. Lapine and Dr. M. Gorkounov and Dr. A. Gorkounova, Dr. A. Trifonov, E. Svetogorova for the pleasurable and friendly atmosphere at work. Also I thank to J. Selinger for his active help in many situations.

Financial support by Deutsche Forschungsgemeinschaft is gratefully acknowledged.

A very special set of thanks has to be given to my wife Darjya and my son Kuzma who shared frustrations and successes during the last years and for their encouragement and patience knowing that the science sometimes asks for sacrifices. I am also gratitude to my parents for their permanent willingness to help and support me.

Eidesstattliche Erklärung

Hiermit erkläre ich an Eides Statt, die vorliegende Abhandlung selbständig und ohne unerlaubte Hilfe verfaßt, die benutzten Hilfsmittel vollständig angegeben und noch keinen Promotionsversuch unternommen zu haben.

Osnabrück, den 15 Juli 2004

(O. Filippov)

Tag der Einreichung: 15. Juli 2004
Tag der mündlichen Prüfung: 20. September 2004